学位論文

Study of the Venus' upper haze

（金星上部もや層の研究 ）

平成 25 年 12 月博士（理学）申請

東京大学大学院理学系研究科

地球惑星科学専攻

髙木　聖子

Abstract

Venus is completely shrouded by a thick cloud deck floating at 45 – 70 km. The major material of the cloud deck is thought to be H_2SO_4 – H_2O droplets. The upper haze on Venus lies above the cloud layer surrounding the planet, ranging from the top of the cloud (～70 km) up to as high as 90 km. The upper haze particles with an effective radius of ～0.25 μm was suggested from Pioneer Venus Orbiter (PV) measurements. The particles were most likely composed of sulfuric acid in terms of refractive index ～1.45. The haze vertical optical thickness in the polar region at 365 nm was found to be 0.8 above the main cloud of 1 μm particles by PV measurements. By comparison, the optical thickness of the haze above the main cloud at low latitudes was found to be 0.06 [Kawabata et al., 1980]. Knibbe et al. (1998) and Braak et al. (2002) observed a gradual decrease of the haze particle column density during the PV mission. Braak et al. (2002) reported a correlation between the decrease of SO_2 abundance [Esposito et al., 1988; Na et al., 1990] and that of the polar haze optical thickness. However, it is unclear how haze are produced and composition of haze.

The upper layer detected (above the clouds) is characterized by a SO_2 mixing ratio increase with altitude from 85 to 105 km [Belyaev et al., 2012]. It shows a new source of SO_2 at high altitude. One possible source of SO_2 in the upper haze layer could be photo-dissociation of H_2SO_4 vapor resulting from evaporation of acid aerosol droplets. However, recent upper limit of H_2SO_4 from sub-mm ground-based observation makes this theory less likely [Sandor et al., 2012]. The cause of the phenomena given above is still controversial.

The Solar Occultation at InfraRed (SOIR) on board Venus Express (ESA) is designed to measure the atmospheric transmission at high altitudes (70 – 220 km) in the IR (2.2 – 4.3 μm) with high resolution by solar occultation. The SOIR data obtained in 2006-2009 are analyzed to examine the upper haze at altitude above 90 km. Vertical and latitudinal distribution of haze extinction, optical thickness and mixing ratio are calculated in using SOIR data statistically. Extinctions and optical thickness at low latitude are two times thicker than those of high latitude. One of the notable results is that mixing ratios increase at altitude above 90 km at both high and low latitudes. It is speculated that sources of haze are transported upward from under altitude 90 km and haze is produced at high altitude. From comparison with the vertical distributions of SO and SO_2 mixing ratios reported by Belyaev et al. (2012), it is speculated about the correlation between sulfuric compound and haze.

Contents

1. Introduction

1.1. Previous Venus observation

1.1.1. Cloud

The Venus cloud consists of a main cloud deck at 47 – 70 km, with thinner hazes above and below. Instruments on the Venera 9 and 10 landers and the four Pioneer Venus (PV) entry probes provided simultaneous in-situ measurements of the vertical structure and particle size distributions in the clouds [Esposito et al., 1983]. They found that the main cloud consists of three distinct layers. Three layers, known as the upper (~57 to 70 km), middle (~49 to 57 km) and lower (~47 to 49 km) clouds, are bounded above and below by more diffuse haze layers. Sulfuric acid (H_2SO_4) aerosols are the principal constituent of all three layers, but the particle size distributions differ from layer to layer. The PV Orbiter Cloud Photopolarimeter (OCPP) measurements showed that the upper haze layer is composed primarily of very small 'mode 1' particles, which have modal radii between 0.25 and 0.4 μm. The PV Large Probe Cloud Particle Spectrometer (LCPS) showed that the lower haze was also composed primarily of these particles. The upper cloud consists primarily of a second particle type, called 'mode 2' which has a ~1 μm equivalent radius, but also includes significant numbers of mode 1 particles. A third particle type, 'mode 3', is the principle component of the middle and lower clouds. This consists of relatively large particles, in a distribution with a mode radius of 3.85 μm and some particles as large as 35 μm equivalent radius. Mode 3 may have a crystalline component of uncertain composition.

A mean cloud model and derivation from the mean were calculated from the measured data collected by previous entry probes, such as Soviet Veneras series

[Takagi and Iwagami. 2011](Fig.1.1). The optical thicknesses of upper haze, upper, middle and lower are 1.0, 10, 14.5 and 8.5, respectively.

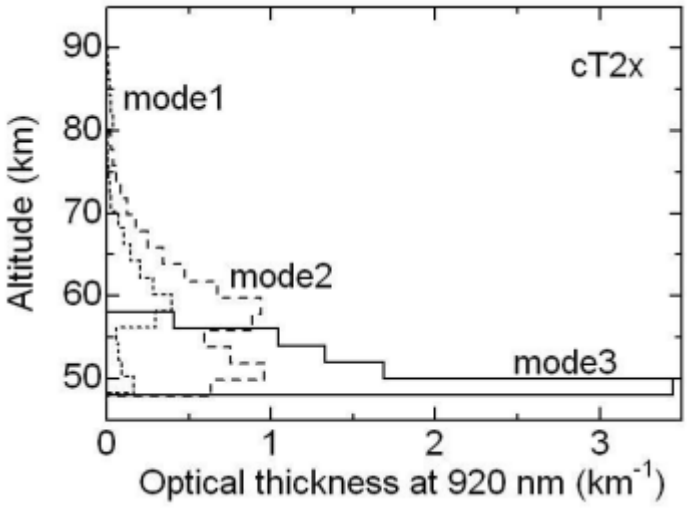

Fig.1.1 The cloud model used for the calculation reported here made from the mean profile shown in Fig. 2(h) by adjusting it to a thickness of 2 km and to a constant mixing ratio of particles in each layer; mode1 (short dashed line), mode2 (long dashed line), mode3 (solid line) [Takagi and Iwagami, 2011].

1.1.2. Early observation of Upper haze (70-90 km)

The upper haze on Venus lies above the cloud layer surrounding the planet, ranging from the top of the cloud (70 km) up to as high as 90 km [Esposito et al., 1983]. The ～1.05 μm particles within the cloud layer were already identified in the early

1970s [Hansen and Hovenier, 1974] and most likely composed of concentrated sulfuric acid (for a review see Esposito, 1983) in terms of refractive index. The existence of the second species of smaller particles within and above the clouds with an effective radius of ~ 0.25 μm was suggested from Pioneer Venus (PV, from 1978 to 1990) measurements [Kawabata et al., 1980]. It was obtained at relatively short wavelengths (< 1.0 μm) by the PV OCPP during the nominal mission in 1979. Haze particles are found to have a refractive index of 1.45 ± 0.04 at 550 nm, an effective radius of 0.23 ± 0.04 μm. The haze vertical optical thickness in the polar region at 365 nm was found to be 0.8 above the main cloud by the PV measurements. By comparison, the optical thickness of the haze above the main cloud at low latitudes was found to be 0.06. Sato et al. (1996) reported that in the north polar region the haze particles have effective radius of 0.25 ± 0.05 μm and the refractive index of 1.435 ± 0.02 at 550 nm. In the south polar region, the haze particles have effective radius of 0.29 ± 0.02 μm and the refractive index 1.45 ± 0.02 at 550 nm.

1.1.3. Recent observation of Upper haze (70-90 km)

Several instruments on ESA's Venus Express (VEX) spacecraft have accumulated new data of the Venus atmosphere over a broad range of wavelengths. It is worth mentioning that both imaging spectrometer Visible and Infrared Thermal Imaging Spectrometer (VIRTIS-M IR) on the nightside [de Kok et al., 2011] and Spectroscopy for Investigation of Characteristics of the Atmosphere of Venus / Solar Occultation at InfraRed (SPICAV/SOIR) at the terminators [Wilquet et al., 2009] are able to target the upper haze above the cloud layers for further investigation. The stellar occultation by SPICAV-UV on the nightside is also useful in this context. SOIR is designed to measure the atmospheric transmission of the solar light in the infrared (IR).

SOIR is an innovative echelle grating spectrometer onboard VEX. All features, capabilities and characteristics of the instrument have been described by Nevejans et al. (2006), Bertaux et al. (2007) and Mahieux et al. (2008). Therefore, only a brief description is given here. SOIR is operated in the solar occultation mode, i.e. the line of sight (LOS) points towards the Sun. As VEX is moving along its orbit, the LOS crosses the atmosphere of Venus at successive tangent altitudes. The instrument is operated in the IR (2.3 – 4.4 μm) and its spectral resolution is about 0.15 cm^{-1}.

The continuum of absorption in the SOIR spectra is primarily shaped by the extinction caused by the aerosol particles in the upper haze. Vertical and latitudinal distributions of extinction are shown by Wilquet et al. (2012) by analyzing the SOIR data. The results focused on the upper haze up to 90 km. As Fig.1.2 shows, extinction profiles are plotted confined to high northern latitude during March-April 2007 and February – March 2008. These profiles are for solar occultation at the morning and the

evening terminator.

Fig.1.3 presents a global picture of all observations considered in Wilquet et al. (2012) regarding the latitudinal dependency of the extinction. For each profile, the value of extinction at 80 km is plotted as a function of the latitude of the observation. For both terminators (morning on the left panel and evening on the right), it is observed that the extinction due to aerosols is significantly smaller in the polar latitudes (by a factor 10 at least) compared to the values around the equator.

Fig.1.4 shows the number densities (N) derived in the UV spectral range for aerosol particles of about 0.1 – 0.3 μm size from the SPICAV-UV channel and in the IR for aerosol particles of about 0.4 – 1.0 μm size from the SPICAV-IR and the SOIR channels depending on the altitude. SPICAV-UV measurements lead to mode 1 particle number density between 10 and 30 cm^{-3} below 90 km with decreasing at higher altitudes. Number density for the larger particles (mode 2) decreases smoothly from 10 to 15 cm^{-3} at 70 km. It decreases down to less than 1 cm^{-3} at 90 km. Wilquet et al. (2009) demonstrated the existence of at least two types of particles. One type with a radius comprised between ～0.1 and 0.3 μm as inferred by the UV channel and the second type, detected in the IR, has a radius varying between ～0.4 and 1 μm depending on the altitude.

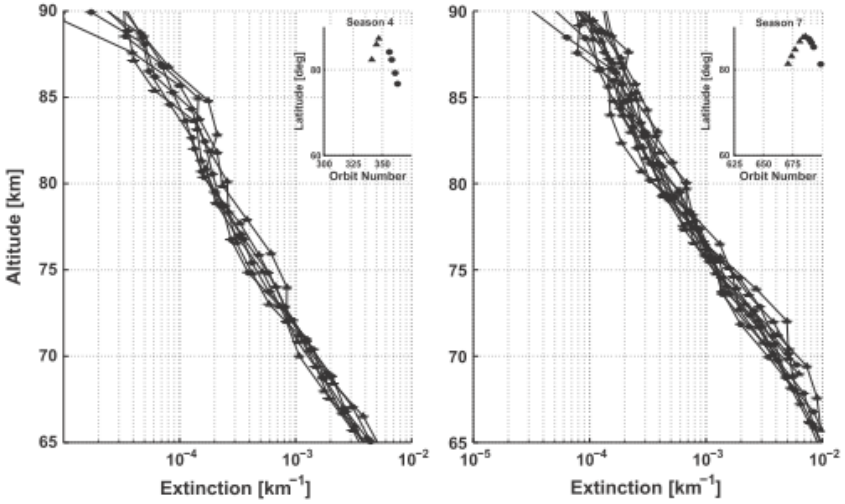

Fig.1.2 Extinction profles at high northern latitudes during March to April 2007 and February to March 2008. Dots (●) are for solar occultation at the morning teminator while Triangles (▲) are for solar occultation at the evening terminator [taken from Wilquet et al. (2012)].

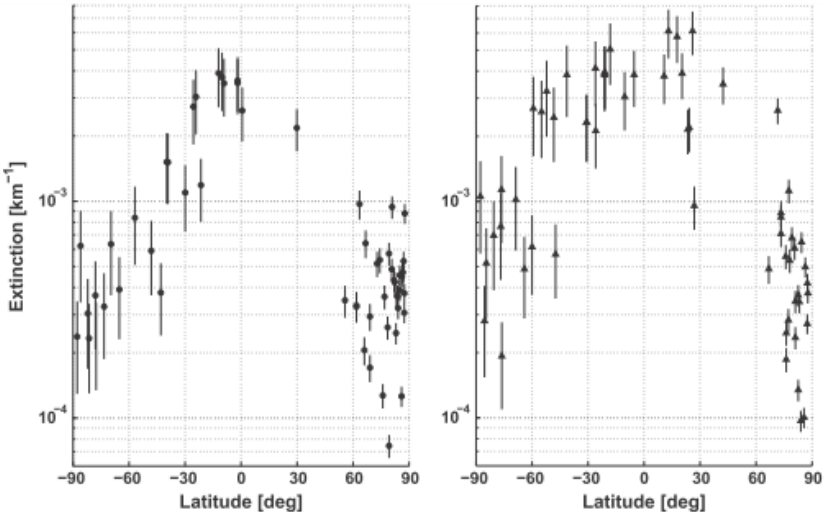

Fig.1.3 Latitudinal distribution of the extinction at 80 km. The left panel is for solar occultation at the morning terminator (●), and the right panel for the evening terminator (▲) [taken from Wilquet et al. (2012)].

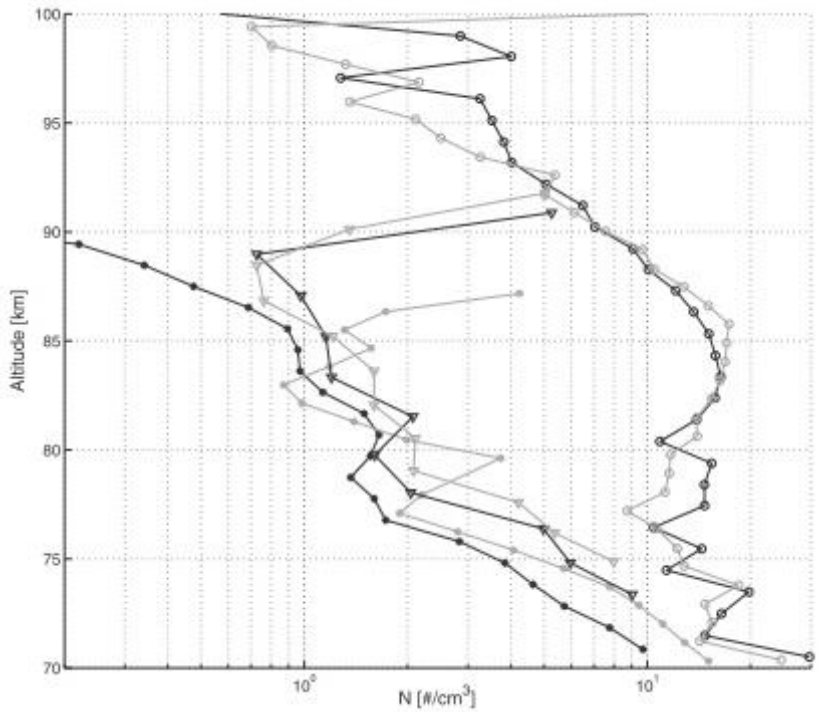

Fig.1.4 Vertical profiles of the particle total number density in the Venus upper haze during two successive orbits of Venus Express. The radius of particles found by fitting normalized extinction to a haze model allowed derive N for mode 1 particles with the SPICAV-UV channel (circles), N for mode 2 particles with the SPICAV-IR channel (inverted triangles), and N for mode 2 particles with the SOIR channel (asterisks) during orbit 485 (black) and orbit 486 (gray) [taken from Wilquet et al. (2009)].

1.2 Relation between Sulfuric compound and Cloud・Haze

1.2.1. Sulfur Chemistry related to Cloud and Haze

Relationship between haze and sulfuric compound is inferred from analogy of correlation between main cloud and sulfuric acid. For example, Belyaev et al. (2012) suggested that haze are related to SO and SO_2 from Venus Express observation. Observations suggesting relation between sulfuric compound and haze will be described in next section. In this section, previously-proposed sulfur chemistry related to cloud and haze will be focused.

Sulfur Oxidation cycle

This cycle involves primarily the oxidation of SO_2 in the upper cloud to form H_2SO_4, condensation and downward transport of the sulfuric acid, and evaporation and decomposition in the lower atmosphere to produce SO_2, CO_2, and H_2O. Chemical reactions and transport processes are summarized in Fig.1.5 (taken from Imamura and Hashimoto. (1998)). The H_2SO_4 – H_2O droplets produced near the cloud top are transported poleward and downward by meridional circulation, sedimentation and eddy diffusion. The droplets evaporate in the hot lower atmosphere to yield H_2SO_4 vapor, a portion of which is transported equatorward below the cloud. The H_2SO_4 vapor is carried aloft by the meridional circulation at low latitudes to condense into cloud particles at 47 – 50 km altitudes. Principal reactions are described in eqs.(1.2.1) and eqs.(1.2.2). Good observational evidence exists for most steps in this cycle [Krasnopolsky and Pollack, 1994]. For example, the Venera 14 photometry at 360 nm showed a decrease in the SO_2 mixing ratio from 50 ppm at 50 km to 10 ppm at 57 km.

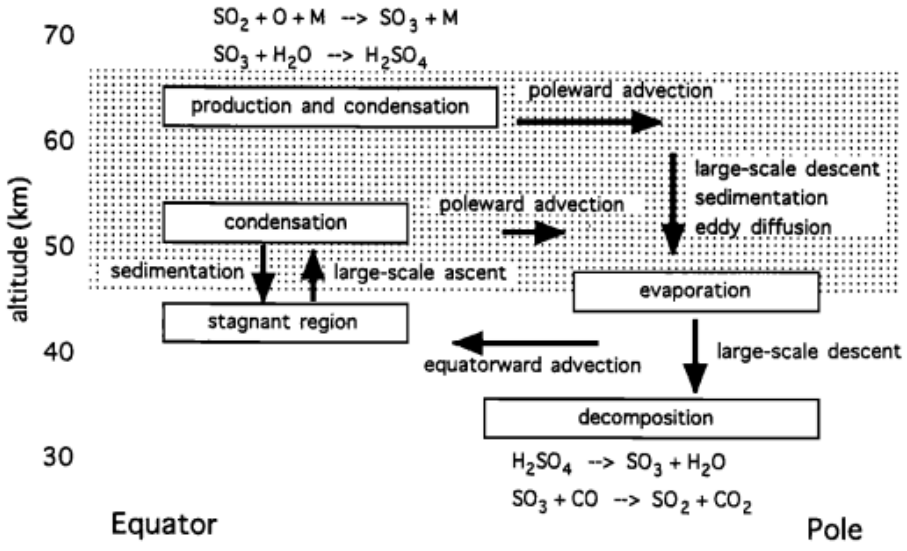

Fig.1.5 Schematic view of the circulation of H_2SO_4 in the Venus atmosphere. Arrows indicate the direction of H_2SO_4 transport. Shaded areas indicate the cloud layer [taken from Imamura and Hashimoto. (1998)].

$$SO_2 + O + M \rightarrow SO_3 + M \qquad (1.2.1\ a)$$

$$SO_3 + H_2O \rightarrow H_2SO_4 \qquad (1.2.1\ b)$$

$$H_2SO_4 \rightarrow SO_3 + H_2O \qquad (1.2.2\ a)$$

$$SO_3 + CO \rightarrow SO_2 + CO_2 \qquad (1.2.2\ b)$$

Polysulfur cycle

Prinn. (1975) suggested a scheme of photochemical formation of sulfuric acid and polysulfur from carbonyl sulfide OCS. The primary sulfur carrier from the deep atmosphere and surface to the middle atmosphere is OCS. Near and above the cloud

tops, OCS readily dissociates, releasing the S atom.

$$OCS + hv \rightarrow CO + S \qquad (1.2.3\ a)$$

$$S + OCS \rightarrow S_2 + CO \qquad (1.2.3\ b)$$

The S atom gets oxidized to SO by reaching with O and O_2

$$S + O + M \rightarrow SO + M \qquad (1.2.4\ a)$$

$$S + O_2 \rightarrow SO + O \qquad (1.2.4\ b)$$

Further oxidation to SO_2 can proceed via the three-body reaction

$$SO + O + M \rightarrow SO_2 + M \qquad (1.2.5)$$

Catalytic oxidation by ClO is also possible

$$SO + ClO \rightarrow SO_2 + Cl \qquad (1.2.6)$$

Below the cloud tops, oxygen is scarce. In the absence of an oxygen source, S reacts with other S bearing species to from polysulfur, S_x. The reactions are summarized in Fig.1.5 (taken from Yung et al. (2009)).

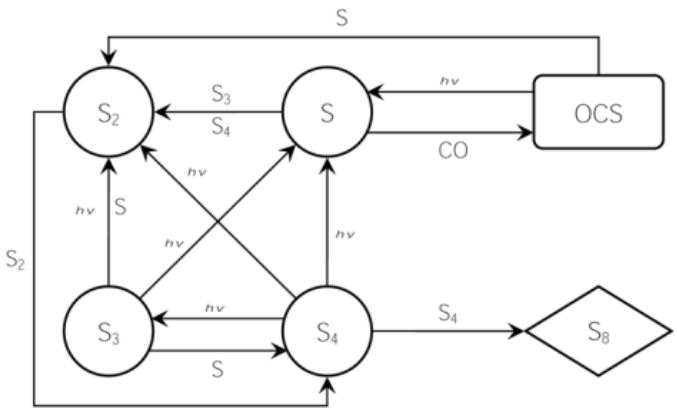

Fig.1.6 Schematic diagram illustrating the S_x chemistry [taken from Yung et al. (2009)].

Aerosol and Sulfur compound

It is speculated that aerosol and sulfuric compound are connected by condensation and evaporation as shown in Fig.1.6. Fig.1.7 illustrates the important pathways of the sulfur cycle related to aerosols [Zhang et al., 2012]. However, the relationship between aerosol and sulfuric compound and composition of haze are still unknown.

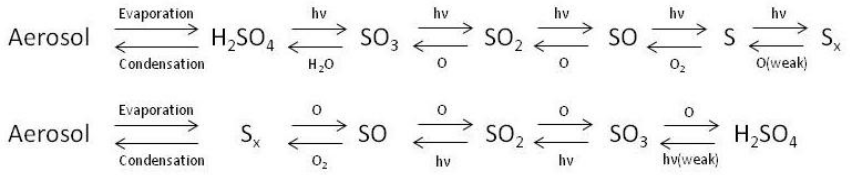

Fig.1.7 Relationship sulfur compound and haze [modified Zhang et al. (2012)].

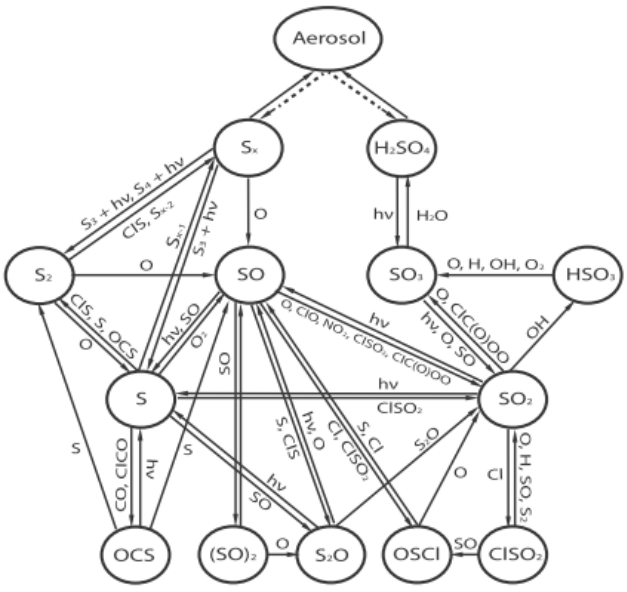

Fig.1.8 Important chemical pathway for sulfur species [taken from Zhang et al. (2012)].

1.2.2. Observations suggesting relation between Sulfuric compound and Haze

Fig.1.9 (taken from Belyaev et al. (2012)) exhibit two layers of SO_2 abundance: the lower layer (65 – 80 km) observed by SOIR measurements, and the upper one (85 – 105 km) observed by SPICAV-UV. Mixing ratio of SO_2 decreases from 0.2 to 0.02 ppmv at 65 – 80 km and increases from 0.05 to 2 ppmv at 85 – 105 km. The upper layer detected (above the clouds, but within the upper haze) is characterized by a SO_2 mixing ratio increase with altitude from 85 to 105 km. It shows a new source of SO_2 at high altitude. One possible source of SO_2 in the upper haze layer could be photo-dissociation of H_2SO_4 vapor resulting from evaporation of acid aerosol droplets. However, recent upper limit of H_2SO_4 from sub-mm ground-based observation makes this theory less likely [Sandor et al., 2012]. The cause of the phenomena given above is still controversial. That is, the relationship sulfuric compound and haze and transport process are still unknown.

Using OCPP polarization data, Knibbe et al. (1998) revisited later by Braak et al. (2002), pointed out long-term temporal variations of the haze layer. They observed a gradual decrease of the haze particle column density during the PV mission. Optical thickness of the haze is found to be 0.25 in 1978 and 0.1 or less in 1990. From OCPP data of the beginning of the PV mission, Sato et al. (1996) also observed short-term variations of optical thickness of the haze particles in the polar regions. As shown in Fig.1.10 (taken from Belyaev et al. (2008)), after a sharp increase of SO_2 abundance between 1967 and 1979, a gradual decline down to 20 ppb at 1995 was observed. Three possible explanations of such behavior were recently recalled by Mills and Allen

(2007): active volcanism [Esposito, 1984], changes in the effective eddy diffusion within the cloud layers [Krasnopolsky, 1986], and changes in atmospheric dynamics [Clancy and Muhleman, 1991]. At present, another global increase of SO_2 between 2004 and 2007 is observed. Studies of SO_2 at the Venus cloud top at the same period show a gradual decrease of SO_2 abundance with time [Esposito et al., 1988; Na et al., 1990]. Braak et al. (2002) reported a correlation between the decrease in SO_2 abundance and that of the polar haze optical thickness. However, it is still unclear how haze are produced and what the composition of haze is. The speculation is described in the previous section.

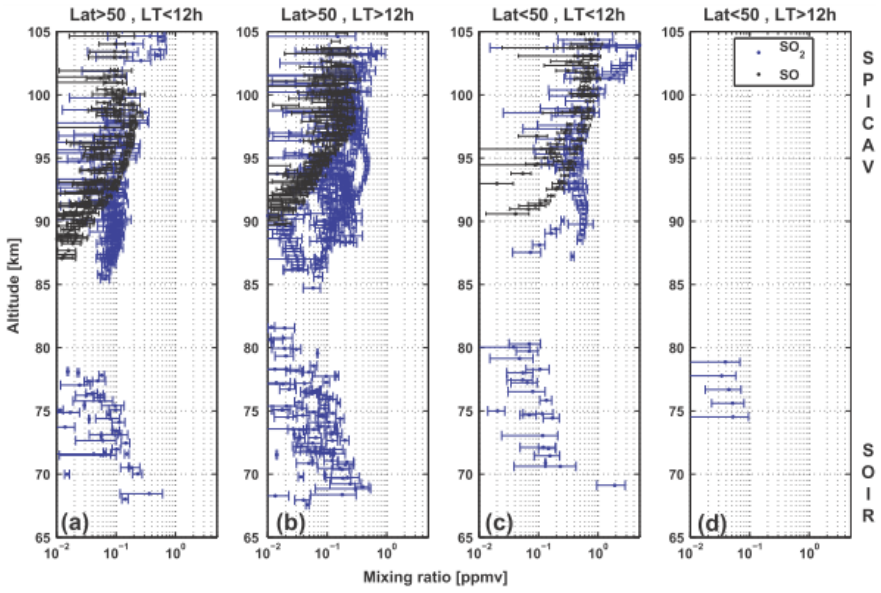

Fig.1.9 SO (black) and SO_2 (blue) mixing ratios: (a) Northern high latitude in morning (> 50 °, < 12 h); (b) Northern high latitude in evening (> 50 °, > 12 h); (c) Low latitude in morning (> 50 °, < 12 h); (d) Low latitude in evening (> 50 °, < 12 h). Values below 80 km are from SOIR measurement, while values above 85 km are from SPICAV UV [taken from Belyaev et al. (2012)].

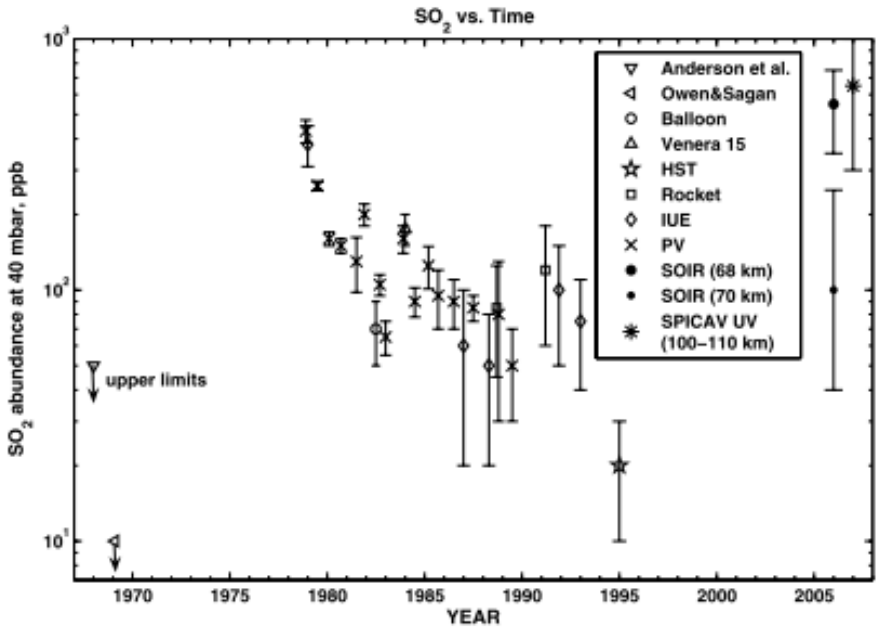

Fig.1.10 Measurements of SO_2 mixing ratio on Venus above the clouds 40 mbar (～69 km of altitude), available from 1969 up to 2008. SOIR results at 68 and 70 km (only at high latitudes) and SPICAV UV results at 100 to 110 km [taken from Belyaev et al. (2008)].

1.3. Purpose of this study

The aim of this work is to examine the upper haze properties at altitude above 90 km, especially extinction, optical thickness and mixing ratio. This work also has aim to discuss the relationship between sulfuric compound and haze at high altitude.

Although several studies have been made on haze layer, there is a poor understanding about it. For example, haze creation process, composition, global distribution, transport process, relationship with sulfuric compound and H_2SO_4 cloud, and so on. If the upper haze properties and relationship with sulfuric compound are cleared in this work, dynamic and chemical process could be cleared globally. This work could be the breakthrough to understand the dynamic and chemical process of overall Venus cloud including main cloud deck, not only confined to the haze layer.

2. Observation

2.1. Venus Express mission

Venus Express (VEX) is the sister mission of the Mars Express mission (MEX). It was proposed in 2001. It reused the design of the MEX mission, and was developed in a very short time. The VEX was launched from the Baikonour cosmodrome in Kazakhstan, on November 9, 2005 by a Soyuz-FG/Fregat rocket. After maneuvers in space to correct the trajectory, the spacecraft arrived at Venus on April 11, 2006 after a 150 days journey. The satellite was placed in a 24 hours polar orbit.

The nominal mission started on June 4, 2006 for two Venus sidereal years (486 Earth days), so until October 2007. It was extended two times for four other sidereal years in total, making that the mission would end in December 2012.

As shown in Fig.2.1, the periapsis of the orbit is located above the north pole, at an altitude varying between 180 and 250 km. The apoapsis is located above the south pole, at an altitude of 65,000 km.

The satellite is a cube of 1.65 m by 1.7 m by 1.4 m, weighting 1,270 kg. On two sides of the spacecraft solar panels are placed to supply electricity to its equipment. The inside temperature is maintained at 25 ◦ C. Venus Express is a three-axis stabilized spacecraft. The sensor components of the Attitude and Orbit Control System (AOCS) comprise two Star Trackers (STR), two Inertial Measurement Units (IMU) and two Sun Acquisition Sensors (SAS). Each Star Tracker has a circular field of view of 16.4 degrees and is capable of making measurements using stars of magnitude 5.5 or greater. Three axis attitude data is derived, with at least three stars always present in the field of view. Each Inertial Measurement Unit employs three ring laser gyros

and three accelerometers, aligned on three orthogonal axes. The gyros are used during attitude acquisition, for roll rate control, during the observation phase, to ensure that the required pointing performance is achieved, and during trajectory corrections, where they serve as backups for the other sensing systems. The accelerometers are used during trajectory corrections to make accurate measurements of change of velocity. Each Sun Acquisition Sensor comprises solar cells mounted on a pyramid, which is then mounted on the exterior of the spacecraft main body. The SASs are used for pointing the spacecraft in Sun Acquisition Mode, during attitude acquisition or re-acquisition. The AOCS uses a Reaction Wheel Assembly, comprising four reaction wheels in a skewed configuration, which enables most nominal mission operations to be performed with any three of the four wheels. By speeding up or slowing down a reaction wheel, the AOCS is able to produce a torque about the axis of rotation of that wheel and so cause the spacecraft to rotate about that axis. A change to the speed of three of the wheels allows a torque to be generated about any chosen axis. It is assumed that satellite attitude behavior causes observed intensity variation (±0.2 %) as shown in Fig.3.1. Standard deviation of observed transmittance is estimated 0.5 %. This contains ±0.2 % observed intensity variation.

The aim of the mission is to study the seven following topics [Svedhem et al., 2007]:

- atmospheric structure;
- atmospheric dynamics;
- atmospheric composition and chemistry;
- cloud layers and haze;
- energy balance and greenhouse effect;

- plasma environment and escape processes;
- surface properties and geology.

A summary concerning the mission can be found on the ESA website: http://sci.esa.int/science-e/www/object/index.cfm?fobjectid=33010.

The payload of the spacecraft consists of seven instruments [Svedhem et al., 2007]. The roles of some of them relating to the present study are described in Appendix A. The position of all the instruments on the spacecraft is shown in Fig.2.2. The SOIR instrument, the focus of this study, is further described in the next Chapter.

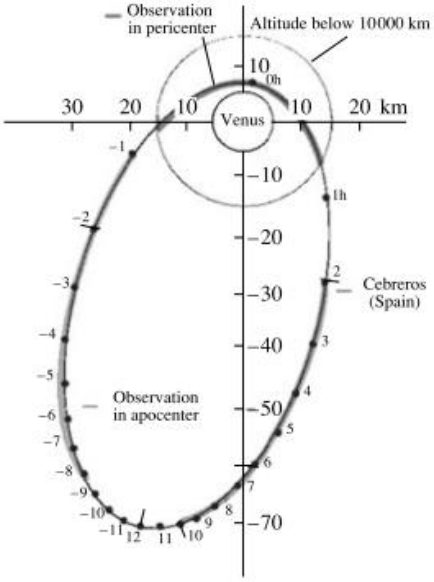

Fig.2.1 The outline of Venus Express orbit. Numeral along the orbit show the time reckoned from the pericenter (orbital time). Arrows mark various segments of the orbit: zone of telecommunication with the Earth, observations in the pericenter, and beyond pericenter [taken from Titov et al. (2006)].

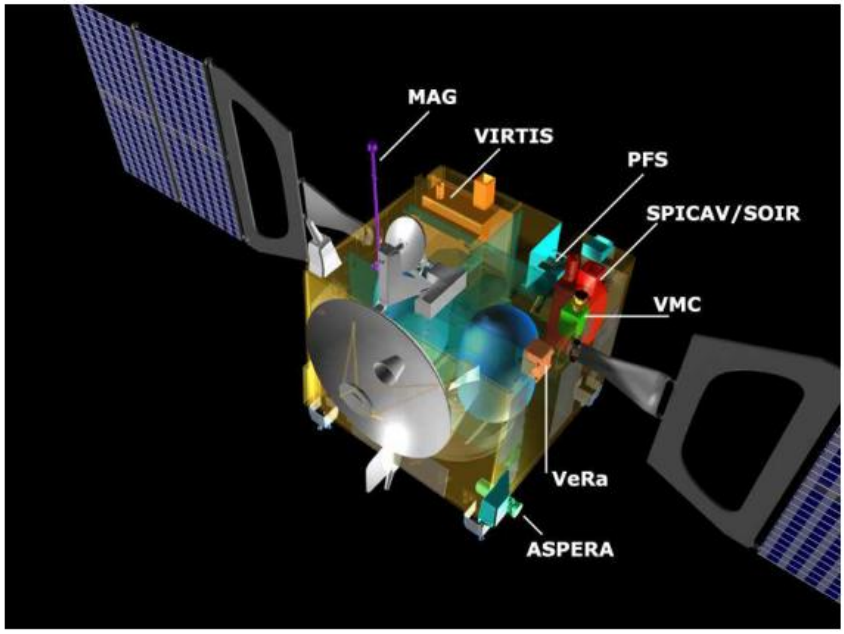

Fig.2.2 Venus Express spacecraft with instruments positions (Credit ESA).

2.2. The SOIR instrument

SOIR is an innovative, compact and high resolution infrared echelle grating spectrometer. It is a low mass instrument, weighting 6.5 kg, confined in a small volume: 414 mm by 254 mm by 210 mm. SOIR is built to probe the atmosphere of Venus using the solar occultation method, therefore to record solar spectra. It measures from 2.2 μm to 4.3 μm, or 4400 cm^{-1} to 2200 cm^{-1}. It was designed at the Belgian Institute for Space Aeronomy in Brussels, Belgium, in collaboration with LATMOS, CNRS, France, and the Russian Academy of Science, IKI, Russia. It is one of the three channels of the French instrument SPICAV/SOIR flying on the mission VEX. The SPICAV instrument is composed of two channels, SPICAV-IR (0.7 – 1.7 μm), measuring in the infrared, and SPICAV-UV (0.11 – 0.31 μm), in the ultraviolet. SPICAV is a sister version of the SPICAM instrument [Bertaux et al., 2000, 2006] flying on the Mars Express spacecraft of the European Space Agency. A complete description of SPICAV can be found in Bertaux et al. (2007).

A solid and mechanical view of the SOIR instrument is given in Fig.2.3 (taken from ESA). Fig.2.3 shows a three dimensional view, with a ray tracing projection inside the instrument. The entrance optics of SOIR, ① on Fig.2.3, are equipped with a fixed periscope-like device to allow the instrument to look at the Sun, when the spacecraft is oriented adequately. The entrance slit has a diameter of 20 mm. After the entrance optics, the light is sent to the Acousto Optical Tunable Filter, or AOTF ③. At the exit of the AOTF, the light enters the spectrometer entrance optics ⑤: the light is focused using a lens in the spectrometer slit. A second lens is used to project the light through an off-axis parabolic mirror ⑥ on the echelle grating ⑦. The refracted light

is then reflected on the same parabolic mirror ⑥. It is finally recorded by the detector ⑨. The parabolic mirror is used twice in the optical path in order to reduce the weight of the instrument. It also reduces the overall size of SOIR.

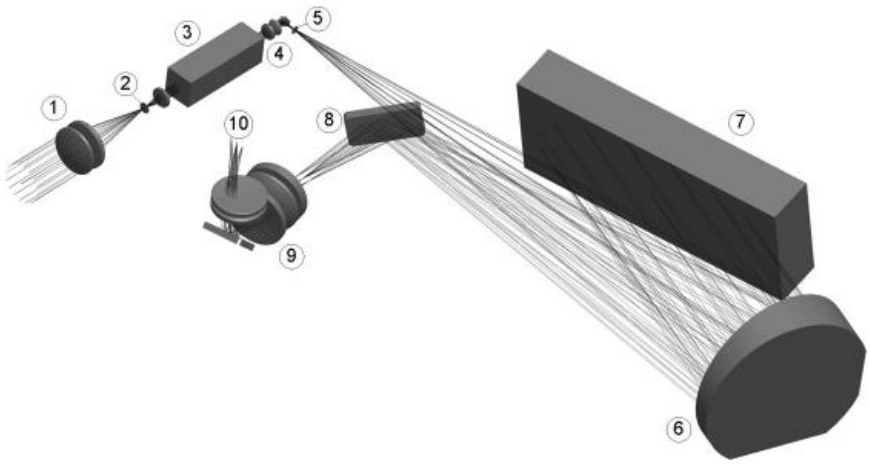

Fig.2.3 Three-dimensional representation of the main SOIR optics elements and ray tracing: ① the entrance optics, ② the diaphragm, ③ the Acousto-optical tunable filter (AOTF), ④ the AOTF exit optics, ⑤ the spectrometer slit, ⑥ the off-axis parabolic mirror, ⑦ the echelle grating, ⑧ the folding mirror, ⑨ the detector optics, and ⑩ the detector [taken from Nevejans et al. (2006)].

2.3. Solar Occultation

The solar occultation technique used by SOIR allows the derivation of unique information about the vertical structure and composition of the Venus atmosphere and cloud. SOIR is looking toward the Sun and records spectra on a one second cycle basis. Solar occultations occur when the line of sight of the instrument crosses the atmosphere of Venus. The projection of the center of the slit on the limbs during each single measurement defines the tangent altitude. Because the spacecraft is moving along its orbit, the instrument sounds the atmosphere of the planet at different tangent altitudes (Fig.3.7). Two different configurations can be observed: the ingress case, when the tangent altitude decreases with time, and the egress case, when the tangent altitude increases with time. For the sake of simplicity, only the ingress case will be described here. The egress case may be considered as ingress with the timescale reversed.

The instrument is turned on and, after a precooling phase to ensure that the detector temperature has reached its operating value of about 70 K, it starts recording solar spectra before the line of sight crosses the atmosphere. It is assumed that the atmosphere of Venus extends up to 220 km in altitude [Hedin et al., 1983]. This procedure starts early enough, corresponding to tangent altitudes well above 220 km, to obtain an amount of at least 40 spectra taken outside the atmosphere. They define the reference Sun spectrum. For tangent altitudes lower than 220 km, the atmospheric transmittances are calculated by dividing the spectrum recorded at the current time by the reference Sun spectrum.

When SOIR points toward the Sun, the position of the slit with respect to Venus is set in order to have its spatial direction parallel to the limb of Venus, when the tangent altitude reaches 60 km (Fig.2.4). The slit should remain as parallel as possible to the limb in order to have the smallest vertical resolution for each separate measurement. Since the VEX is set into an inertial mode while performing a solar occultation, the slit rotates slightly, and does not remain parallel to the limb during the whole occultation. This tilting angle (γ_{slit} on Fig.2.5) remains small, reaching maximum values in some occultations of about 10° which slightly decreases the vertical resolution. The variations of tangent altitude and latitude during one occultation are summarized in Mahieux et al. (2010). During one occultation, tangent points move through a distance of several dozen kilometers at most in a horizontal direction. Such horizontal move has little impact on observed transmittance.

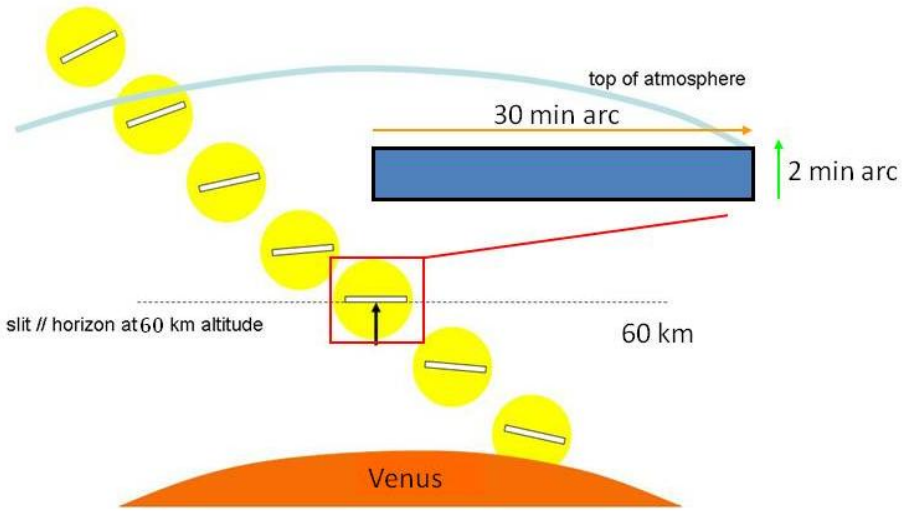

Fig.2.4 Slit position during an occultation. The slit become parallel to the limb of Venus when the tangent altitude reaches 60 km [taken from A. Mahieux, personal communication].

The slit of SOIR is 2′ in the spectral direction, and 30′ in the spatial direction. The apparent size of the Sun at Venus is 44′, which ensures that the slit will remain within the solar disk. The vertical distribution is comprised between 200 m and 700 m at high northern latitudes and from 2.0 up to 5.0 km in the southern hemisphere [Mahieux et al., 2010].

The VEX does not point to the center of the Sun. It points to a point located 10′ above the center of the Sun. This configuration is depicted in Fig.2.6. The reason for the depointing comes from the consideration that the refraction of the light beams in the Venus atmosphere has to be considered. This is due to the atmospheric density at the lowest altitudes reached by SOIR. If the instrument points to the center of the Sun, the refracted Sun would exit the pointing direction too early in the occultation [Mahieux et al., 2008]. The refraction displaces the image of the Sun away from the limb.

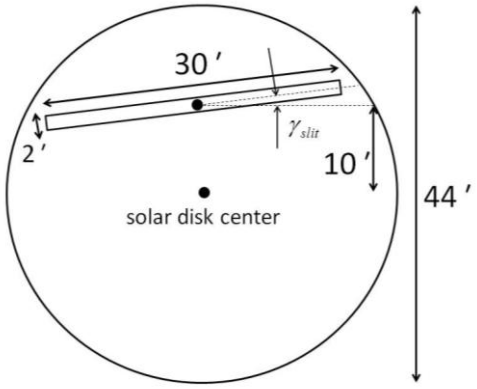

Fig.2.5 Position of the slit in the solar disk. The slit has a size of 30′ by 2′, respectively in the spatial and spectral direction. The slit does not point to the solar disk center, but 10′ above it. It is tilted by an angle of γ_{slit} [modified A. Mahieux Doctoral thesis].

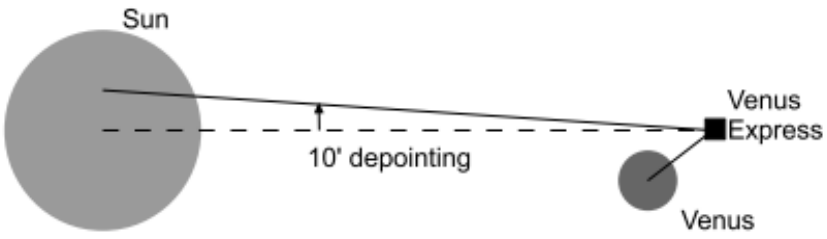

Fig.2.6 Description of the pointing direction of the instrument SOIR, by pointing 10′ above the center of the Sun [taken from A. Mahieux Doctoral thesis].

2.4. Transmittance observed by SOIR

Fig.2.7 gives an example of the observed transmittance (T_{obs}) through one occultation (03 Dec. 2007, order147, orbit591, latitude 9 °S, longitude 209 °). Vertical scale on Fig.2.7 is enlarged; the bottom of the vertical scale on Fig.2.7 is 0.95.

At the beginning of the one occultation, the light path is assumed not to cross the Venus atmosphere down to 220 km in tangent height h_{tg}. No absorption signature is assumed to be present and transmittances are equal to almost unity. As the Sun sets, the light path goes deeper and deeper into the atmosphere, and two absorption processes take place: continuum absorption due to aerosols and line absorption such as CO_2. The influence of scattering on transmittance is currently under investigation. It is speculated that the contribution of scattering light is proportional to optical thickness in the optical path. If absolute values of observed transmittance are changed

due to scattering, the figures of spectra stay unchanged. At the end of an occultation, no light is captured anymore because the Sun disappears behind the cloud deck.

As seen in Fig.2.7, solar spectrum has already been removed from observed spectra. It is found that the standard deviation on the observed transmittance is small enough to isolate an individual observed transmittance regardless of high-altitude observation. It is recognized that no absorption signature is present at altitude above 90 km. For example, the difference between the spectra at 118.54 km and 115.77 km appears to be 0.3 % while the random error appears to be 0.1 %.

Fig.2.8 gives examples of observed transmittance. All examples are enlarged and separated completely regardless of high-altitude observation. The total number of occultations used in this study are 130.

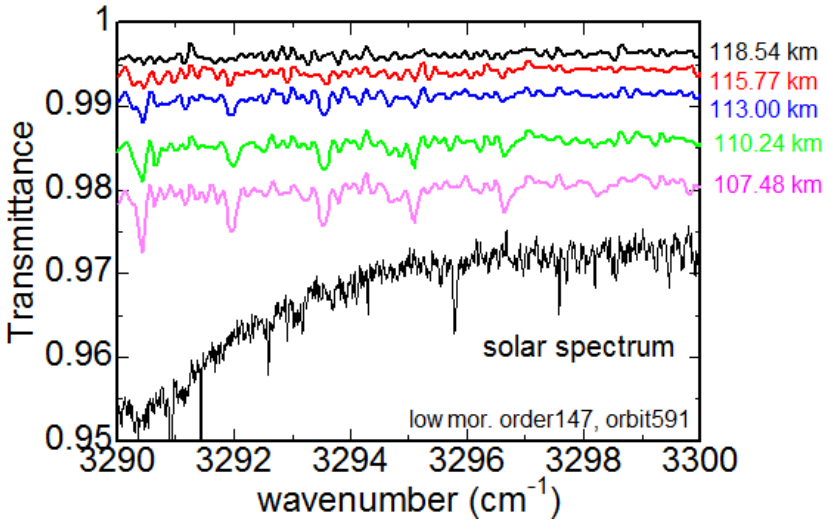

Fig.2.7 Example of observed transmittance (03 Dec. 2007, order147, orbit591, latitude 9 ° S, longitude 209 °). A solar spectrum (black) is also plotted. The standard deviation on the observed transmittance is small enough to isolate an individual observed transmittance regardless of high-altitude observation.

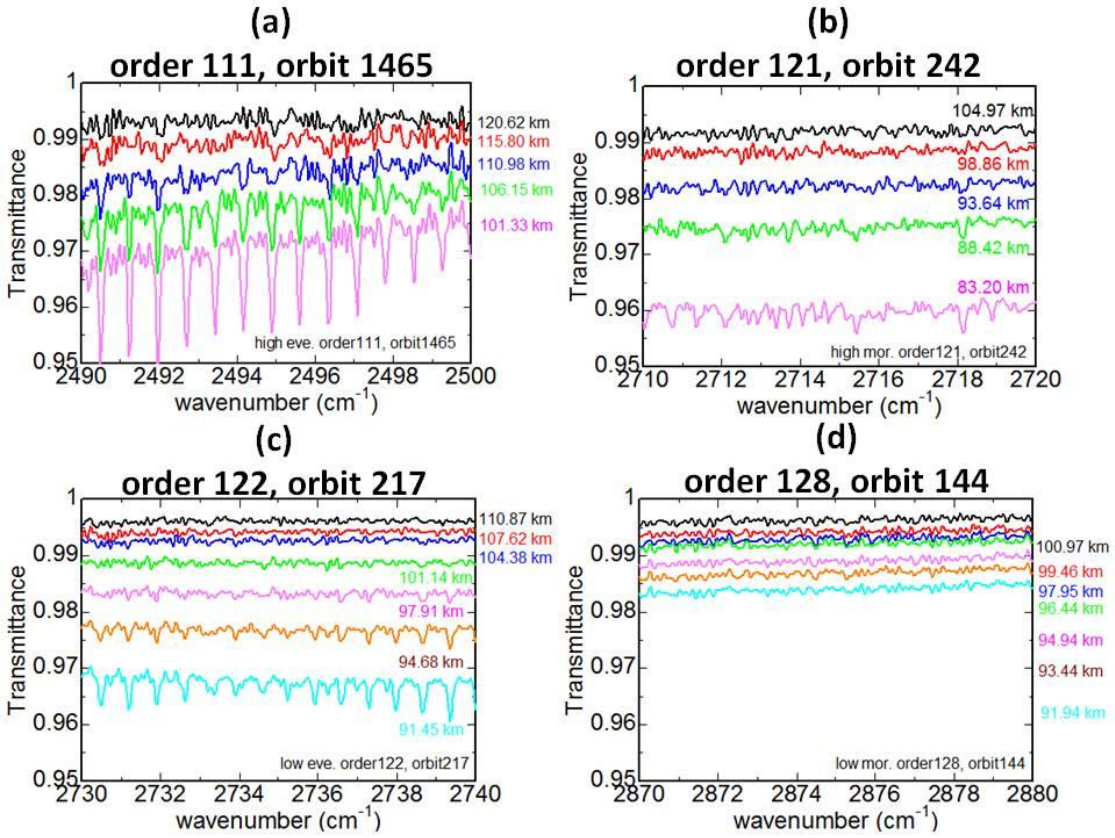

Fig.2.8 Example of spectra obtained during one occultation. Each transmittance is obtained by making the ratio of the solar spectrum seen through the Venus atmosphere to the unattenuated solar spectrum measured above the atmosphere. The selected orders are (a) order111, (b) order121, (c) order122 and (d) order128.

2.5. Spatial and temporal distribution of the measurements

Fig.2.9 shows all observed data used in this study (see Appendix C. for details). Dots (●) are for solar occultation at the morning terminator while triangles (△) are for solar occultation at the evening terminator. There is one orbit per day. The total number observed occultation on Fig.2.9 is 130. Most of these data are obtained from 2006 to 2009 at high latitude.

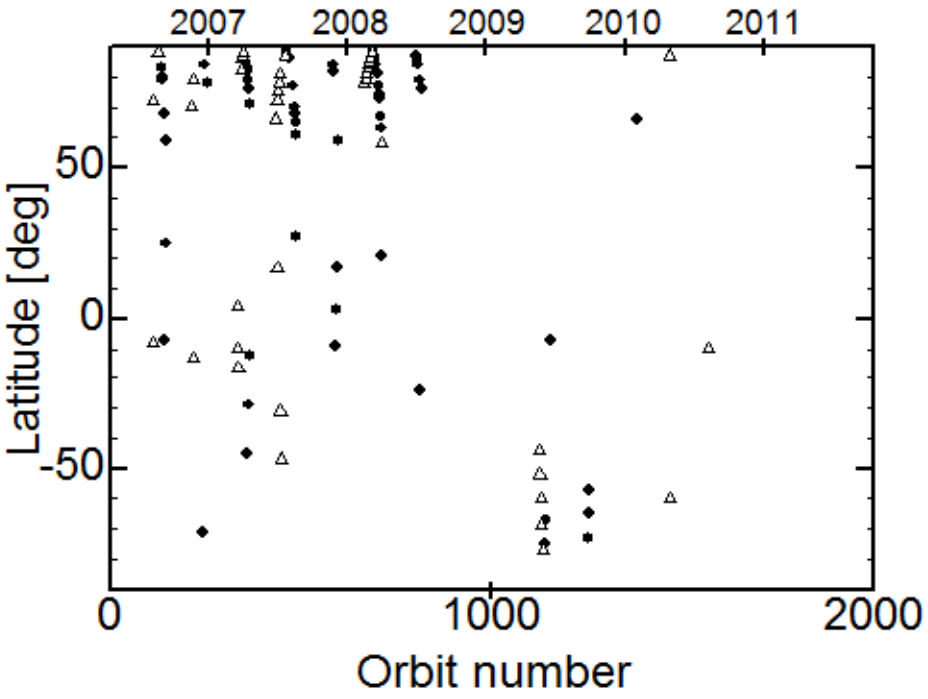

Fig.2.9 Latitudes of SOIR occultations are plotted as a function of the VEX orbit number. Dots (●) are for the morning terminator while triangles (△) are for the evening terminator. There is one orbit per day. The reason why less than 2000 number of data were selected in standard way described in Section 3.5.

3. Analysis

3.1. Redefined Transmittance

The value of observed transmittance at top altitude is not equal to unity (see Fig.2.7). This may be due to combination of pointing error and limb darkening of the solar disk. Fig.3.1 shows reference solar spectrum (blue line) with almost 0.4 % fluctuation observed at exo-atmosphere. It would appear that the fluctuation is caused for the above reason. The contribution of limb darkening to observed transmittance will be examined in next chapter. In this study, the observed transmittance at top altitude is redefined as unity as shown in the right-hand on Fig.3.2. Redefined transmittances are calculated by dividing each transmittance by transmittance at top altitude. The contribution of the configuration to the result of this study is estimated almost 10 % as shown in Fig.3.3. The top observed altitude differ from one occultation to another. The difference affects only two scale heights of the result in this study.

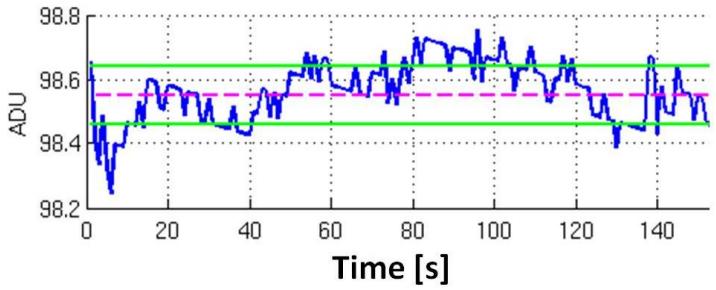

Fig.3.1 Reference solar spectrum (blue) with almost 0.4 % fluctuation observed at exo-atmosphere [taken from A. Mahieux, personal communication]. Vertical axis represents analog to digital unit. Pink dashed line and two green lines represent mean spectra and noise, respectively.

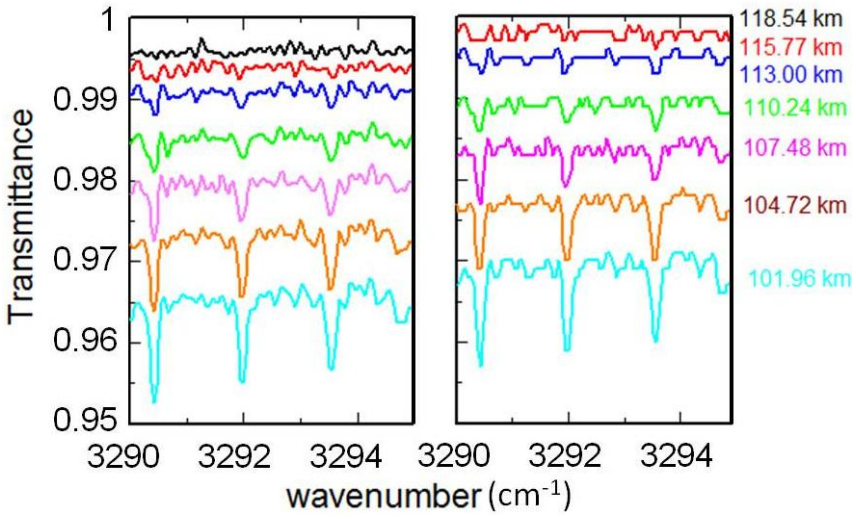

Fig.3.2 Example of (left) observed transmittance and (right) redefined transmittance. For example, the black line on the left panel is redefined to unity on the right panel.

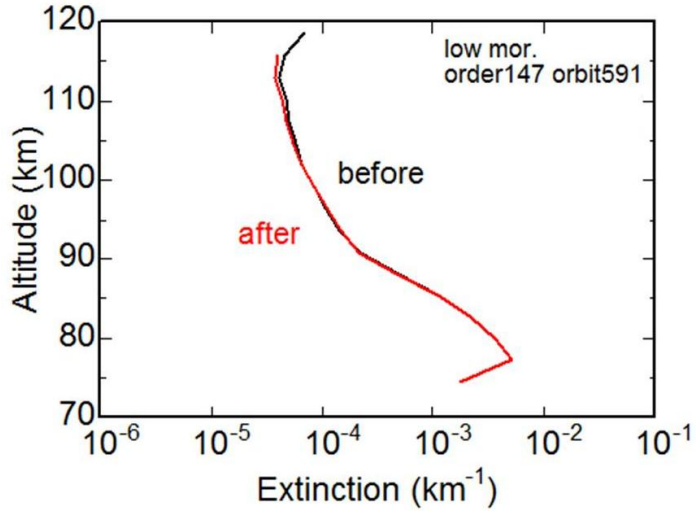

Fig.3.3 The contribution of configulation to the result of this study. The extinction illustrated in black line is calculated from transmittance plotted on the left panel of Fig.3.2. Similarly, the red line represents extinction calculated from transmittance plotted on the right panel of Fig.3.2.

3.2. Limb darkening

The contribution of limb darkening to observed transmittance is calculated as the following process.

The normalized intensity of the Sun $I(\mu)$ is calculated as

$$I(\mu) = 1 - u(1-\mu) \qquad (3.2.1)$$

$$\mu = \cos\theta = \sqrt{1-r^2} \qquad (3.2.2)$$

where radius of the solar disk is set to be unity, r is radial distance from the disk center (Fig.3.4) and u is the limb darkening coefficient. u depends on wavelength and is estimated from 0.1 to 0.4 in the 2 ～ 4 μm [Hestroffer and Magnan, 1998].

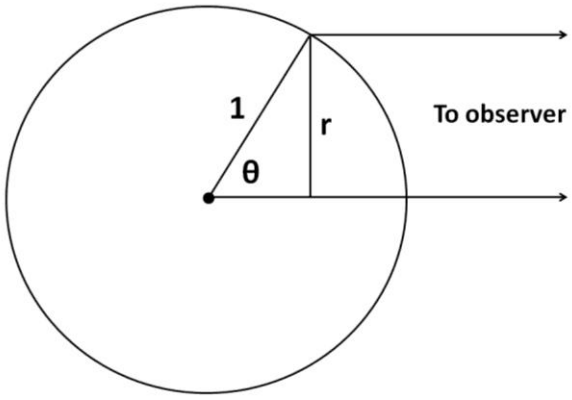

Fig.3.4 Limb darkening geometry. Radius of the solar disk is unity. r is radial distance from the disk center.

Fig.3.5 shows normalized intensity of solar disk calculated by eq.(3.2.1) and eq.(3.2.2). The brightness of disk center is defined to unity. If the slit is stirred 2 arcmin in vertical, the contribution to the observed transmittance is estimated almost 0.1 %. In case of Fig.2.7, the slit is needed to stir more than 2 arcmin in vertical to explain the gap from observed transmittance at top altitude to unity.

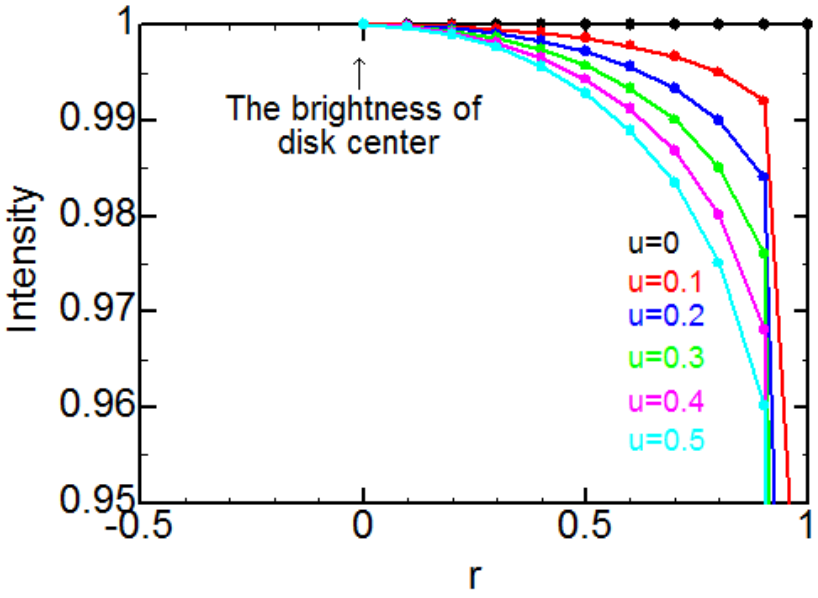

Fig.3.5 Calculated normalized intensity of solar disk. *u* depends on wavelength. *u* is estimated from 0.1 to 0.4 at 2～4 μm.

3.3. Removal of molecular absorption

As described in Section 2.4, T_{obs} is obtained by removing solar spectra from observed spectra. As the aerosol signature is continuum absorption with an wavelength scale of μm which is much larger than the each SOIR spectral range of 20 $cm^{-1} \approx 0.01$ μm, the impact of aerosols on the observed spectra is therefore a decrease of the mean transmittance levels with decreasing altitude (ex. Fig.2.7), which is called in the thesis the baseline of the spectra.

To define the baseline, molecular absorption signatures due to Venus' atmospheric molecules such as CO_2 are removed from observed transmittance. Molecular absorption T_{molec} is calculated in using following equations,

$$T_{molec} = e^{-\tau_{total}} \qquad (3.3.1\ a)$$

$$\tau_{total} = \sum \tau_i \qquad (3.3.1\ b)$$

$$\tau_i = \sigma_i \int_{light\ path} n_i ds \quad (i = CO_2, H_2O, SO_2, HCl...) \qquad (3.3.2)$$

where τ_i, σ_i and n_i is optical thickness, absorption cross-section and number density of i-th gas respectively. σ_i s and n_i s are obtained from Venus atmosphere model, HITEMP 2000, VIRA 1985 model [Keating et al., 1985] and HITRAN 2008. σ_i is calculated in using voigt function. Line absorption is obtained from HITRAN and temperature and number density are obtained from VIRA 1985 model.

As shown in Fig.3.6.1, overall T_{molec} level is equal to unity because of no aerosol absorption is supposed.

The baseline (T_{base}) is defined by dividing T_{obs} by T_{molec} (see eq.(3.3.3) and

Fig.3.6.2).

$$T_{base} = \frac{T_{obs}}{T_{molec}} \qquad (3.3.3)$$

In case of the analysis by the SOIR team, the continuum is obtained by fitting the baseline of spectra, i.e. the observed transmittance from which absorption lines have been removed, by a second degree polynomial as a function of the wavenumber.

Scattering effect is not considered in molecular absorption calculation in this study. Infrared wavelength light is scattered poorly compared to visible wavelength. At 100 km, CO_2 number density is 1.0×10^{14} [cm^{-3}], scattering cross-section at 3 μm is 5.0×10^{-30} [cm^2] and the optical path length in atmosphere is assumed 3.0×10^{7} [cm]. Therefore, optical thickness at 100 km due to Rayleigh scattering is estimated 1.5×10^{-8}. This is considerably smaller than optical thickness due to Mie scattering.

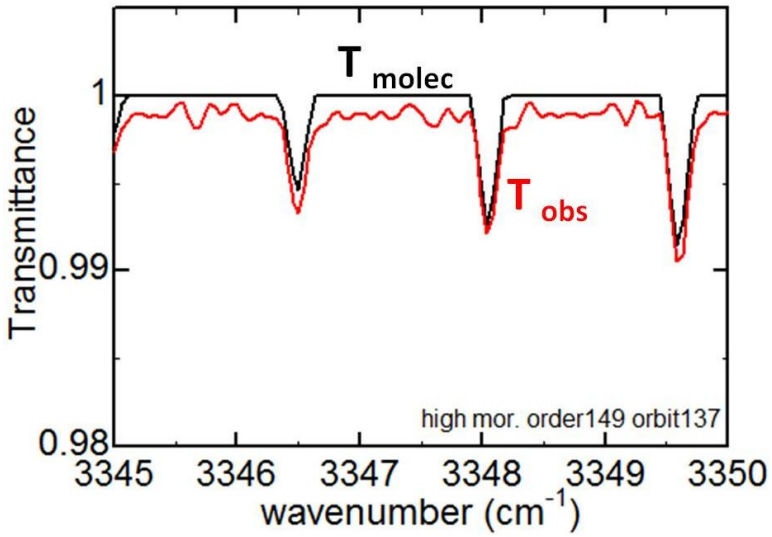

Fig.3.6.1 Example of calculated transmittance (T_{molec}, black line) and observed transmittance (T_{obs}, red line). T_{molec} level is equal to unity because of no aerosol absorption is supposed.

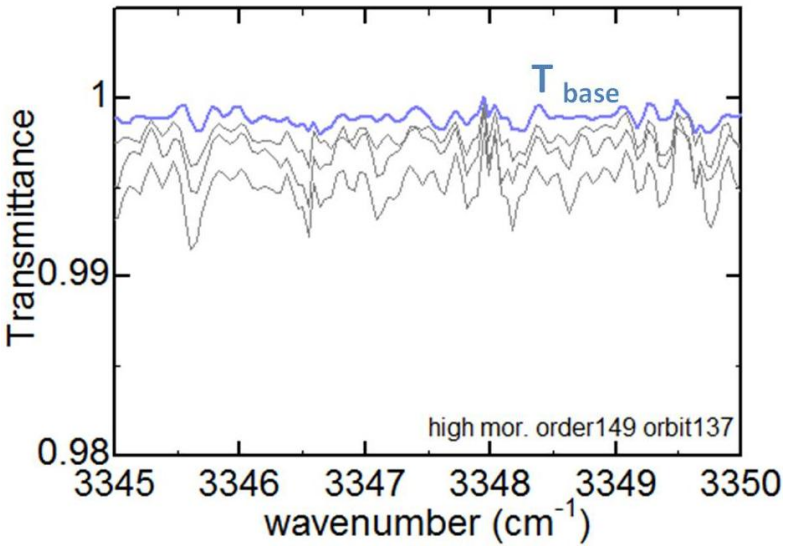

Fig.3.6.2 Example of baseline (T_{base}, blue line).

3.4. Onion peeling method

The solar occultation is the measurement technique used by SOIR to probe the Venus atmosphere. Each measurement can be assigned to a tangent point at the limb. As Fig.3.7 shows, the tangent altitude monotonically decreases in case of an ingress. The tangent altitude $h_{g,j}$ corresponding to the j-th measurement defines an atmospheric shell. The regions between two successive measurement altitudes $h_{tg,j-1}$ and $h_{tg,j}$ is defined to be the j-th layer (L_j).

τ_j, the horizontal optical thickness of layer L_j, is defined

$$\tau_j = -\ln(T_{base,j}) \qquad (3.4.1)$$

where T_{base} is calculated by eq.(3.3.3).

$\tau_{j,in}$, the horizontal optical thickness at all the layers inner than the L_j layer, is calculated using

$$\tau_{j,in} = \tau_j - \sum_{i}^{j-1} 2dx_i \times k_i \qquad (3.4.2)$$

where k_i is aerosol extinction of all the layers outer than the L_j layer, and dx_i is the horizontal length of outer the L_j layer.

Local extinction k_j is calculated by dividing the $\tau_{j,in}$ by local length X_j (see eq.(3.4.3)).

$$k_j = \frac{\tau_{j,in}}{X_j} \qquad (3.4.3)$$

The vertical distribution of extinction is obtained by repeating the above process. Fig.3.8.1 is an example of the distribution. The error is estimated by using following equations,

$$\Delta\tau_j = \frac{\Delta T_{base,\ j}}{T_{base,\ j}} \qquad (3.4.4)$$

$$\Delta\tau_{j,\ in} = \sqrt{(\Delta\tau_j)^2 + (\sum_{i=1}^{j-1}(\Delta k_i \times dx_i))^2} \qquad (3.4.5)$$

$$\Delta k_j = \sum_{i=1}^{j} \frac{\Delta\tau_{i,\ in}}{X_i} \qquad (3.4.6)$$

where ΔT_{base} is standard deviation of T_{base}. ΔT_{base} and Δk are estimated almost 0.001 and 40 % respectively.

The vertical optical thickness τ_{vert} is calculated by integrating the extinction vertically (see eq.(3.4.7)).

$$\tau_{vert} = \int k_j \quad dz \qquad (3.4.7)$$

The normalized extinction m_j is equivalent to mixing ratio and calculated by

$$m_j = \frac{k_j}{d_j} \qquad (3.4.8)$$

where d_j is CO_2 number density at L_j layer obtained in Section 3.3. Fig.3.8.2 is an example of the vertical distribution of normalized extinction. The errors of τ_{vert} and m_j are estimated in using eq.(3.4.9) and eq.(3.4.10).

$$\Delta\tau_{vert} = \sum_{i=1}^{j} \Delta k_i \qquad (3.4.9)$$

$$\Delta m_j = \sqrt{\left(\frac{\Delta k_j}{n_{co_2}}\right)^2 + \left(\frac{k_j \cdot \Delta n_{co_2}}{n_{co_2}}\right)^2} \qquad (3.4.10)$$

where Δn_{co2} is error of CO_2 number density.

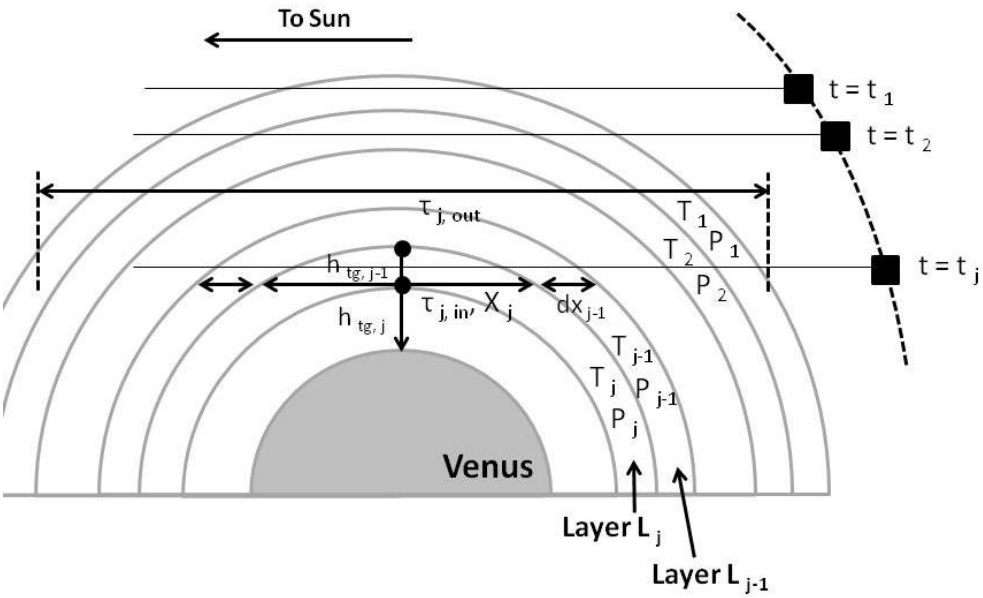

Fig.3.7 Geometry of the solar occultation measurements and definition of the onion peeling method. In the ingress case depicted here, the instrument is taking a measurement every second. The tangent altitudes $h_{tg,j}$ define layers in the atmosphere. The light path is divided into several segments, named X_j such that the time corresponds to $t = t_j$, and j the layer number. In each layer L_j, the quantities temperature T_j and pressure P_j are assumed to be constant [modified Mahieux et al. (2010)]

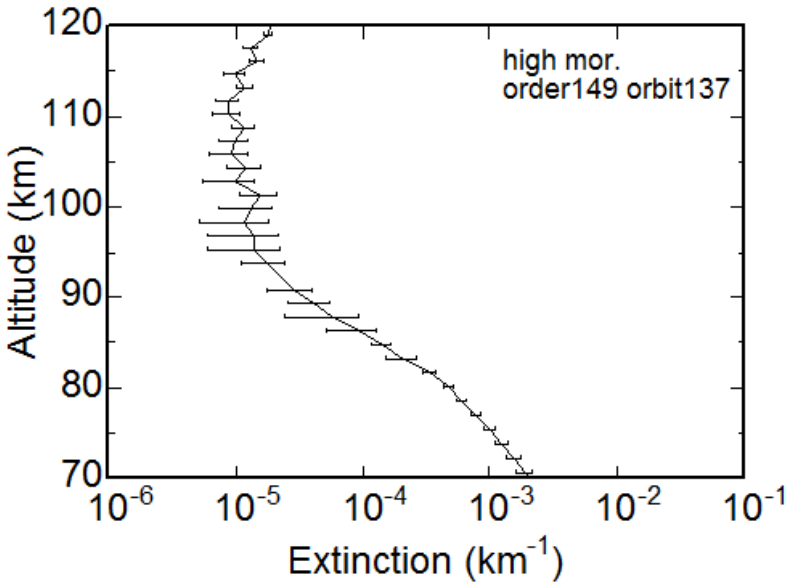

Fig.3.8.1 Example of vertical distribution of extinction (05 Sep. 2006, order149, orbit137, latitude 79°N, longitude 237°).

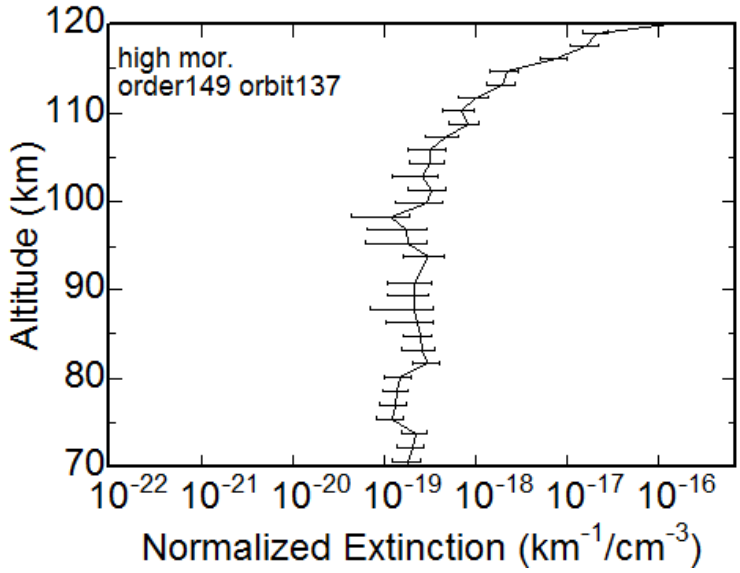

Fig.3.8.2 Example of vertical distribution of normalized extinction (05 Sep. 2006, order149, orbit137, latitude 79°N, longitude 237°).

3.5. Data selection

There are unsuitable data to be analyzed such as the following two types. One type is indicated in Fig.3.9.1 and second type is indicated in Fig.3.9.2.

Fig.3.9.1 shows an example that the number of absorption lines differ between T_{molec} and T_{obs}. The cause seems to be due to lack in the molecular database or interference from nearby orders.

Fig.3.9.2 shows another example that T_{obs} is not constant in the 3950 – 3960 cm^{-1} region. However, the vertical axis on Fig.3.9.2 is enlarged significantly, the bottom axis is defined 0.994. The curve seems to be due to the property of spectroscopy. This example is normal spectrum. In this study, the tiny variations of transmittance level at altitude above 90 km are intended. So, straight transmittances around the 5 central wavenumbers at the time of acquisition are used in this analysis.

The total number of occultations used in this study is 130.

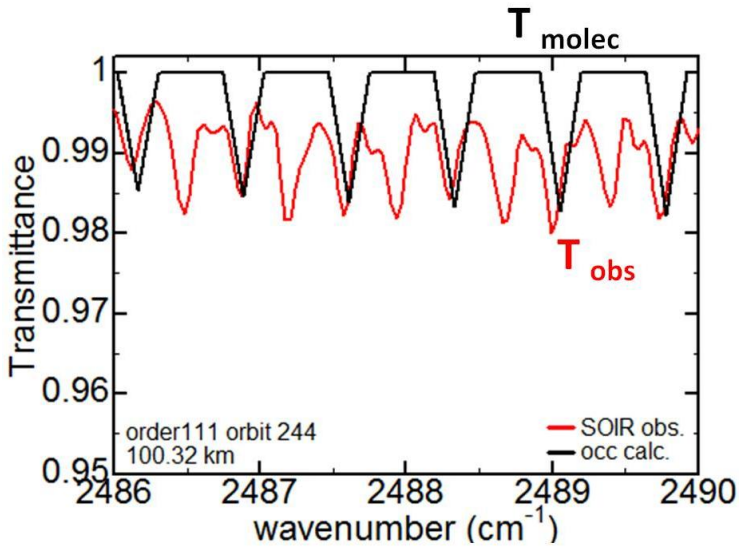

Fig.3.9.1 Example of unsuitable data to be analyzed. The number of absorption lines differ between T_{molec} (black line) and T_{obs} (red line).

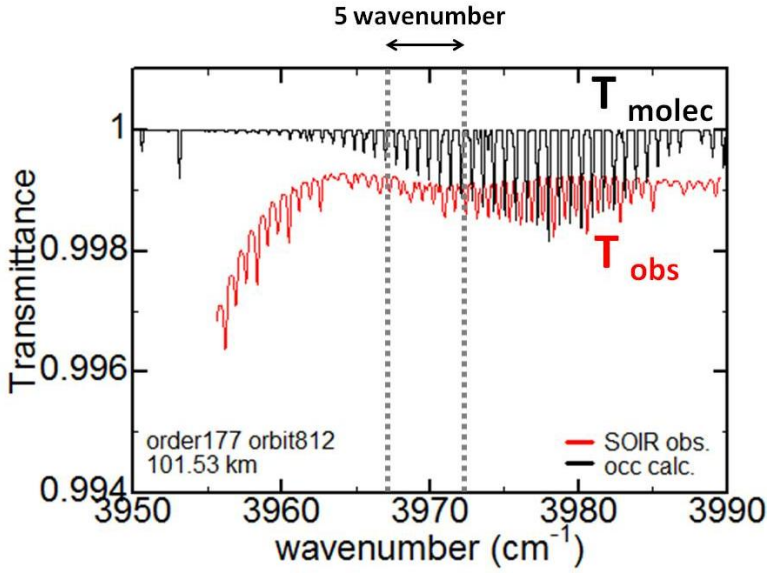

Fig.3.9.2 Example of unsuitable data to be analyzed. T_{obs} (red line) is not constant in the 3950 – 3960 cm^{-1} region.

4. Results

4.1. Extinction

4.1.1. Vertical distribution

Figs.4.1 (a)-(d) show vertical distributions of extinction calculated by using the method described in Section 3.4. Profiles are plotted up to 120 km. This study shows for the first time vertical distributions of extinctions at altitude above 90 km.

Figs.4.2 (a)-(d) show vertical distributions of extinction obtained from SOIR team. Derivation method differs from that of this study. The difference is described in Section 3.3. The profiles at 70 – 90 km are shown in Wilquet et al. (2012) (Fig.1.2) because it has long been recognized so far that the top of the upper haze is 90 km.

Extinction profiles at high latitude in the morning (Lat. > 60 °, LT < 12 h) are shown in Fig.4.1 (a) and Fig.4.2 (a). Similarly, those at high latitude in the evening (Lat. > 60 °, LT > 12 h), low latitude in the morning (Lat. < 60 °, LT < 12 h) and low latitude in the evening (Lat. < 60 °, LT > 12 h) are shown in Fig.4.1 (b) and Fig.4.2 (b), (c) and (d), respectively. Some profiles are plotted on a figure every ten orders. The reason why profiles are classified every ten orders is that total number of data is large. Some profiles are classified into two groups (① and ②) depending on observed time; ① shows that profiles are observed relatively early. The profiles at order 141 – 150 are indicated up to 120 km. All the diffraction orders with corresponding wavelengths are summarized in Appendix B. Each profile is color-coded according to orbit number. Orders and orbit numbers are written on the right hand of each figure. An error bar is plotted on each figure.

Extinction profiles (Figs.4.1) share common features though different orders. Accordingly, these features have high reliability.

(1) Extinctions vary order of magnitude every occultations.

(2) Extinctions are appeared to be independent of wavelength. This makes it clear that haze particles are sufficiently-small in size in comparison with observation wavelength. Wilquet et al. (2009) demonstrated the existence of at least two types of particles at high altitude: mode 1 of mean radius $0.1 \leqq r \leqq 0.3$ μm and mode 2 of $0.4 \leqq r \leqq 1.0$ μm.

(3) These profiles are characterized by folding at around 95 km.

Figs.4.1 and 4.2 share common features although computation methods differ from one another. Accordingly, these results are reliable.

(1) Upper haze exists at altitude above 90 km although it has long been recognized so far that the top of the upper haze is 90 km.

(2) These profiles are characterized by folding at around 95 km.

(3) Extinction profiles vary order of magnitude every occultations.

(4) At low latitude, profiles are separated into two sections; one is observed earlier than 2008 and the other is observed later than 2008.

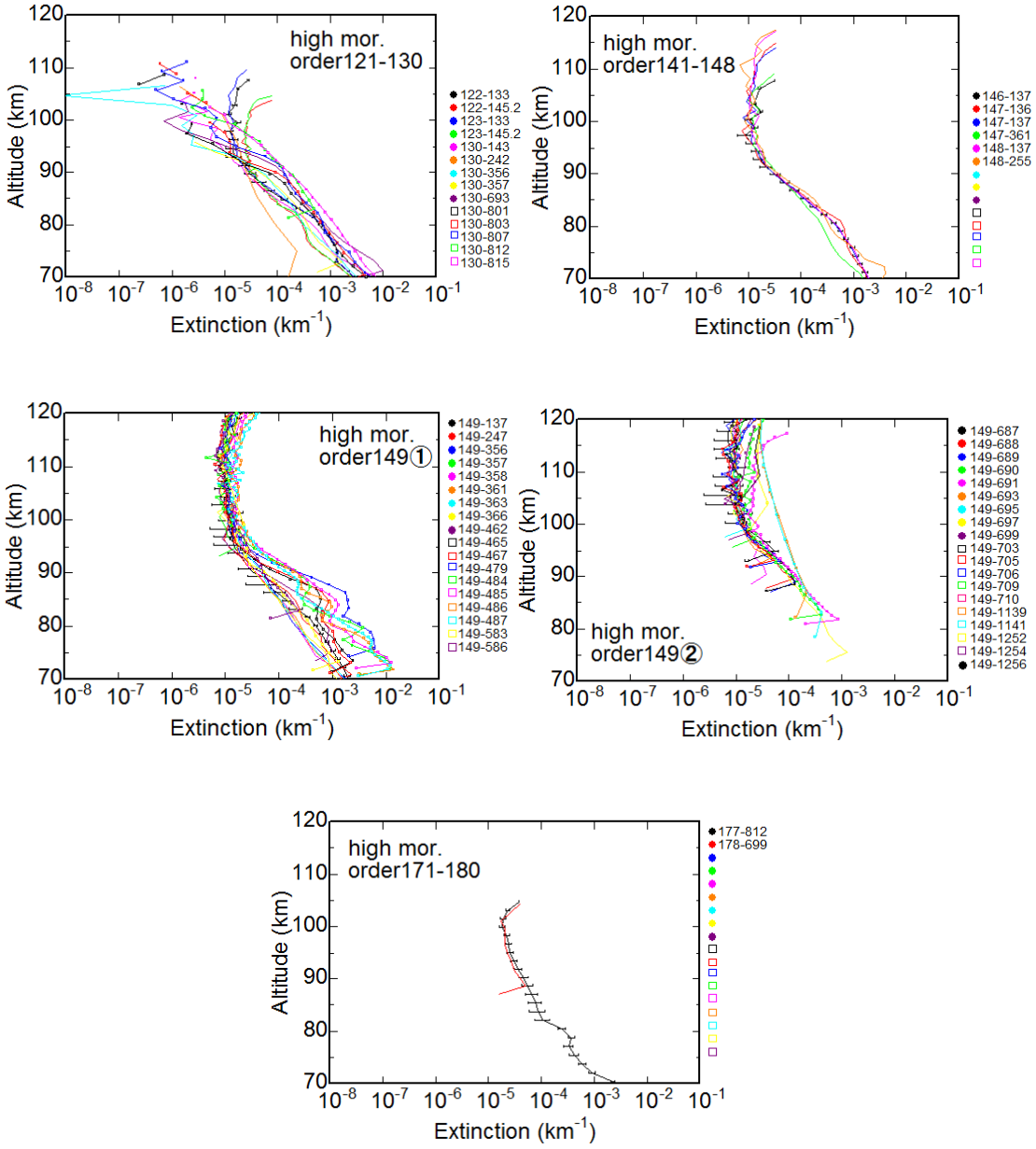

Fig.4.1 (a) Vertical distributions of observed extinctions at high latitude in the morning (Lat. > 60°, LT < 12 h). All the diffraction orders with corresponding wavelengths are summarized in Appendix B. Each profile is color-coded according to orbit number. Orders and orbit numers are written on the right hand of each figure. An error bar is plotted on each figure.

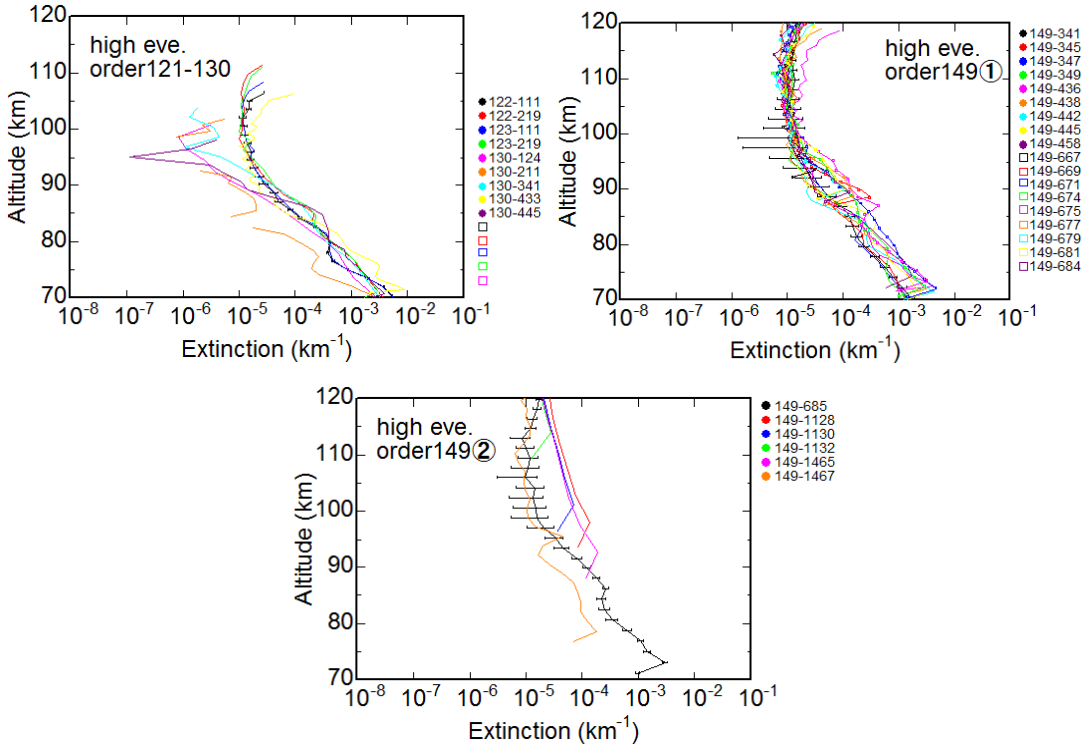

Fig.4.1 (b) Vertical distributions of observed extinctions at high latitude in the evening (Lat. > 60 °, LT > 12 h).

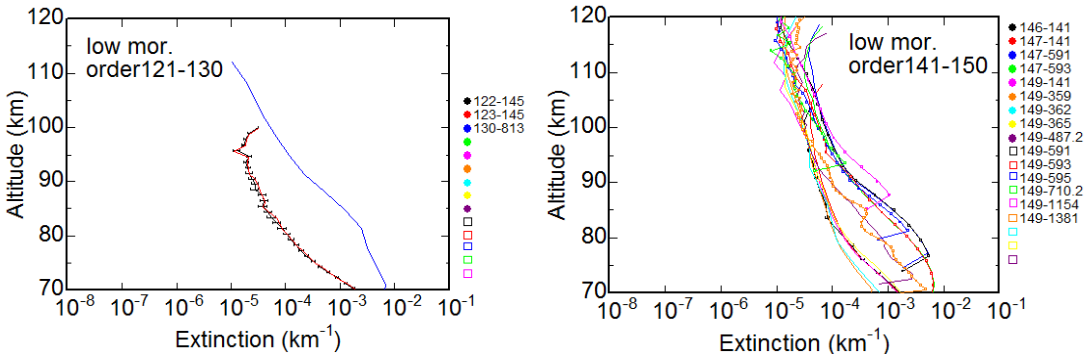

Fig.4.1 (c) Vertical distributions of observed extinctions at low latitude in the morning (Lat. < 60 °, LT < 12 h).

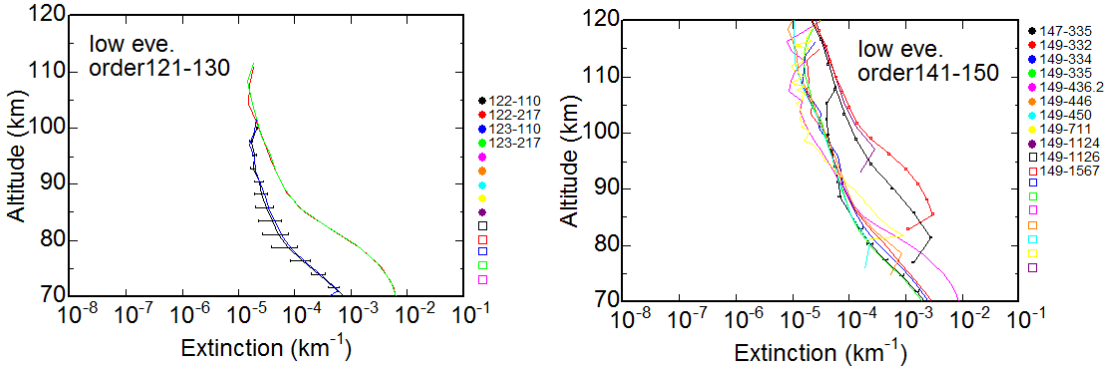

Fig.4.1 (d) Vertical distributions of observed extinctions at low latitude in the evening (Lat. < 60 °, LT > 12 h).

Vertical distributions of Extinction (SOIR team)

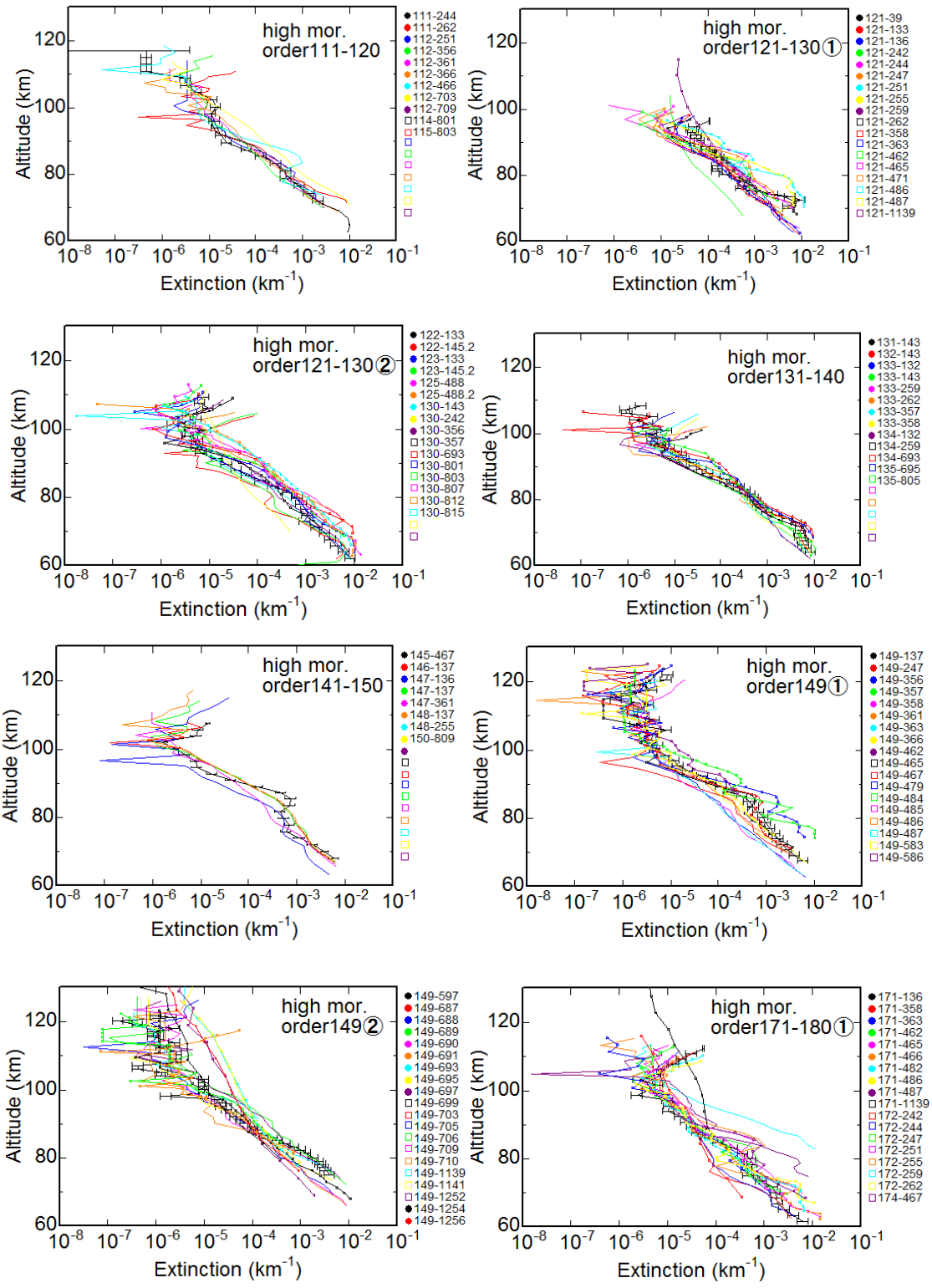
high mor.
order111-120
111-244
111-262
112-251
112-356
112-361
112-366
112-466
112-703
112-709
114-801
115-803
high mor.
order121-130①
121-39
121-133
121-136
121-242
121-244
121-247
121-251
121-255
121-259
121-262
121-358
121-363
121-462
121-465
121-471
121-486
121-487
121-1139
high mor.
order121-130②
122-133
122-145.2
123-133
123-145.2
125-488
125-488.2
130-143
130-242
130-356
130-357
130-693
130-801
130-803
130-807
130-812
130-815
high mor.
order131-140
131-143
132-143
133-132
133-143
133-259
133-262
133-357
133-358
134-132
134-259
134-693
135-695
135-805
high mor.
order141-150
145-467
146-137
147-136
147-137
147-361
148-137
148-255
150-809
high mor.
order149①
149-137
149-247
149-356
149-357
149-358
149-361
149-363
149-366
149-462
149-465
149-467
149-479
149-484
149-485
149-486
149-487
149-583
149-586
high mor.
order149②
149-597
149-687
149-688
149-689
149-690
149-691
149-693
149-695
149-697
149-699
149-703
149-705
149-706
149-709
149-710
149-1139
149-1141
149-1252
149-1254
149-1256
high mor.
order171-180①
171-136
171-358
171-363
171-462
171-465
171-466
171-482
171-486
171-487
171-1139
172-242
172-244
172-247
172-251
172-255
172-259
172-262
174-467
Altitude (km)
Extinction (km^{-1})

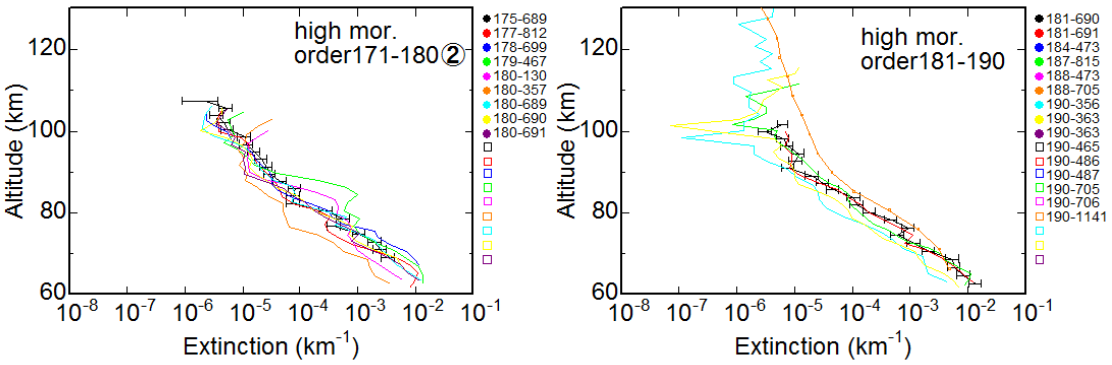

Fig.4.2 (a) Vertical distributions of observed extinctions by SOIR team at high latitude in the morning (Lat. > 60°, LT < 12 h). All the diffraction orders with corresponding wavelengths are summarized in Appendix B. Each profile is color-coded according to orbit number. Orders and orbit numbers are written on the right hand of each figure. An error bar is plotted on each figure.

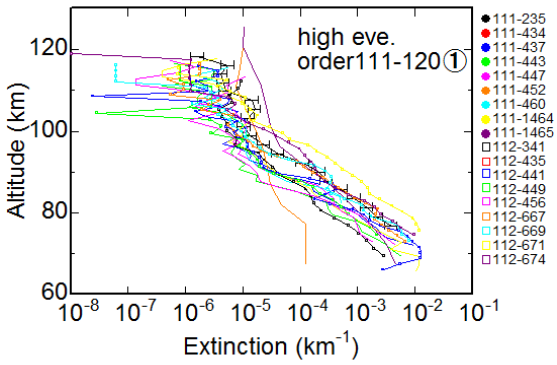
high eve.
order111-120①
Altitude (km)
Extinction (km^{-1})
111-235
111-434
111-437
111-443
111-447
111-452
111-460
111-1464
111-1465
112-341
112-435
112-441
112-449
112-456
112-667
112-669
112-671
112-674

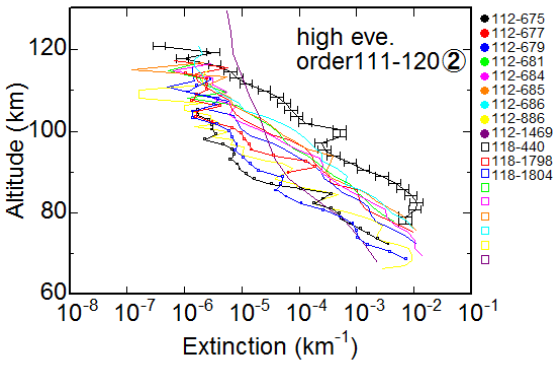
high eve.
order111-120②
Altitude (km)
Extinction (km^{-1})
112-675
112-677
112-679
112-681
112-684
112-685
112-686
112-886
112-1469
118-440
118-1798
118-1804

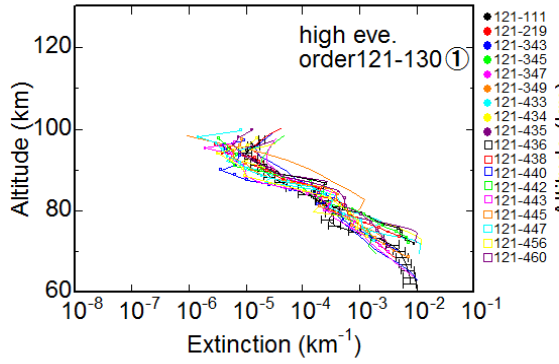
high eve.
order121-130①
Altitude (km)
Extinction (km^{-1})
121-111
121-219
121-343
121-345
121-347
121-349
121-433
121-434
121-435
121-436
121-438
121-440
121-442
121-443
121-445
121-447
121-456
121-460

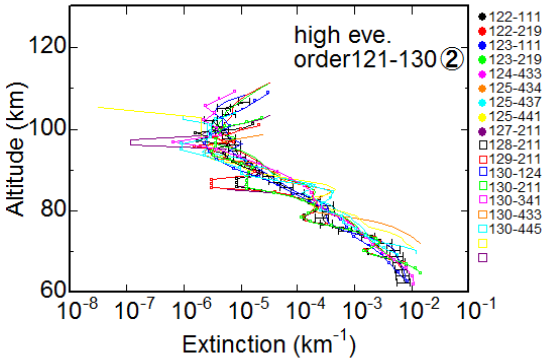
high eve.
order121-130②
Altitude (km)
Extinction (km^{-1})
122-111
122-219
123-111
123-219
124-433
125-434
125-437
125-441
127-211
128-211
129-211
130-124
130-211
130-341
130-433
130-445

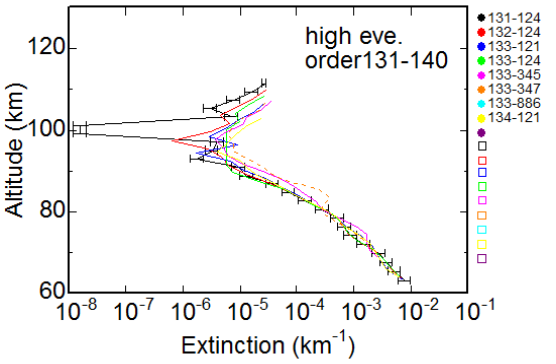
high eve.
order131-140
Altitude (km)
Extinction (km^{-1})
131-124
132-124
133-121
133-124
133-345
133-347
133-886
134-121

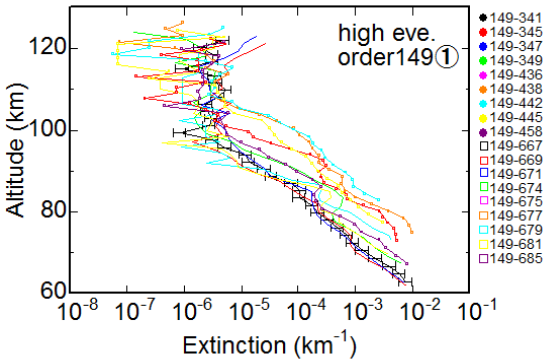
high eve.
order149①
Altitude (km)
Extinction (km^{-1})
149-341
149-345
149-347
149-349
149-436
149-438
149-442
149-445
149-458
149-667
149-669
149-671
149-674
149-675
149-677
149-679
149-681
149-685

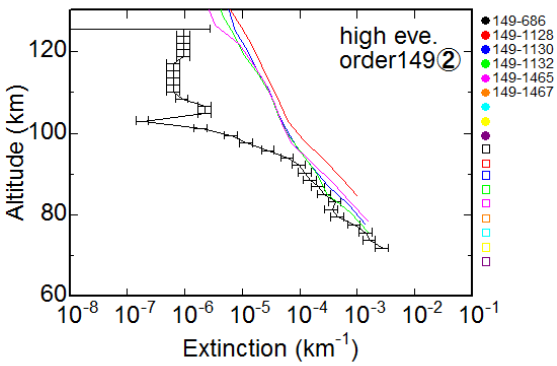
high eve.
order149②
Altitude (km)
Extinction (km^{-1})
149-686
149-1128
149-1130
149-1132
149-1465
149-1467

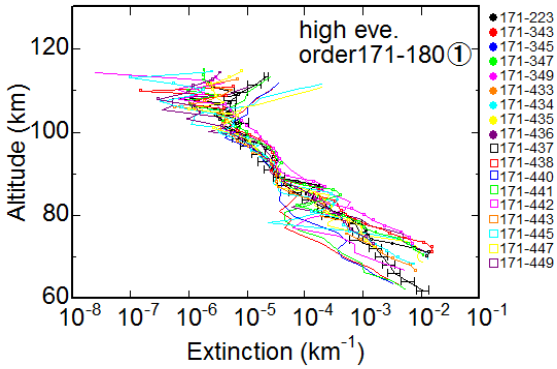
high eve.
order171-180①
Altitude (km)
Extinction (km^{-1})
171-223
171-343
171-345
171-347
171-349
171-433
171-434
171-435
171-436
171-437
171-438
171-440
171-441
171-442
171-443
171-445
171-447
171-449

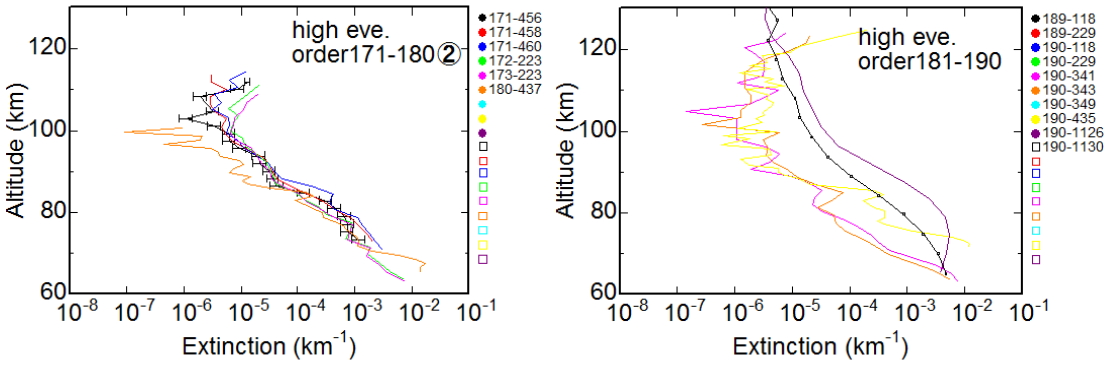

Fig.4.2 (b) Vertical distributions of observed extinctions by SOIR team at high latitude in the evening (Lat. > 60 °, LT > 12 h).

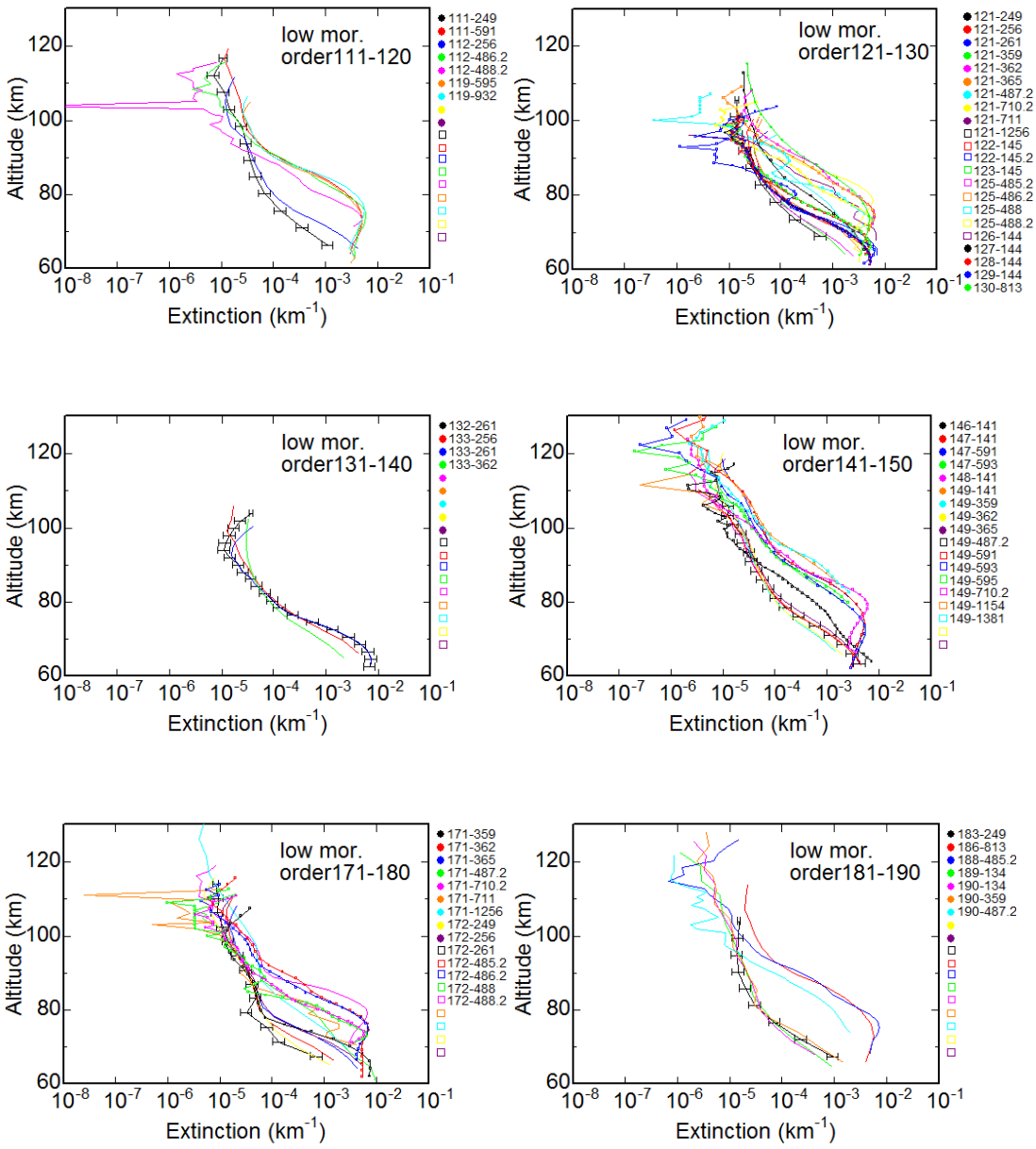

Fig.4.2 (c) Vertical distributions of observed extinctions by SOIR team at low latitude in the morning (Lat. < 60 °, LT < 12 h).

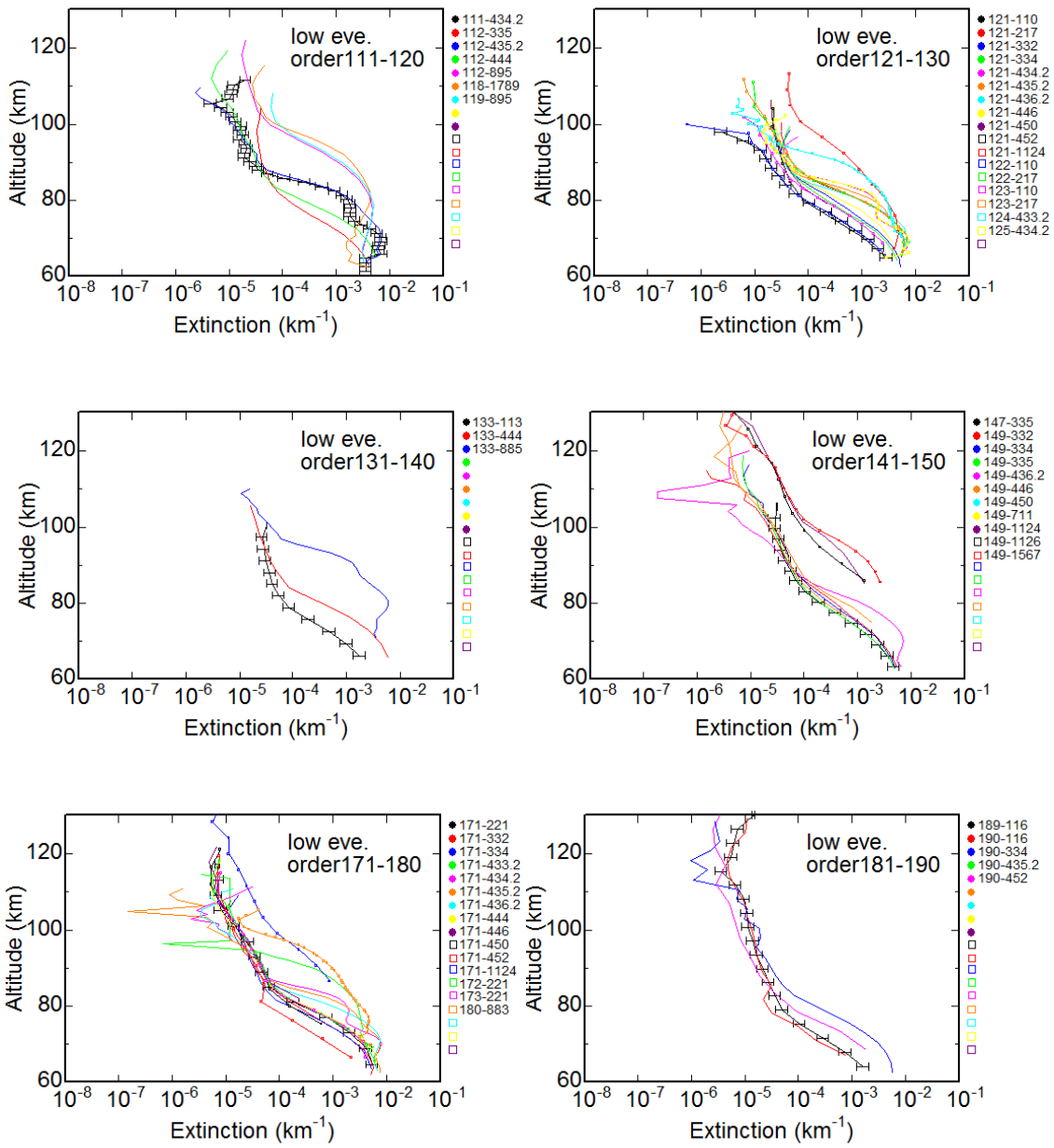

Fig.4.2 (d) Vertical distributions of observed extinctions by SOIR team at low latitude in the evening (Lat. < 60 °, LT > 12 h).

4.1.2. Averages

The mean of all extinction profiles at the present work (Figs.4.1) is shown in Fig.4.3. Similarly, the mean of all extinction profiles of the SOIR team (Figs.4.2) is shown in Fig.4.4. Error bar is plotted only at high latitude in the morning. The error is mean of each error. A comparison of two is plotted on Fig.4.5.

Fig.4.3 and 4.4 share common features although computation methods are different from each other. Accordingly, these results are reliable.

(1) Upper haze exists at altitude above 90 km although it has long been recognized so far that the top of the upper haze is 90 km.

(2) Extinction profiles fold at around 95 km.

(3) Their values at low latitudes are larger than those at high latitude. It would appear that aerosols are more produced at low latitude than at high latitude. These features given above appear to be clearer than those shown by Wilquet et al. (2012) owing to analysis with wider altitude and latitude ranges in this study than in the previous study.

(4) Both values of extinctions are almost the same (see Fig.4.5), although derivation methods are different from each other. For example, at high latitude in the morning at 90 km, the value obtained from this study and SOIR team is 8.75×10^{-5} and 8.25×10^{-5}, respectively. However, at 120 km, extinctions obtained from this study are order of magnitude larger than these from SOIR team. It would appear that this difference is caused by difference in method to define baseline and to select data. However, we need to get into details about analysis algorithm of SOIR team to give a quantitative rating

the difference. It is an issue in the future.

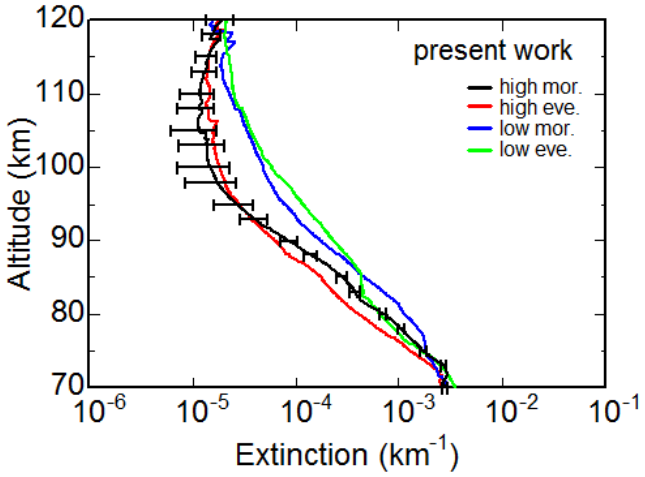

Fig.4.3 Mean of all extinctions of the present work (Figs.4.1); high latitude morning (black line), high latitude evening (red line), low latitude morning (blue line) and low latitude evening (green line). The error is calculated in using eq.(3.4.6) described in Section 3.4 and shown only for high latitude morning.

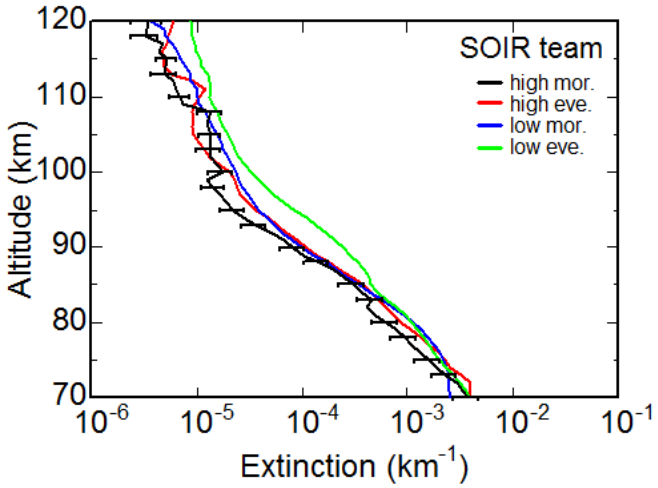

Fig.4.4 Mean of all extinctions of the SOIR team (Figs.4.2); high latitude morning (black line), high latitude evening (red line), low latitude morning (blue line) and low latitude evening (green line).

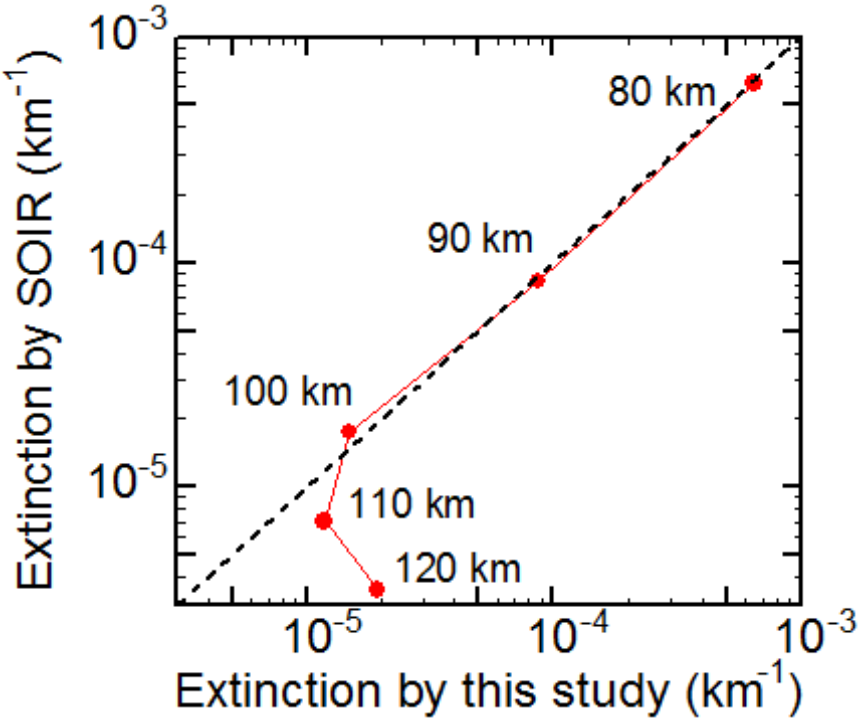

Fig.4.5 A comparison of extinctions obtained from this study and SOIR team. Both values are almost the same, although computation methods are different from each other.

4.2. Optical thickness

Fig.4.6 and 4.7 show latitude distributions of vertical optical thickness of the present work between 70 and 90 km and between 90 and 110 km, respectively. To calculate the optical thickness, extinctions (Figs.4.1) are used. Similarly, Fig.4.8 and 4.9 show latitude distributions of vertical optical thickness of the SOIR team between 70 and 90 km and between 90 and 110 km, respectively. To calculate the optical thickness, extinctions (Figs.4.2) are used. Optical thicknesses are plotted every latitude 20 °.

Fig.4.6, 4.7, 4.8 and 4.9 share common features.

(1) Optical thicknesses have similar values between 70 and 90 km in both Fig.4.6 and 4.8. As shown in Fig.4.6, the average of optical thickness in the morning is 0.0201 and 0.0305 in the evening. As show in Fig.4.8, the average of optical thickness in the morning is 0.0284 and 0.0351 in the evening.

(2) Optical thicknesses have similar values between 90 and 110 km in both Fig.4.7 and 4.9. As shown in Fig.4.7, the average of optical thickness in the morning is 9.76×10^{-4} and 8.74×10^{-4} in the evening. As show in Fig.4.9, the average of optical thickness in the morning is 8.48×10^{-4} and 7.33×10^{-4} in the evening.

(3) Optical thicknesses vary enormously and are independent of latitude. However, Kawabata et al. (1980) showed that optical thickness at high latitude is larger than that at low latitude in using PV OCPP polarization data. Observation methods of SOIR and PV are solar occultation technique and nadir observation, respectively. There is a possibility that observed altitudes and objects of two satellites are different. Braak et al. (2002) pointed out long-term temporal variations of upper haze optical thickness. Upper

haze optical thicknesses vary 0.3 times from 1980 to 1992. There is a possibility that optical thickness at high latitude were larger in the past.

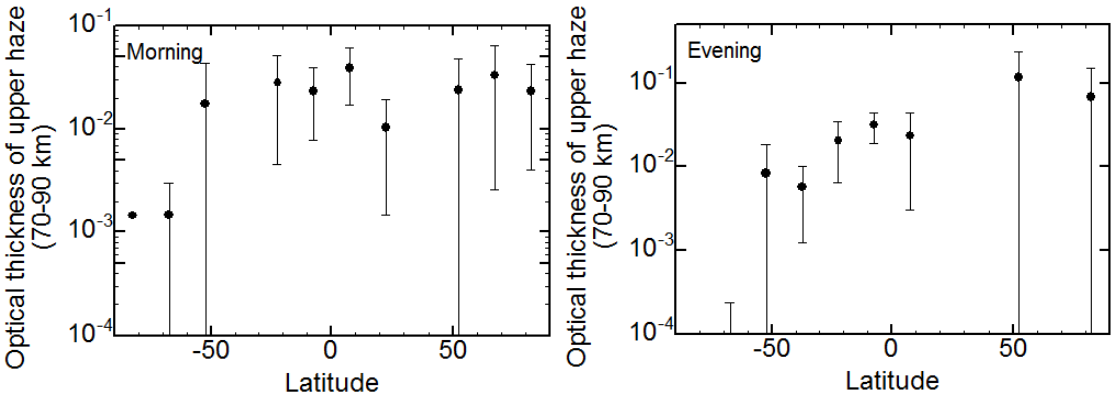

Fig.4.6 Latitudinal distributions of vertical optical thickness of the present work between 70 km and 90 km in the morning (left) and in the evening (right).

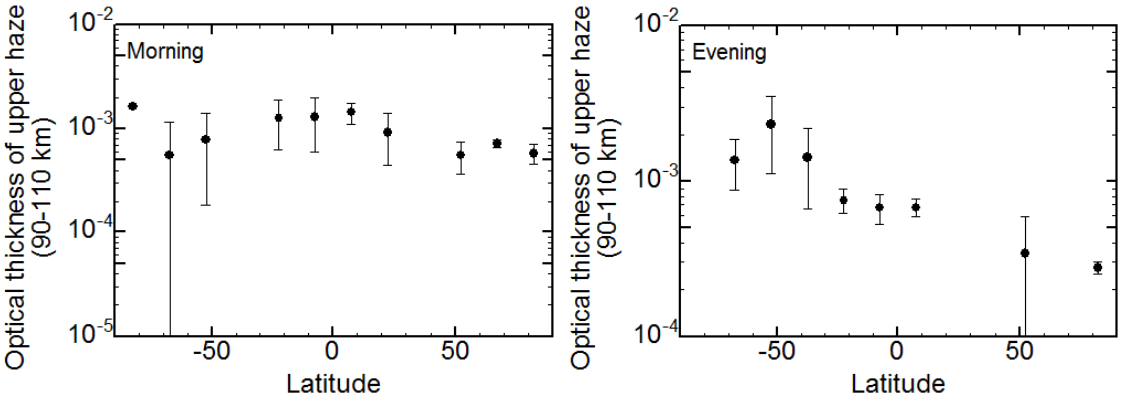

Fig.4.7 Latitudinal distributions of vertical optical thickness of the present work between 90 km and 110 km in the morning (left) and in the evening (right).

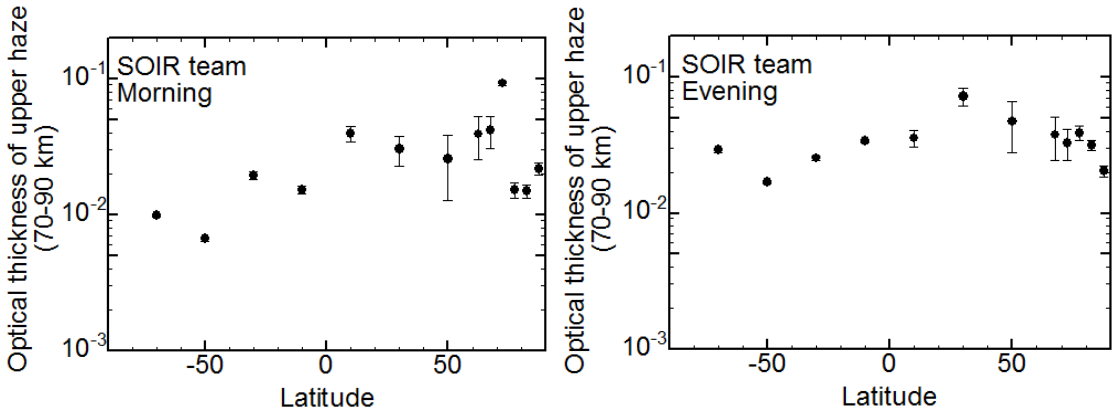

Fig.4.8 Latitudinal distribution of vertical optical thickness of the SOIR team from 70 km to 90 km in the morning (left) and in the evening (right).

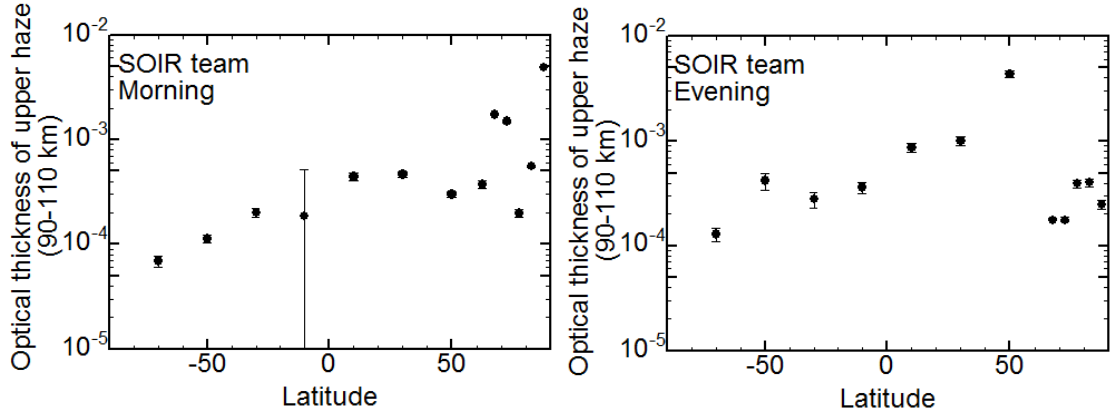

Fig.4.9 Latitudinal distribution of vertical optical thickness of the SOIR team from 90 km to 110 km in the morning (left) and in the evening (right).

4.3. CO_2 number density

4.3.1. Vertical distribution

Figs.4.11 (a)-(d) show vertical distributions of CO_2 number densities determined in Section 3.3 in this study.

Figs.4.12 (a)-(d) show vertical distribution of CO_2 number densities processed by SOIR team. To calculate CO_2 number densities, Zasova model [Zasova et al., 2007, 2006] and Keating model [Keating et al., 1985] are used. Derivation method is described in Mahieux et al. (2012).

CO_2 number density profiles at high latitude in the morning are shown in Fig.4.11 (a) and Fig.4.12 (a). Similarly, those at high latitude in the evening, low latitude in the morning and low latitude in the evening are shown in Fig.4.11 and Fig.4.12 (b), (c) and (d), respectively. Some profiles are plotted on a figure every ten orders. The reason why profiles are classified each ten orders is that total number of data is large. Some profiles are classified into two groups (① and ②) depending on observed time; ① shows that profiles are observed relatively early. The profiles at order 141 – 150 are indicated up to 120 km. All the diffraction orders with corresponding wavelengths are summarized in Appendix B. Each profile is color-coded according to orbit number. Orders and orbits are written on the right hand of each figure. An error bar is plotted on each figure.

CO_2 number densities (Figs.4.11) are compared by order.

(1) CO_2 number densities vary almost two-digits at both high and low latitudes. This feature is same as Mahieux et al. (2012). It's not known exactly why CO_2 number densities vary enormously.

(2) There are folds at around 95 km at high latitude at order 141 – 149. It's not known the cause of folding.

Figs.4.11 and 4.12 share common features although computation methods differ from one another. Accordingly, these results are reliable.

(1) CO_2 number densities vary almost two-digits at both high and low latitudes. This feature is same as Mahieux et al. (2012). It's not known exactly why CO_2 number densities vary enormously.

Figs.4.11 and 4.12 have different characteristics. However, the cause of difference is unclear.

(1) There are folds at around 95 km in Figs.4.11, especially at high latitude at order 141 – 149. On the other hand, Figs.4.12 show that profiles are regular in shape.

(2) CO_2 number densities obtained from this study are almost two orders magnitude smaller than those processed by SOIR team.

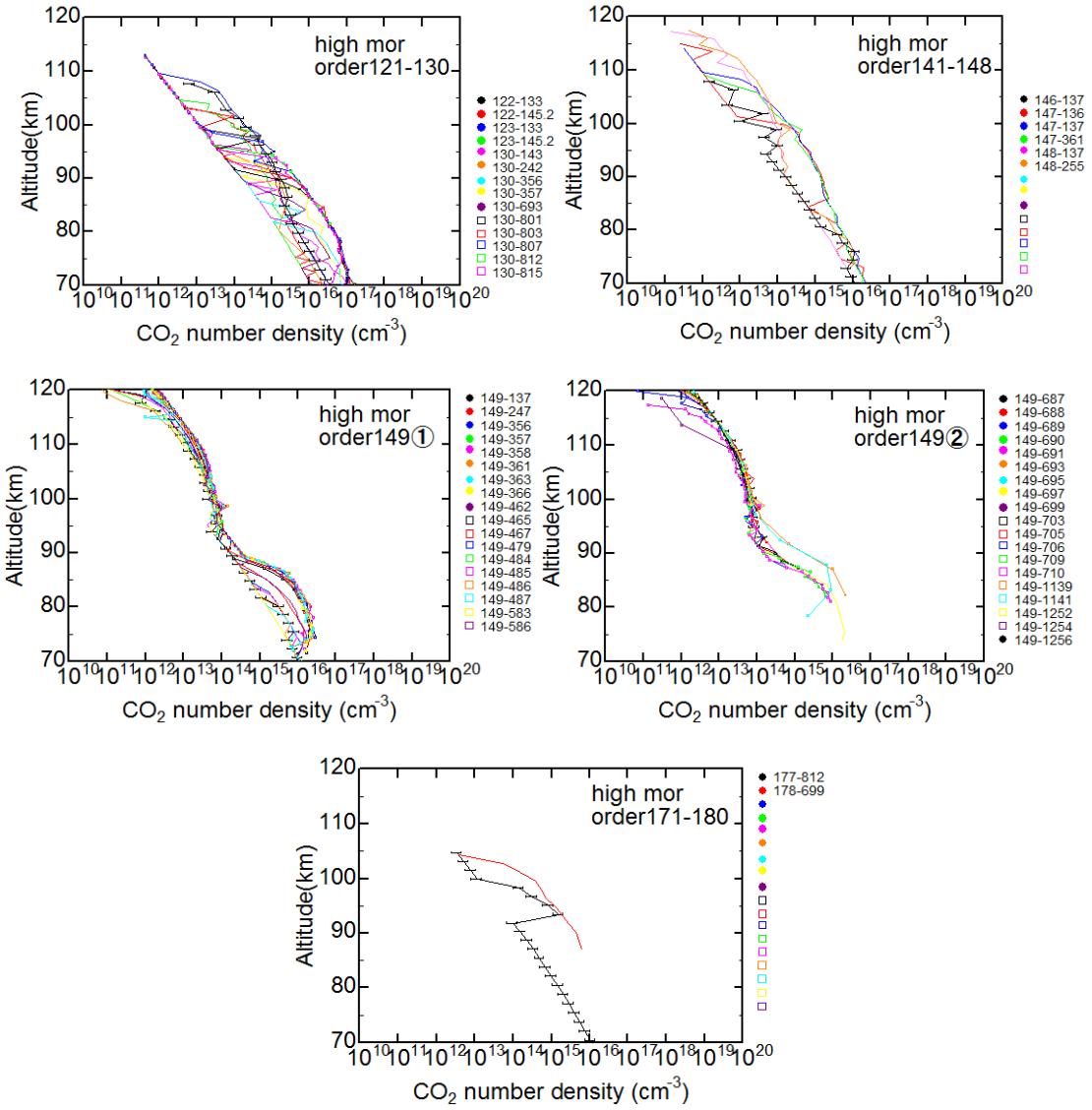

Fig.4.11 (a) Vertical distributions of CO_2 number density of the present work at high latitude in the morning (Lat. > 60 °, LT < 12 h). All the diffraction orders with corresponding wavelengths are summarized in Appendix B. Each profile is color-coded according to orbit number. Orders and orbit numbers are written on the right hand of each figure. An error bar is plotted on each figure.

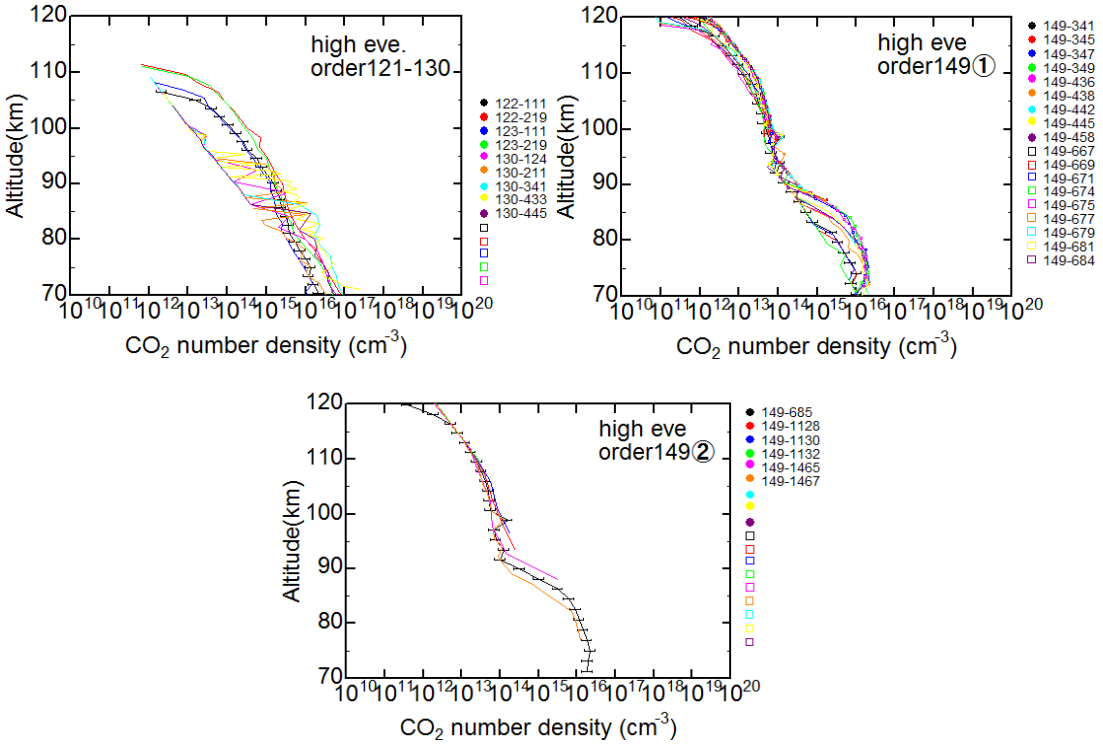

Fig.4.11 (b) Vertical distributions of CO_2 number density of the present work at high latitude in the evening (Lat. > 60 °, LT < 12 h).

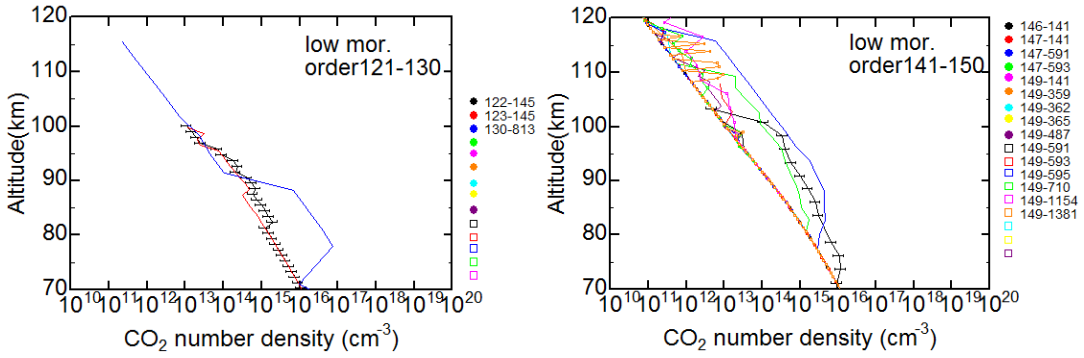

Fig.4.11 (c) Vertical distributions of CO_2 number density of the present work at low latitude in the morning (Lat. > 60 °, LT < 12 h).

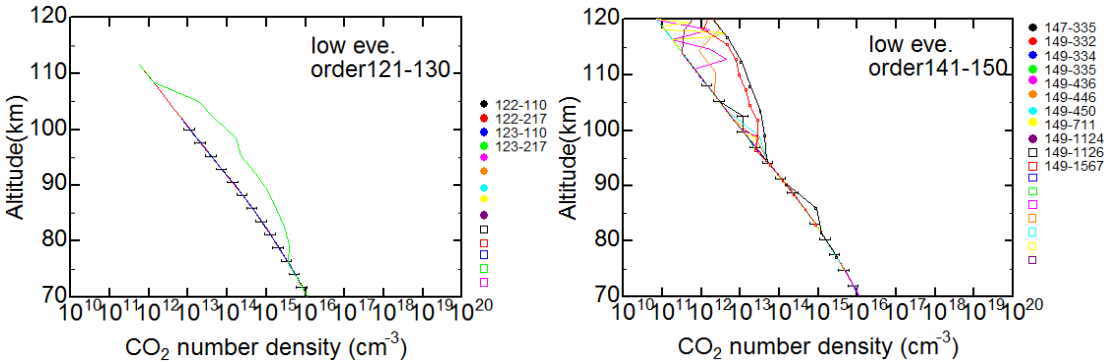

Fig.4.11 (d) Vertical distributions of CO_2 number density of the present work at low latitude in the evening (Lat. > 60 °, LT < 12 h).

Vertical distributions of CO_2 number density (SOIR team)

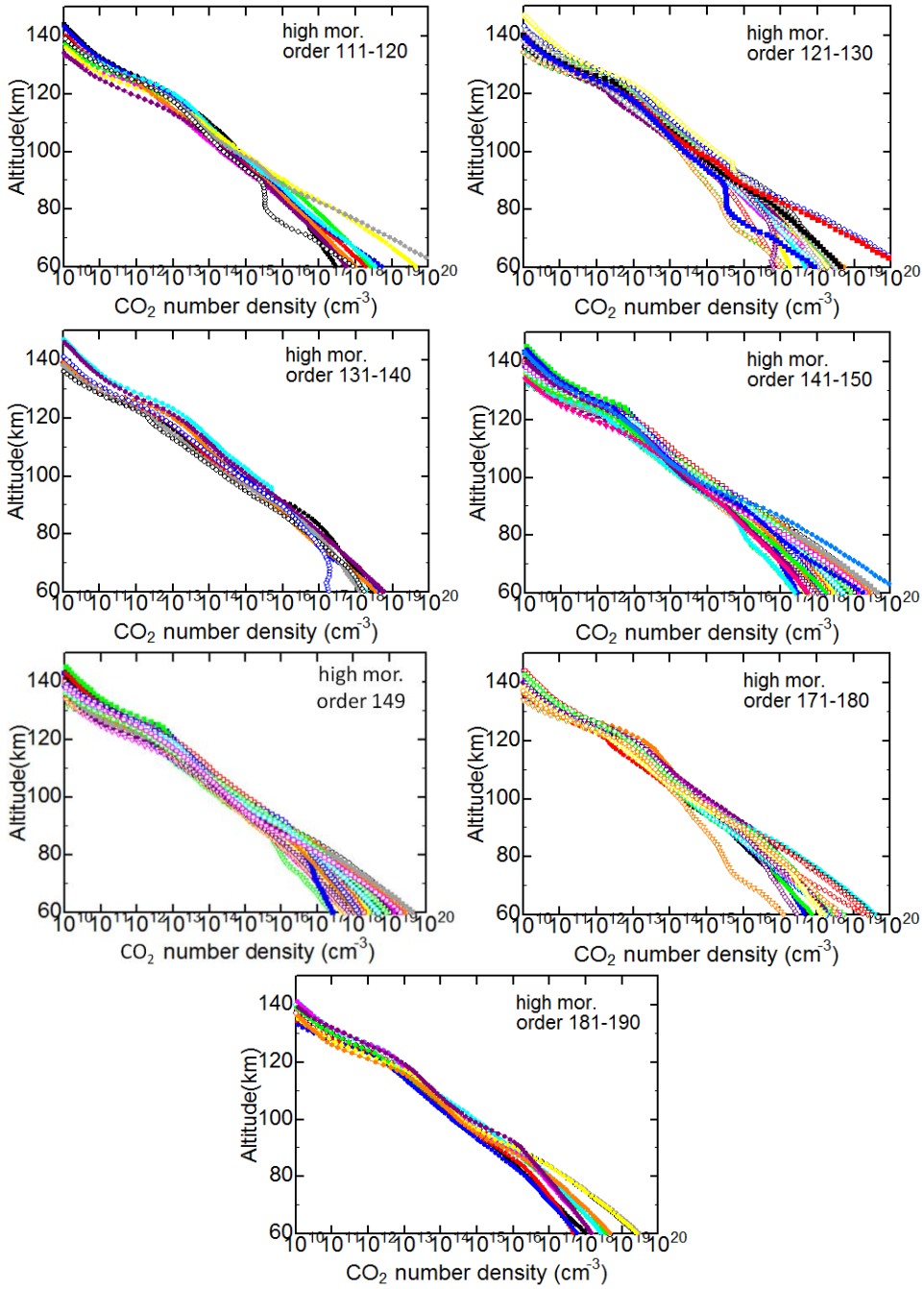

Fig.4.12 (a) Vertical distributions of observed CO_2 number density by the SOIR team at high latitude in the morning (Lat. > 60°, LT < 12 h). All the diffraction orders with corresponding wavelengths are summarized in Appendix B. Each profile is color-coded according to orbit number.

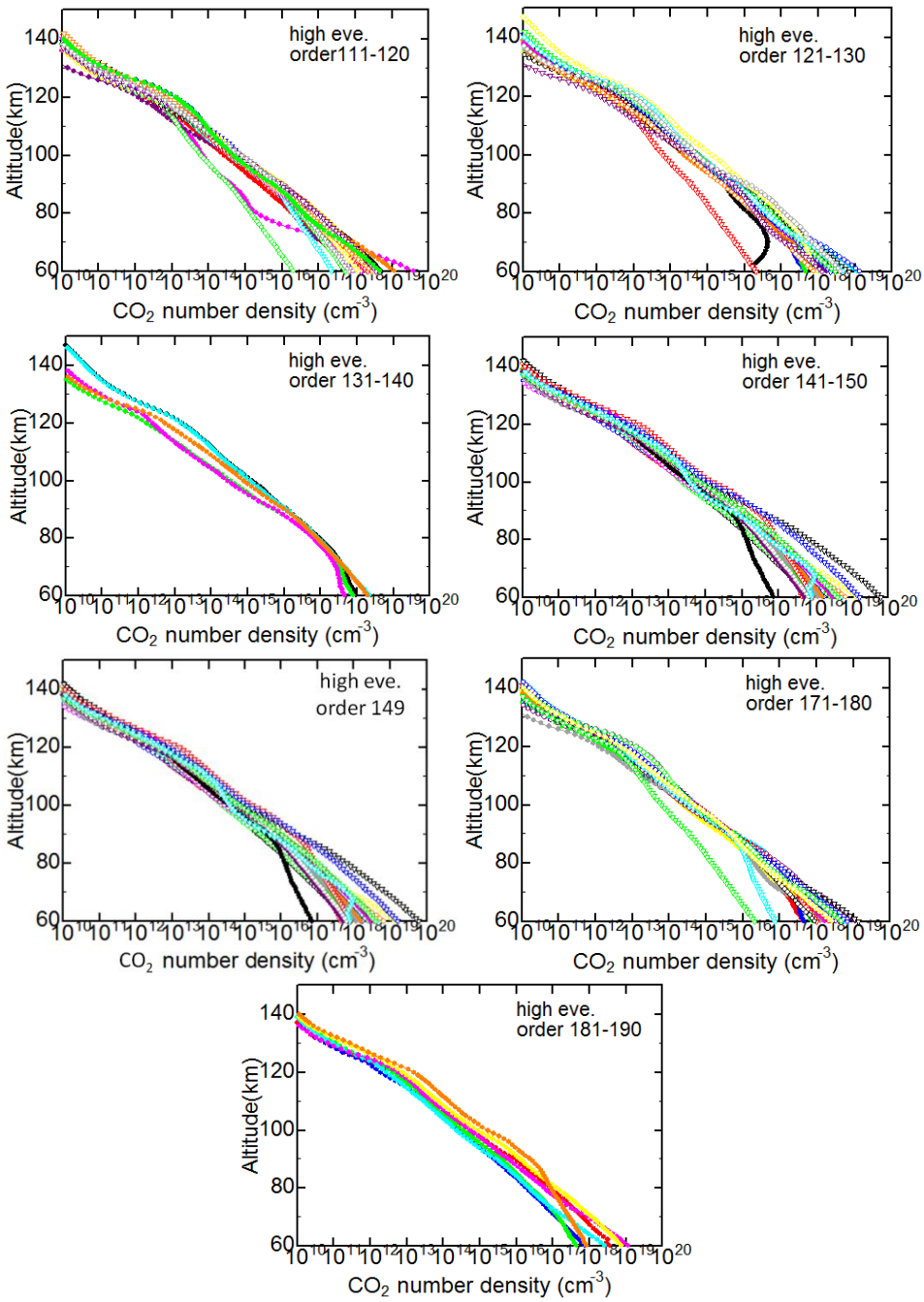

Fig.4.12 (b) Vertical distributions of observed CO_2 number density by the SOIR team at high latitude in the evening (Lat. > 60 °, LT > 12 h).

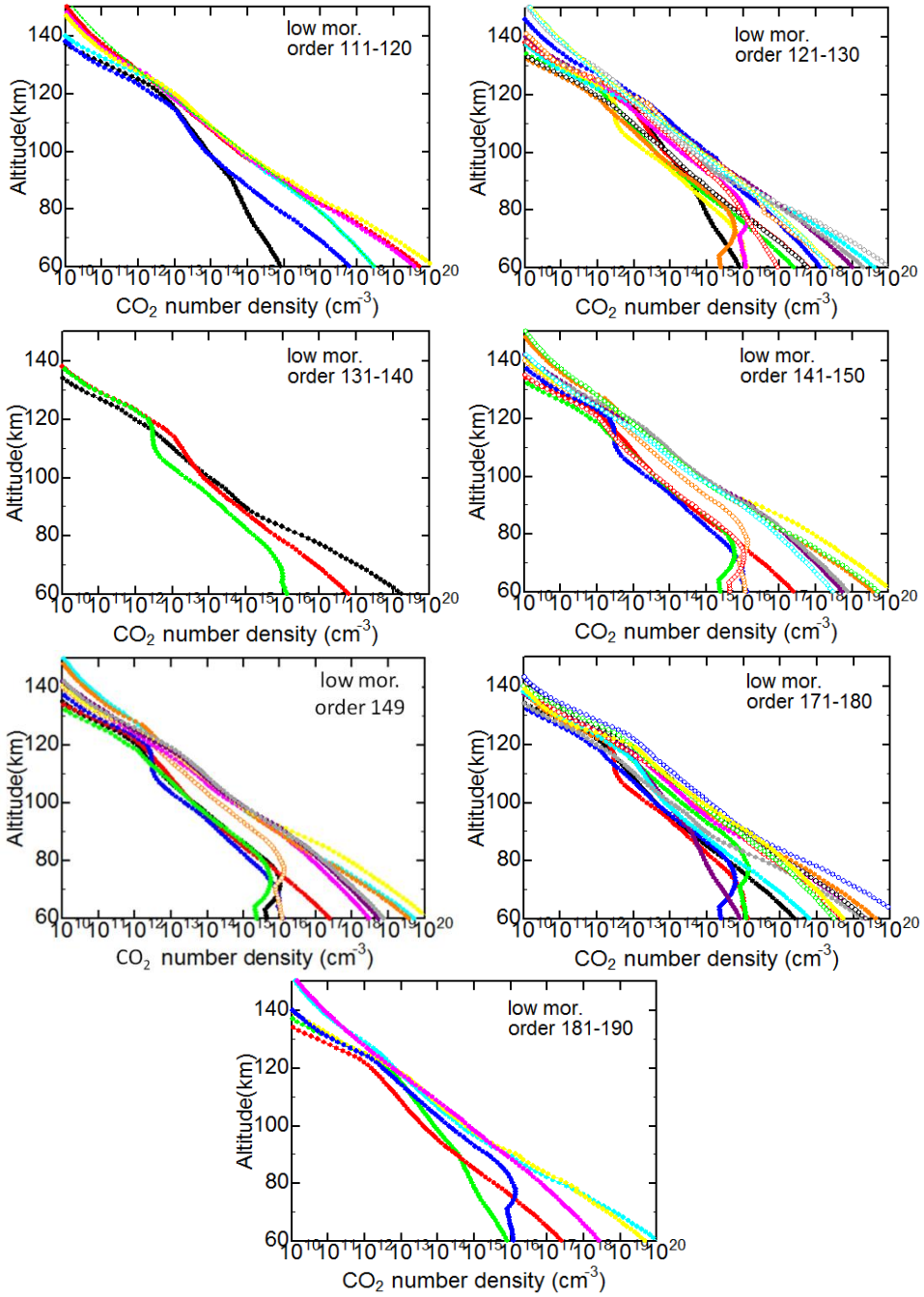

Fig.4.12 (c) Vertical distributions of observed CO_2 number density by the SOIR team for low latitude morning (Lat. < 60 °, LT < 12 h).

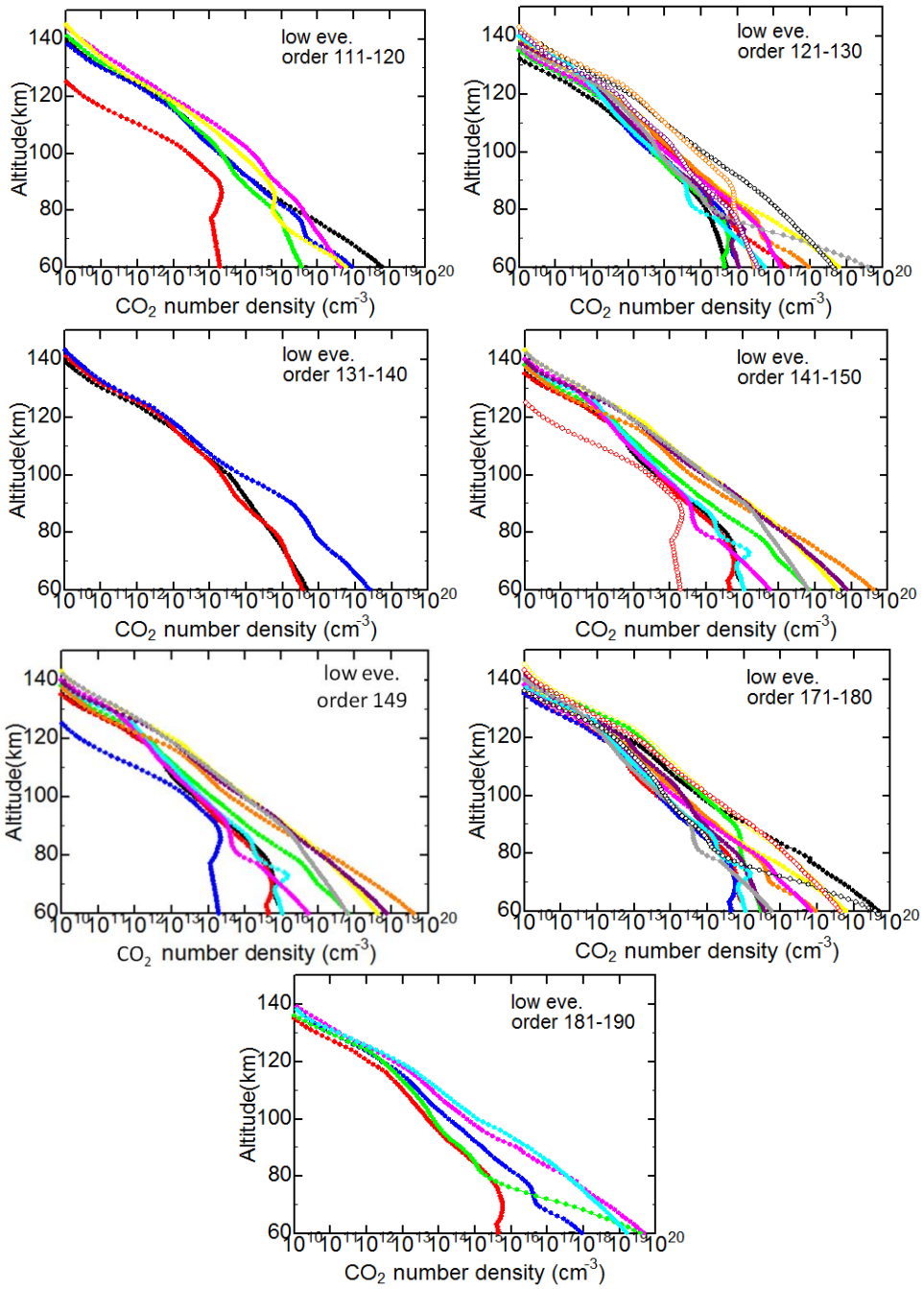

Fig.4.12 (d) Vertical distributions of observed CO_2 number density by the SOIR team for low latitude evening (Lat. < 60°, LT > 12 h).

4.3.2. Averages

The mean of all CO_2 number densities profiles by the present work (Figs.4.11) is shown in Fig.4.13. Similarly, that by the SOIR team (Figs.4.12) is shown in Fig.4.14. Error bar is plotted only at high latitude in the morning. This error is mean of each error. The pink dashed line on Fig.4.13 and 4.14 represents CO_2 number density value of the VIRA 1985 model [Keating et al., 1985].

Fig.4.13 and 4.14 have different characteristics. It would appear that this difference is caused by difference in absorption database and method to select data. However, we need to get into details about analysis algorithm of SOIR team to give a quantitative rating the difference. It is an issue in the future.

(1) CO_2 number densities obtained from this study (Fig.4.13) are almost two orders magnitude smaller than those processed by the SOIR team. For example, at high latitude in the morning at 90 km, the each value obtained from this study, SOIR team and VIRA 1985 model is 1.09×10^{15}, 5.76×10^{15} and 1.60×10^{16}, respectively. Further, CO_2 number densities obtained from Soret et al. (2012) are comparable in magnitude to those of this study.

(2) As shown in Fig.4.13, CO_2 number densities obtained from this study at low latitude are smaller than those at high latitude. On the other hand, CO_2 number densities obtained from SOIR team (Fig.4.14) at low latitude are equal to those at high latitude.

(3) There are folds at around 95 km at high latitude in Fig.4.13. On the other hand, Fig.4.14 shows that profiles are regular in shape.

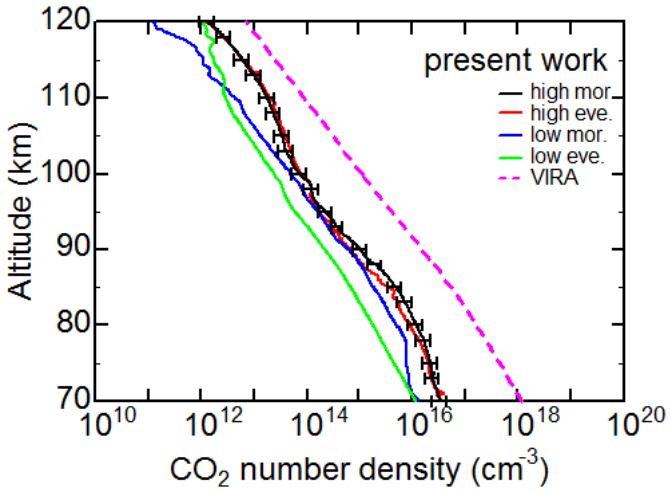

Fig.4.13 Mean of all CO_2 number density profiles of the present work (Figs.4.11); high latitude morning (black line), high latitude evening (red line), low latitude morning (blue line) and low latitude evening (green line). The error is shown only for high latitude morning. Errors appear to be 30 %. VIRA 1985 CO_2 density profile is also plotted (pink dashed line).

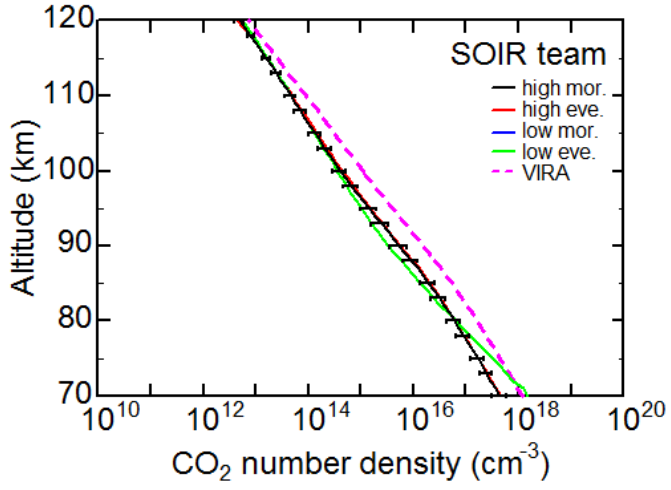

Fig.4.14 Mean of all CO_2 number density profiles by the SOIR team (Figs.4.12); high latitude morning (black line), high latitude evening (red line), low latitude morning (blue line) and low latitude evening (green line). The error is shown only for high latitude in morning. Error is estimated by the SOIR team. CO_2 density profile of VIRA 1985 model is also plotted in the figure (pink dashed line).

4.4. Normalized Extinction

4.4.1. Vertical distribution

As shown in the last chapter, values of CO_2 number density obtained from this study and SOIR team are different from VIRA 1985 model. Since, it is difficult to decide whether the difference is significant or not, VIRA 1985 model will also be used in this chapter.

Figs.4.15 show vertical distribution of normalized extinction of this study. To calculate these normalized extinctions, extinctions (Figs.4.1) and CO_2 number densities (Figs.4.11) are used. Normalized extinction represents mixing ratio. This study shows for the first time vertical distribution of normalized extinctions at altitude above 90 km.

Figs.4.16 show vertical distribution of normalized extinction, calculated from extinctions (Figs.4.1) and CO_2 number densities of VIRA 1985 model [Keating et al., 1985].

Figs.4.17 show vertical distribution of normalized extinction, calculated from extinctions (Figs.4.2) and CO_2 number densities (Figs.4.12) by SOIR team.

Normalized extinctions at high latitude in the morning are shown in Fig.4.15 (a), Fig.4.16 (a) and Fig.4.17 (a). Similarly, those at high latitude in the evening, low latitude in the morning and low latitude in the evening are shown in Fig.4.15, Fig.4.16 and Fig.4.17 (b), (c) and (d), respectively. Some profiles are plotted on a figure every ten orders. The reason why profiles are classified every ten orders is that total number of data is large. Some profiles are classified into two groups (① and ②) depending on

observed time; ① shows that profiles are observed relatively early. The profiles at order 141 – 150 are indicated up to 120 km. All the diffraction orders with corresponding wavelengths are summarized in Appendix B. Each profile is color-coded according to orbit number. Orders and orbit numbers are written on the right hand of each figure. An error bar is plotted on each figure.

Normalized extinction profiles (Figs.4.15) share common features though different orders. Accordingly, these features have high reliability.

(1) Normalized extinctions vary order of magnitude every occultations.

(2) One of the notable features of these profiles is increase at altitude above 90 km at both high and low latitudes. From comparison with the increase of SO and SO_2 mixing ratios with altitude reported by Belyaev et al. (2012) (Fig.1.9), following process is speculated. At first, the sources of haze including sulfur will be transported upward from under altitude 90 km. Next, transported source will evaporate and SO・SO_2 will be produces at high altitude. In the next place, haze will be produced by any chemical process at high altitude. This is unexpected finding because it has not been recognized that haze exists at altitude above 90 km. This is cleared due to the first statistic analysis at altitude above 90 km with SOIR data in this study.

Figs.4.15, 4.16 and 4.17 have common features although computation methods of extinction and CO_2 number density differ from one another. Accordingly, these features have high reliability.

(1) Normalized extinctions vary order of magnitude every occultations.

(2) Normalized extinctions increase at altitude above 90 km.

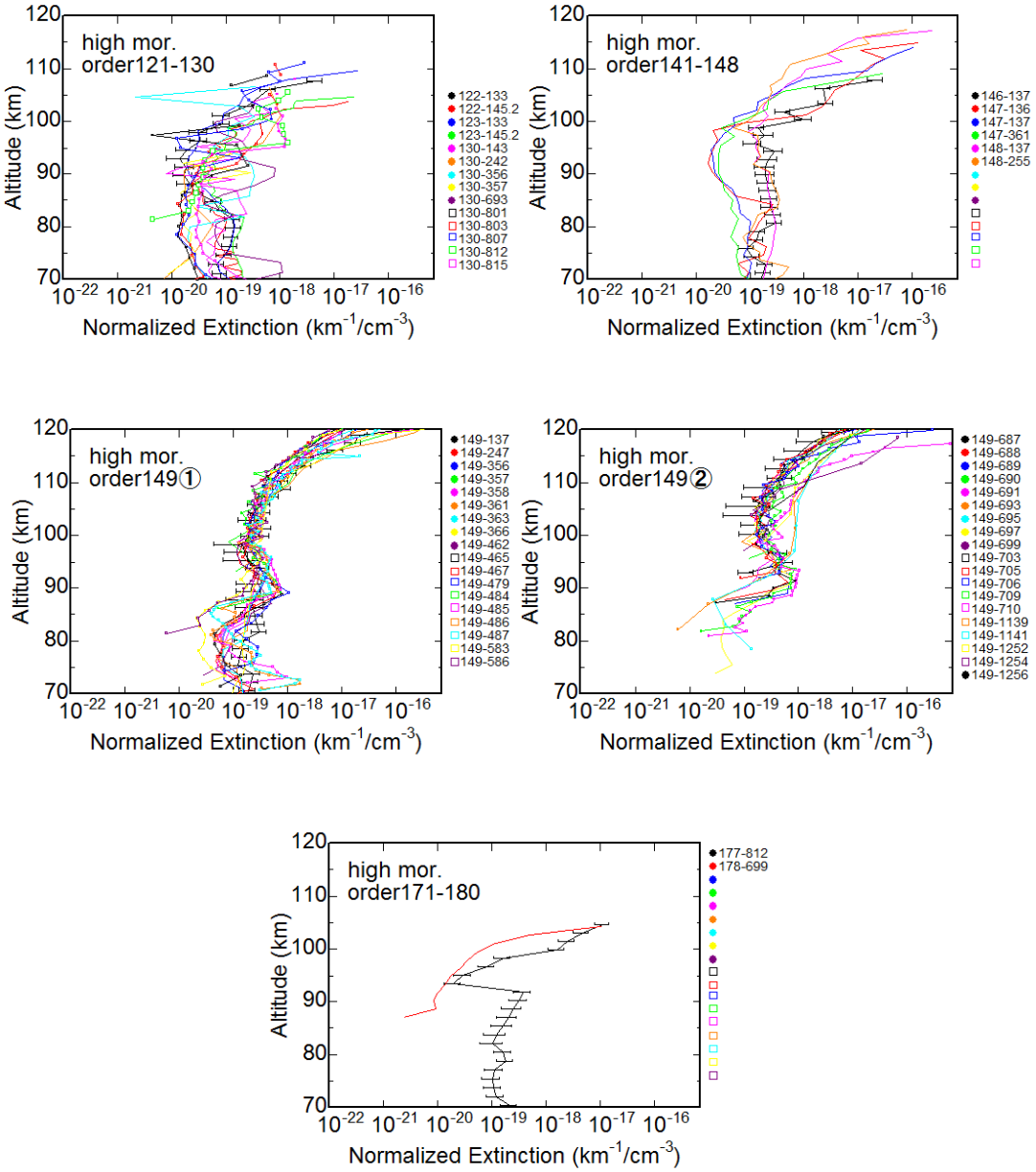

Fig.4.15 (a) Vertical distributions of normalized extinction of the present work at high latitude morning (Lat. > 60 °, LT < 12 h). All the diffraction orders with corresponding wavelengths are summarized in Appendix B. Each profile is color-coded according to orbit number. Orders and orbit numbers are written on the right hand of each figure. An error bar is plotted on each figure.

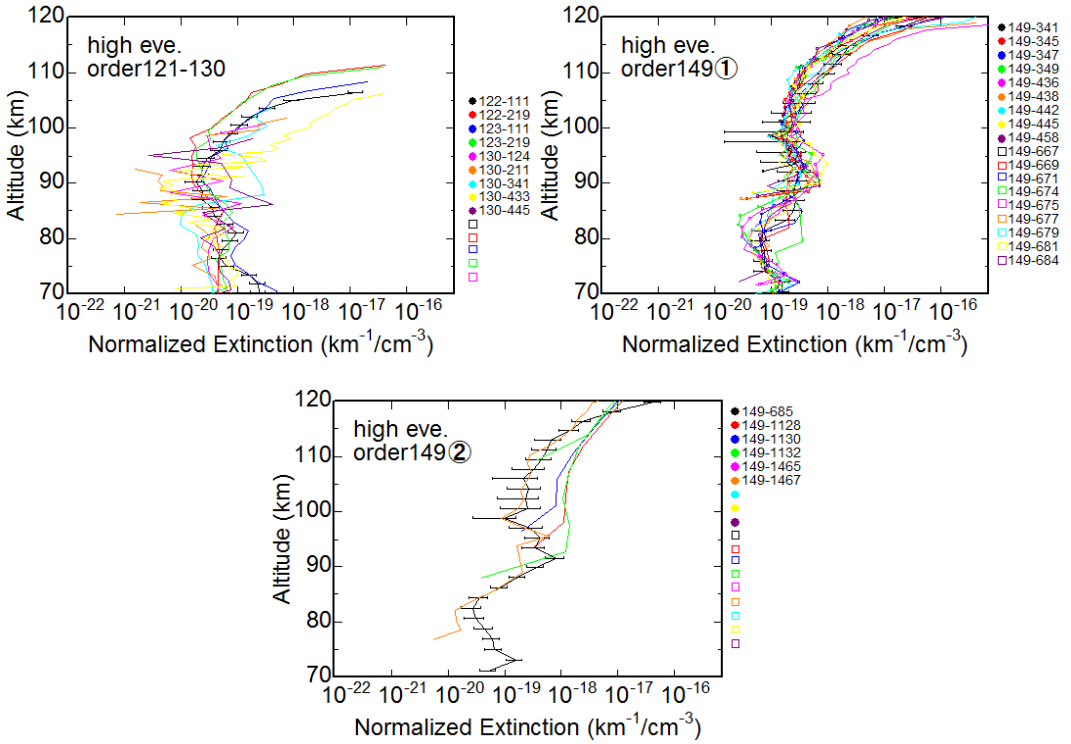

Fig.4.15 (b) Vertical distributions of normalized extinction of the present work at high latitude in the evening (Lat. > 60 °, LT > 12 h).

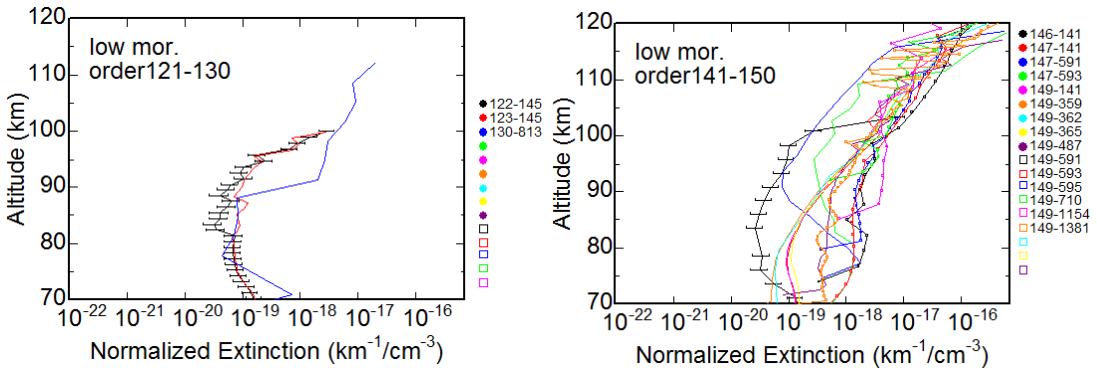

Fig.4.15 (c) Vertical distributions of normalized extinction of the present work at low latitude in the morning (Lat. < 60 °, LT < 12 h).

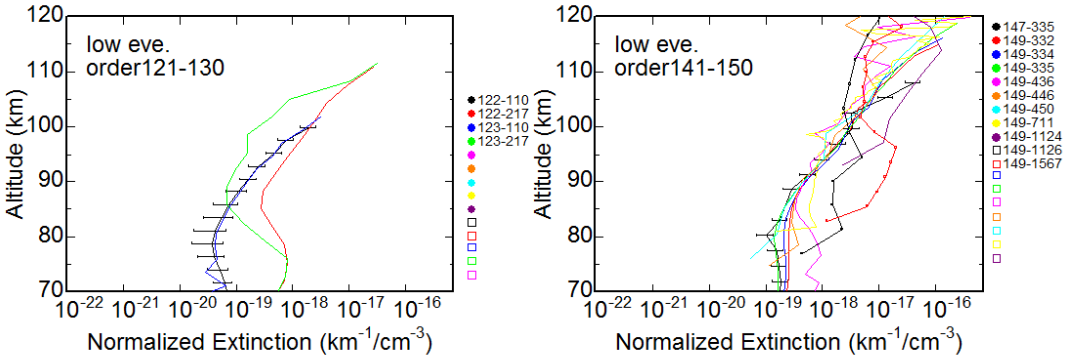

Fig.4.15 (d) Vertical distributions of normalized extinction of the present work at low latitude in the evening (Lat. < 60 °, LT > 12 h).

Vertical distributions of Normalized extinction (based on VIRA)

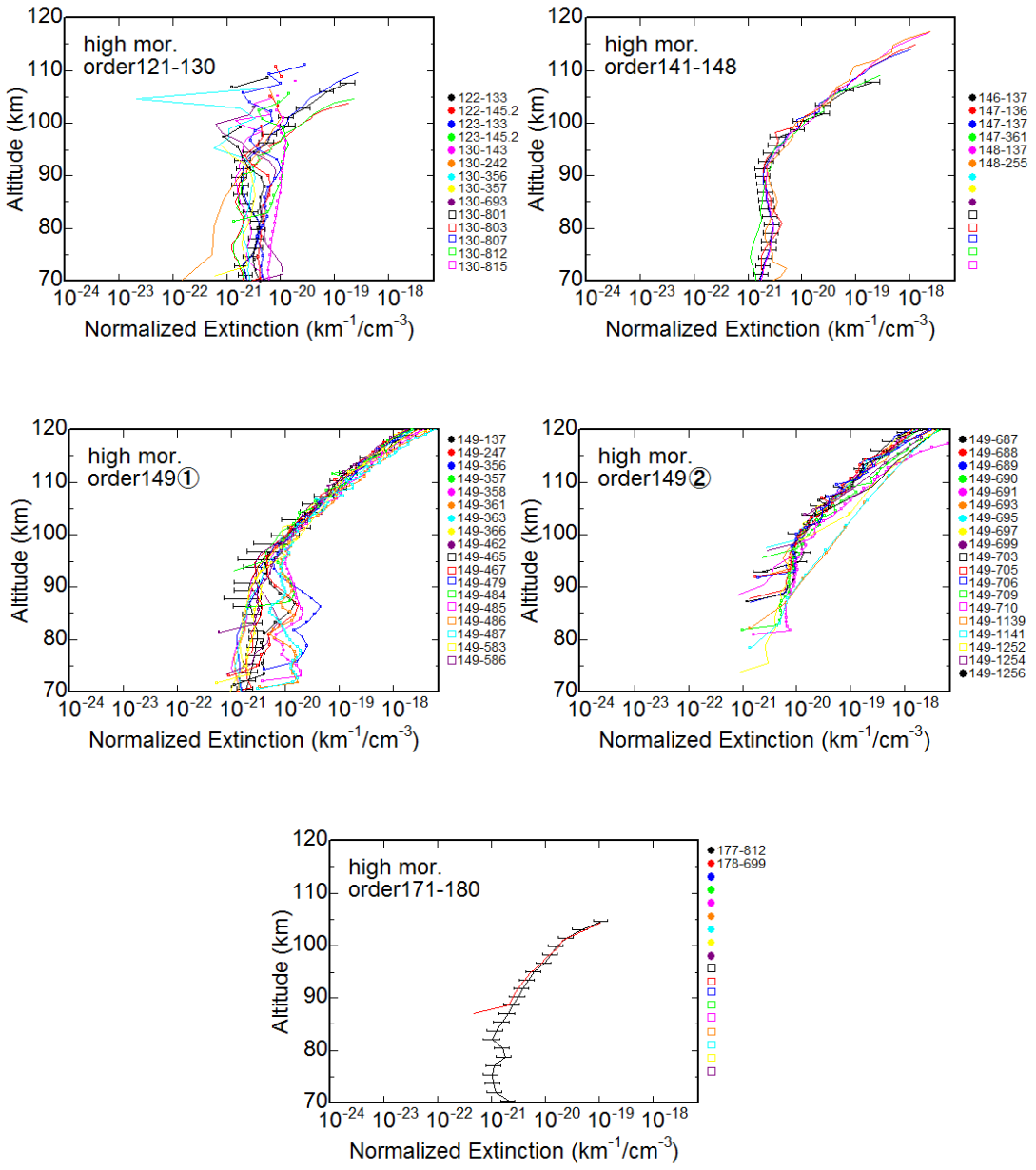

Fig.4.16 (a) Vertical distributions of observed normalized extinction in using extinctions (Fig.4.1 (a)) and VIRA CO_2 number densities at high latitude morning (Lat. > 60 °, LT < 12 h). All the diffraction orders with corresponding wavelengths are summarized in Appendix B. Each profile is color-coded according to orbit number. Orders and orbit numbers are written on the right hand of each figure. An error bar is plotted on each figure.

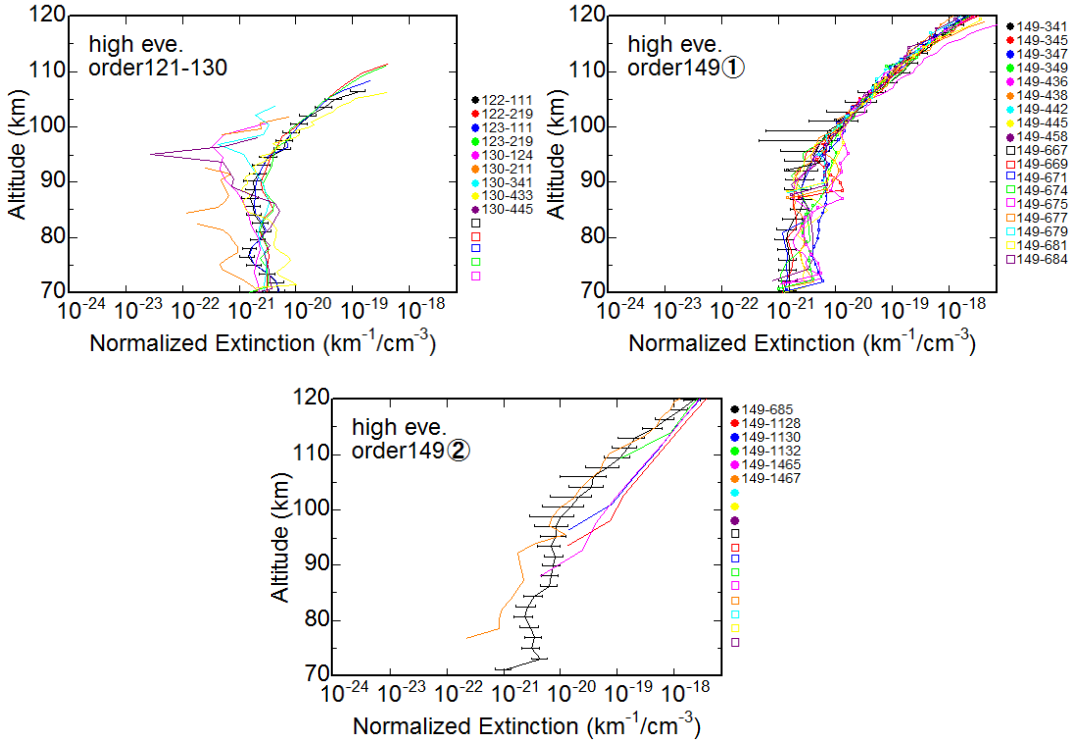

Fig.4.16 (b) Vertical distributions of observed normalized extinction in using extinctions (Fig.4.1 (b)) and VIRA CO_2 number densities at high latitude evening (Lat. > 60°, LT > 12 h).

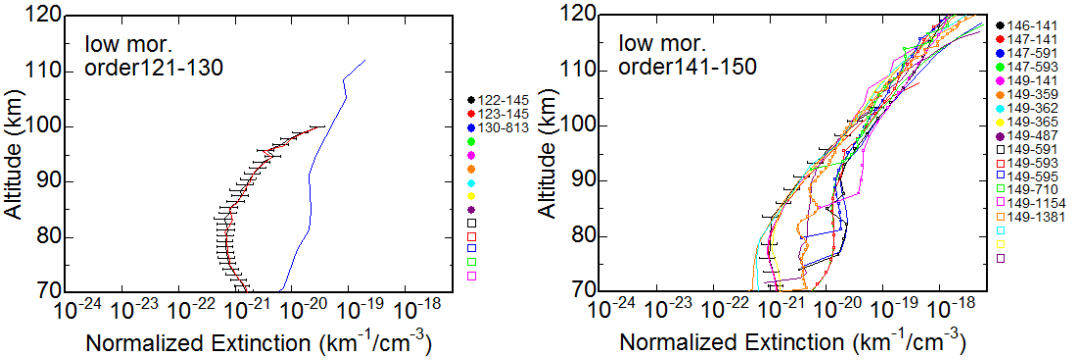

Fig.4.16 (c) Vertical distributions of observed normalized extinction in using extinctions (Fig.4.1 (c)) and VIRA CO_2 number densities at low latitude morning (Lat. < 60°, LT < 12 h).

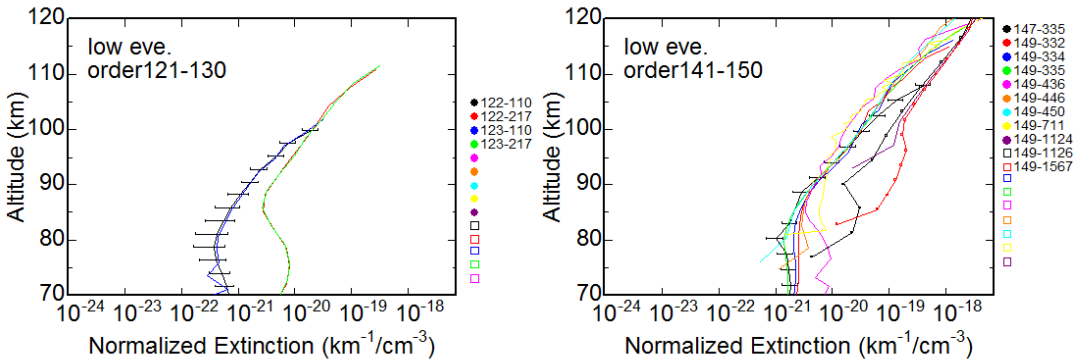

Fig.4.16 (d) Vertical distributions of observed normalized extinction in using extinctions (Fig.4.1 (d)) and VIRA CO_2 number densities at low latitude in the evening (Lat. < 60 °, LT > 12 h).

Vertical distributions of Normalized extinction (SOIR team)

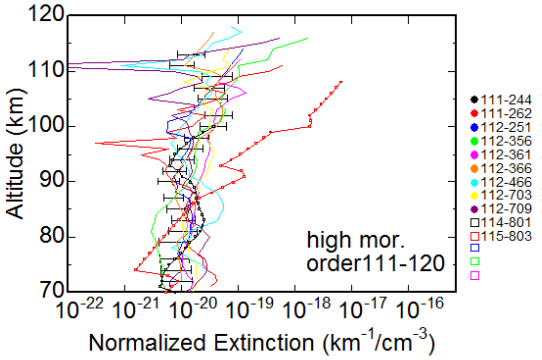
Altitude (km)
Normalized Extinction (km^{-1}/cm^{-3})
high mor.
order111-120
111-244
111-262
112-251
112-356
112-361
112-366
112-466
112-703
112-709
114-801
115-803

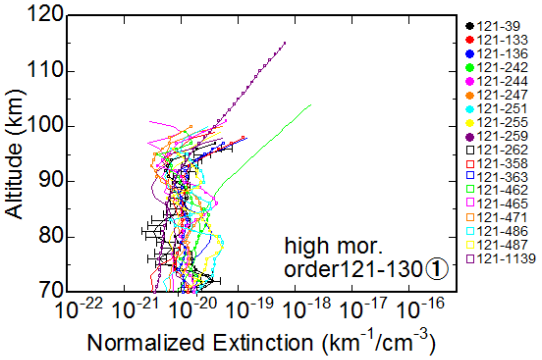
Altitude (km)
Normalized Extinction (km^{-1}/cm^{-3})
high mor.
order121-130①
121-39
121-133
121-136
121-242
121-244
121-247
121-251
121-255
121-259
121-262
121-358
121-363
121-462
121-465
121-471
121-486
121-487
121-1139

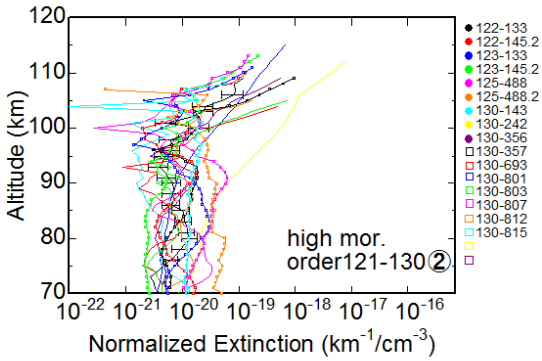
Altitude (km)
Normalized Extinction (km^{-1}/cm^{-3})
high mor.
order121-130②
122-133
122-145.2
123-133
123-145.2
125-488
125-488.2
130-143
130-242
130-356
130-357
130-693
130-801
130-803
130-807
130-812
130-815

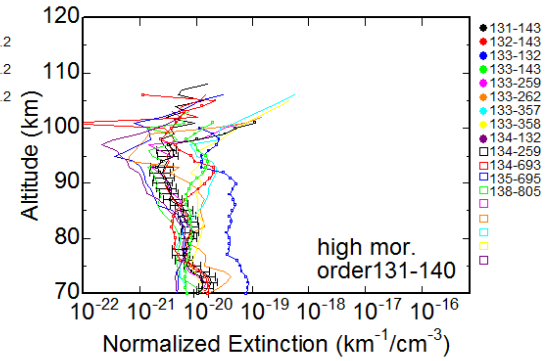
Altitude (km)
Normalized Extinction (km^{-1}/cm^{-3})
high mor.
order131-140
131-143
132-143
133-132
133-143
133-259
133-262
133-357
133-358
134-132
134-259
134-693
135-695
138-805

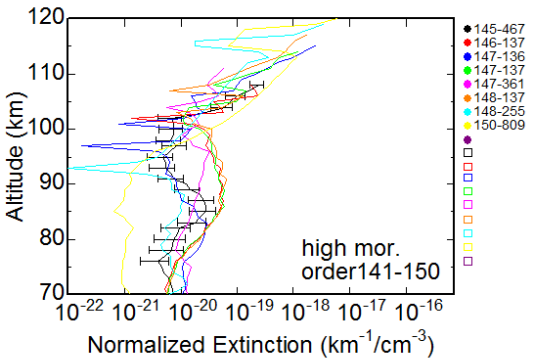
Altitude (km)
Normalized Extinction (km^{-1}/cm^{-3})
high mor.
order141-150
145-467
146-137
147-136
147-137
147-361
148-137
148-255
150-809

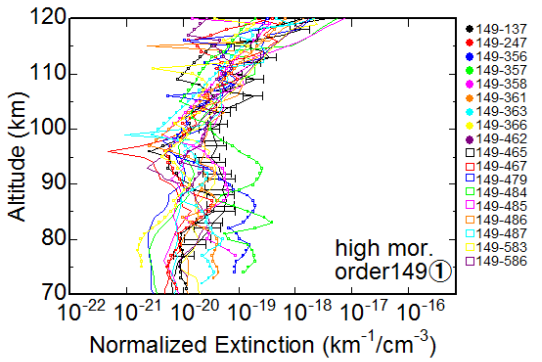
Altitude (km)
Normalized Extinction (km^{-1}/cm^{-3})
high mor.
order149①
149-137
149-247
149-356
149-357
149-358
149-361
149-363
149-366
149-462
149-465
149-467
149-479
149-484
149-485
149-486
149-487
149-583
149-586

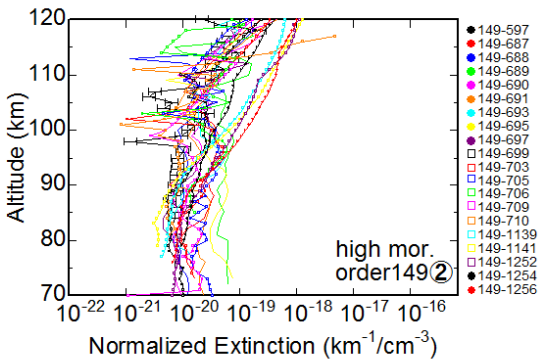
Altitude (km)
Normalized Extinction (km^{-1}/cm^{-3})
high mor.
order149②
149-597
149-687
149-688
149-689
149-690
149-691
149-693
149-695
149-697
149-699
149-703
149-705
149-706
149-709
149-710
149-1139
149-1141
149-1252
149-1254
149-1256

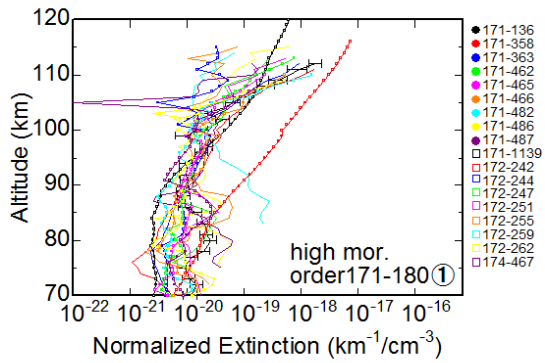
Altitude (km)
Normalized Extinction (km^{-1}/cm^{-3})
high mor.
order171-180①
171-136
171-358
171-363
171-462
171-465
171-466
171-482
171-486
171-487
171-1139
172-242
172-244
172-247
172-251
172-255
172-259
172-262
174-467

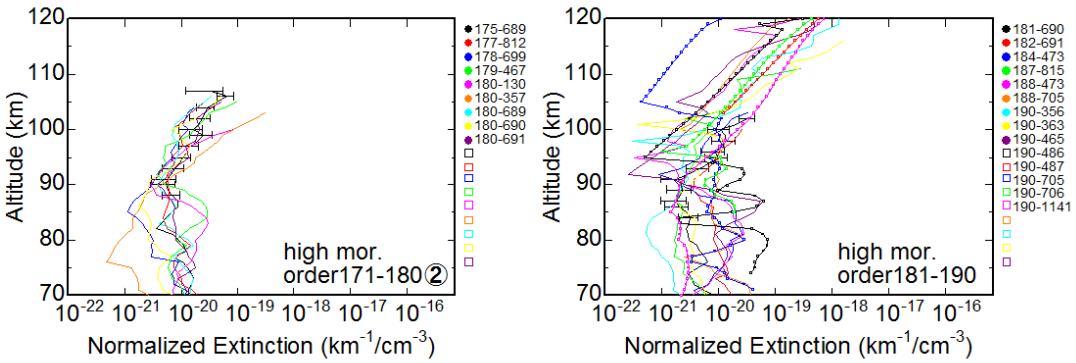

Fig.4.17 (a) Vertical distributions of normalized extinction of the SOIR team at high latitude morning (Lat. > 60°, LT < 12 h). All the diffraction orders with corresponding wavelengths are summarized in Appendix B. Each profile is color-coded according to orbit number. Orders and orbit numbers are written on the right hand of each figure. An error bar is plotted on each figure.

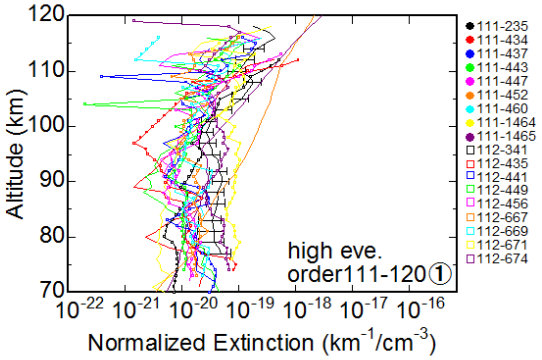
Altitude (km)
Normalized Extinction (km-1/cm-3)
high eve.
order111-120①
111-235
111-434
111-437
111-443
111-447
111-452
111-460
111-1464
111-1465
112-341
112-435
112-441
112-449
112-456
112-667
112-669
112-671
112-674

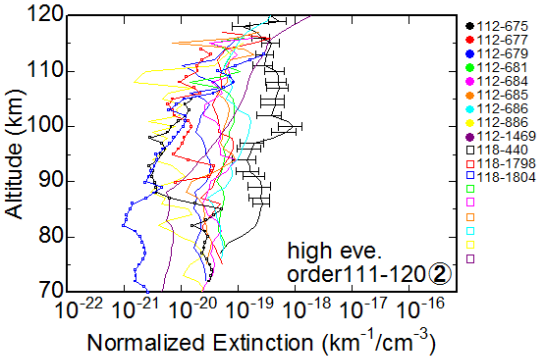
Altitude (km)
Normalized Extinction (km-1/cm-3)
high eve.
order111-120②
112-675
112-677
112-679
112-681
112-684
112-685
112-686
112-886
112-1469
118-440
118-1798
118-1804

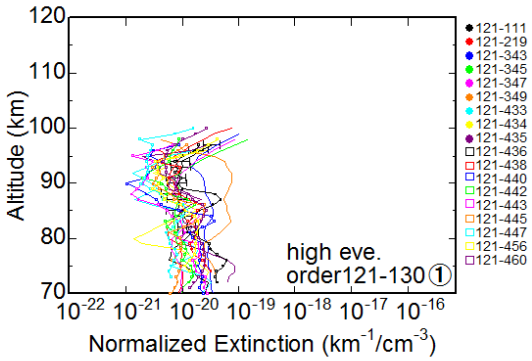
Altitude (km)
Normalized Extinction (km-1/cm-3)
high eve.
order121-130①
121-111
121-219
121-343
121-345
121-347
121-349
121-433
121-434
121-435
121-436
121-438
121-440
121-442
121-443
121-445
121-447
121-456
121-460

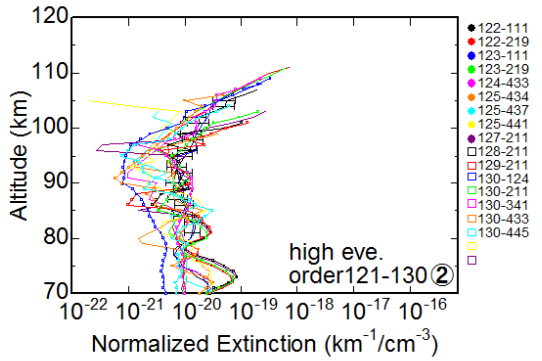
Altitude (km)
Normalized Extinction (km-1/cm-3)
high eve.
order121-130②
122-111
122-219
123-111
123-219
124-433
125-434
125-437
125-441
127-211
128-211
129-211
130-124
130-211
130-341
130-433
130-445

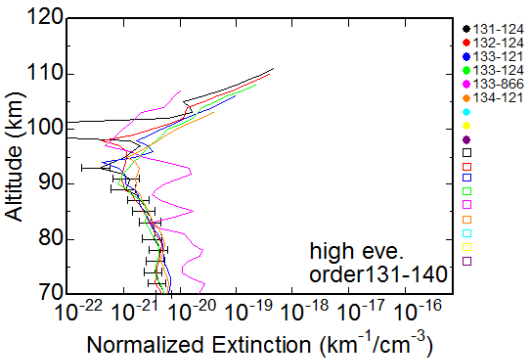
Altitude (km)
Normalized Extinction (km-1/cm-3)
high eve.
order131-140
131-124
132-124
133-121
133-124
133-866
134-121

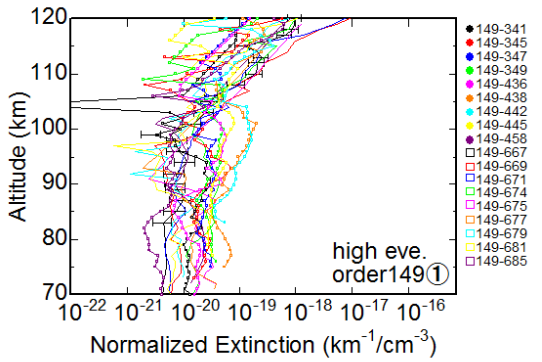
Altitude (km)
Normalized Extinction (km-1/cm-3)
high eve.
order149①
149-341
149-345
149-347
149-349
149-436
149-438
149-442
149-445
149-458
149-667
149-669
149-671
149-674
149-675
149-677
149-679
149-681
149-685

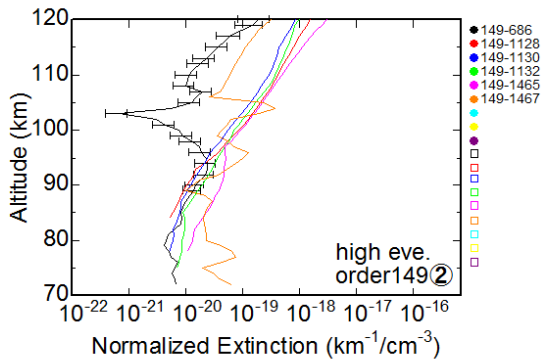
Altitude (km)
Normalized Extinction (km-1/cm-3)
high eve.
order149②
149-686
149-1128
149-1130
149-1132
149-1465
149-1467

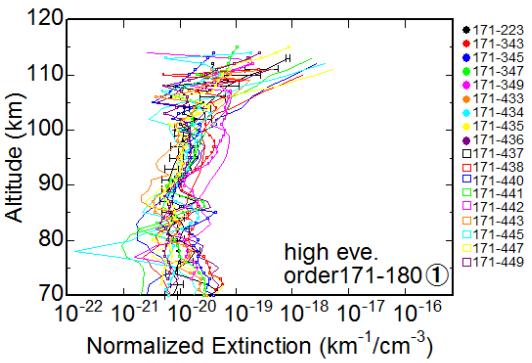
Altitude (km)
Normalized Extinction (km-1/cm-3)
high eve.
order171-180①
171-223
171-343
171-345
171-347
171-349
171-433
171-434
171-435
171-436
171-437
171-438
171-440
171-441
171-442
171-443
171-445
171-447
171-449

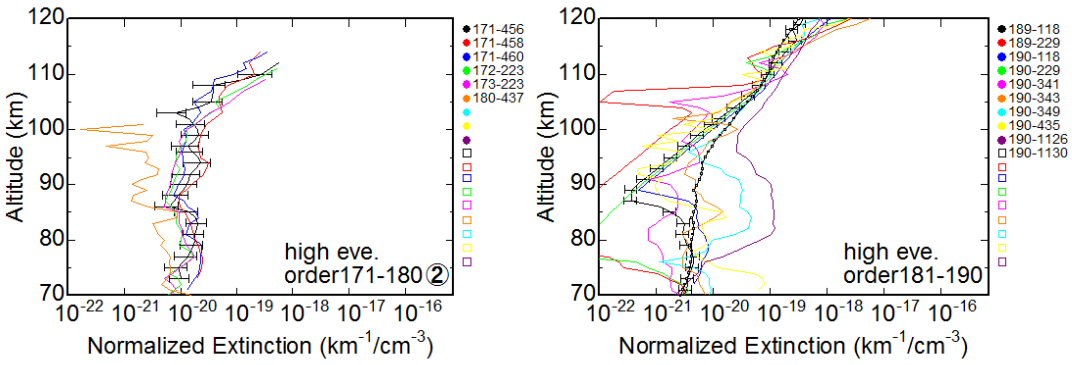

Fig.4.17 (b) Vertical distributions of normalized extinction of the SOIR team at high latitude evening (Lat. > 60 °, LT > 12 h).

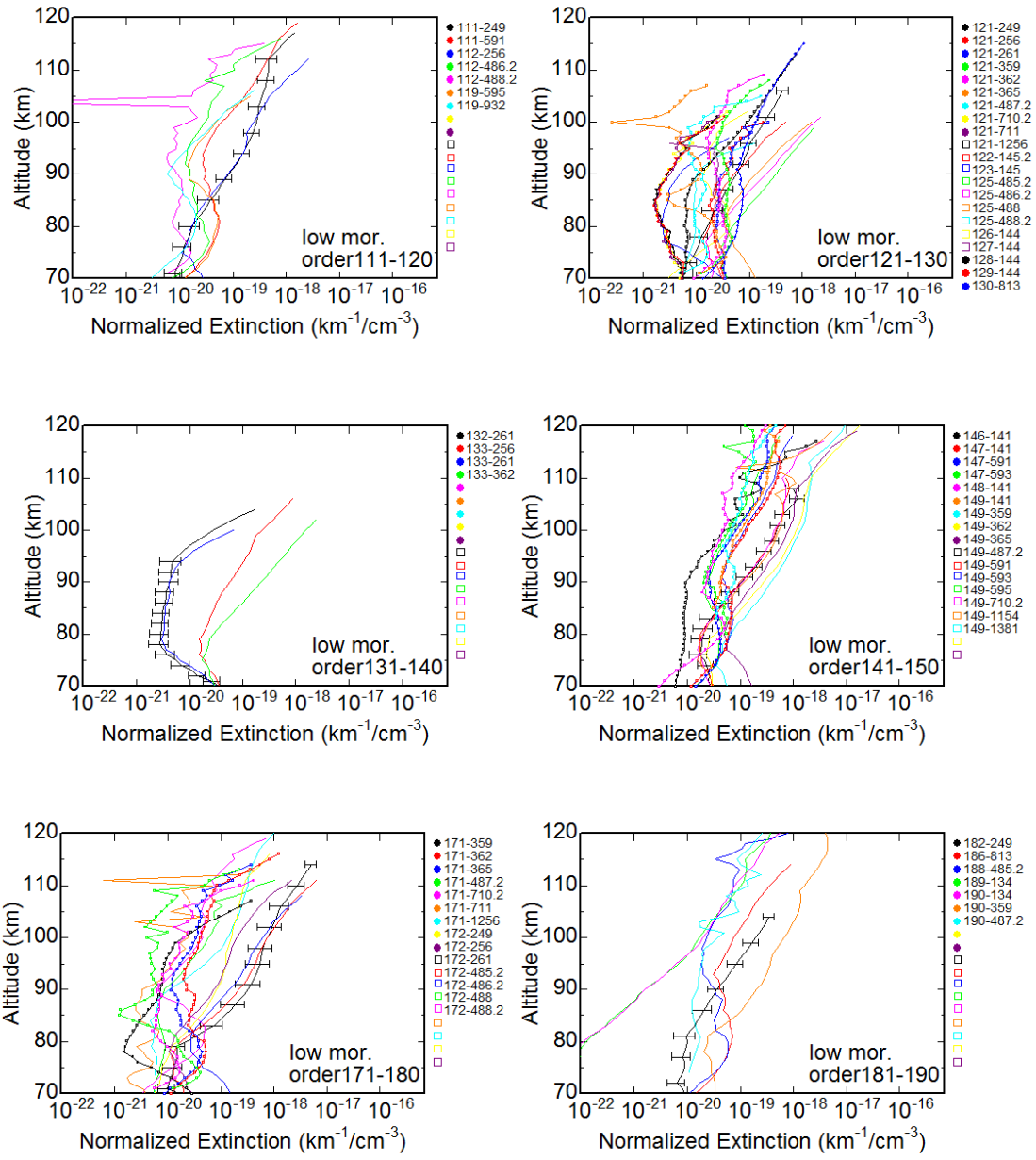

Fig.4.17 (c) Vertical distributions of normalized extinction of the SOIR team at low latitude morning (Lat. < 60 °, LT < 12 h).

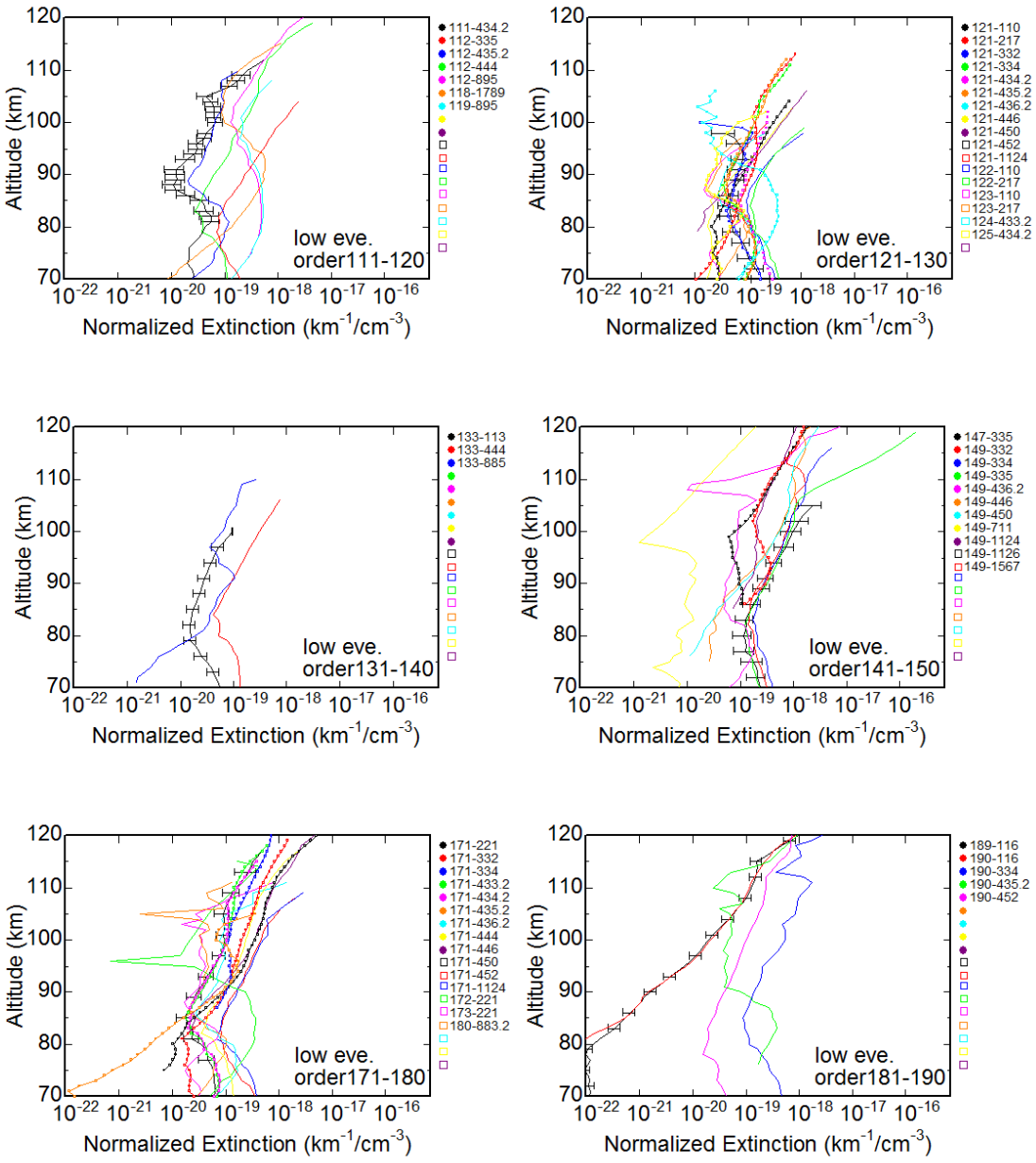

Fig.4.17 (d) Vertical distributions of observed normalized extinction of the SOIR team at low latitude evening (Lat. < 60 °, LT > 12 h).

4.4.2. Averages

The mean of all normalized extinctions of present work (Figs.4.15) is shown in Fig.4.18. Similarly, the mean of all normalized extinctions (Figs.4.16) is shown in Fig.4.19. The mean of all normalized extinctions of SOIR team (Figs.4.17) is shown in Fig.4.20. Error bar is plotted only at high latitude in the morning. This error is mean of each error.

Fig.4.18, 4.19 and 4.20 have common features although computation methods of extinction and CO_2 number density differ from one another.

(1) Significant increases of normalized extinctions are observed at altitude above 90 km at both high and low latitudes. From comparison with the increase of SO and SO_2 mixing ratios with altitude reported by Belyaev et al. (2012) (Fig.1.9), following process is speculated. At first, the sources of haze including sulfur will be transported upward from under altitude 90 km. Next, transported source will evaporate and SO・SO_2 will be produces at high altitude. In the next place, haze will be produced by any chemical process at high altitude. This is unexpected finding because it has not been recognized that haze exists at altitude above 90 km. This is cleared due to the first statistic analysis at altitude above 90 km with SOIR data in this study.

(2) Normalized extinctions at low latitude are almost order of magnitude larger than those at high latitude. It would appear that aerosols are more produced at low latitude than at high latitude.

Fig.4.18, 4.19 and 4.20 have different characteristics.

(1) Normalized extinctions differ by two orders of magnitude because of CO_2 number density difference.

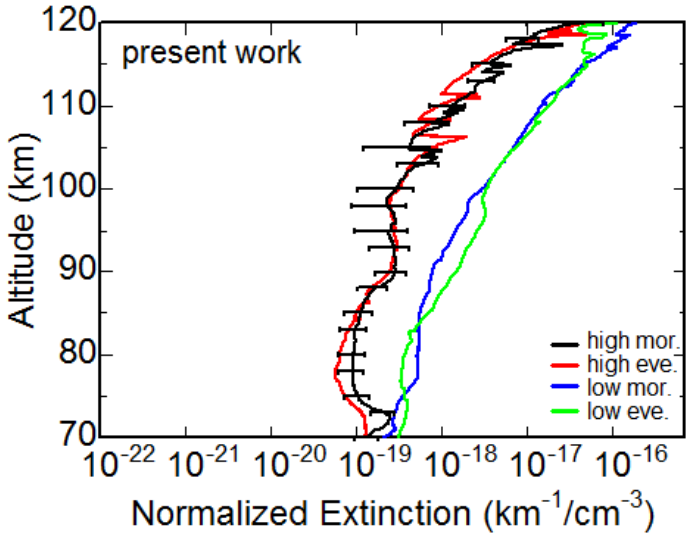

Fig.4.18 Mean of all normalized extinction of the present work (Figs.4.15); high latitude in morning (black line), high latitude evening (red line), low latitude in morning (blue line) and low latitude evening (green line). The error is shown only at high latitude in the morning.

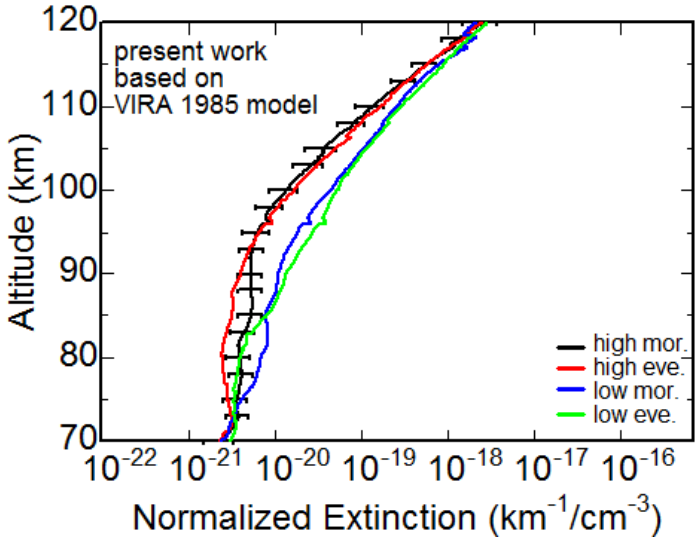

Fig.4.19 Mean of all normalized extinction of the present work based on VIRA 1985 model (Figs.4.16); high latitude in morning (black line), high latitude in evening (red line), low latitude in morning (blue line) and low latitude in evening (green line). The error is shown only at high latitude in the morning.

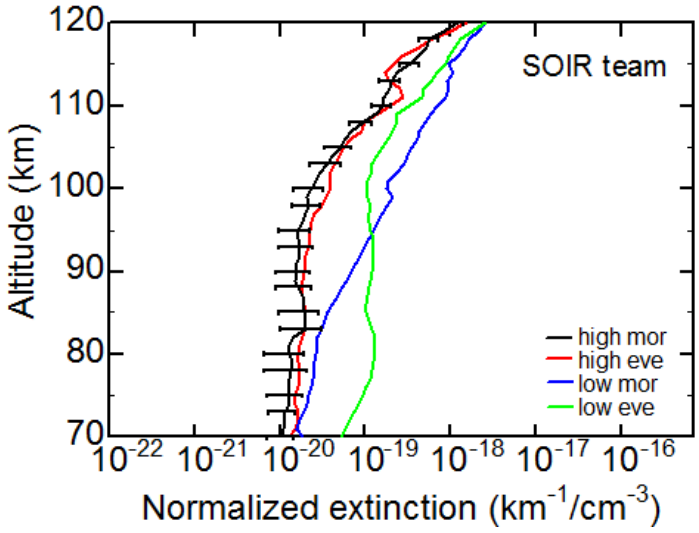

Fig.4.20 Mean of all normalized extinction (Figs.4.17); high latitude morning (black line), high latitude evening (red line), low latitude morning (blue line) and low latitude evening (green line). The error is shown only at high latitude in the morning.

5. Discussion

The properties of upper haze at altitude above 90 km were obtained for the first time as shown in Chapter 4. One of the notable results is that normalized extinctions exist and even increase at altitude above 90 km at both high and low latitudes. It is considered that sources of haze are transported to high altitude from main cloud height and haze are produced at high altitude.

Several studies have been made on sulfuric compound. According to a study by Belyaev et al. (2012), SO and SO_2 mixing ratios increase with altitude from 85 to 105 km (Fig.1.9). It is speculated that sources of SO and SO_2 are transported and could be photo-dissociation of H_2SO_4 vapor resulting from evaporation of acid aerosol droplets in the upper haze layer. Belyaev et al. (2008) also reported the variation of SO_2 abundance (Fig.1.10). After a sharp increase of SO_2 abundance between1967 and 1979, a gradual decline down to 20 ppb at 1995 was observed. At present, another global increase of SO_2 between 2004 and 2007 is observed.

Comparison with this study and previous study related to sulfuric compound, it is speculated about the correlation between sulfuric compound and haze. In this chapter, transport process and haze increase process related to sulfuric compound will be discussed.

5.1 Transport process

It follows from what has been said thus far that the sources of haze including sulfur are transported to high altitude from main cloud height.

The upward transport velocity can be estimated in comparison with sedimentation velocity. Imamura and Hashimoto. (2001) assume that the cloud particles are spherical and fall at the Stokes velocity. Sedimentation velocity w_{sed} is calculated

$$w_{sed} = -\frac{2}{9}\frac{g\rho r^2}{\eta} \qquad (5.1.1)$$

where g = 8.7 m s^{-2} is the acceleration of gravity, ρ = 1800 kg m^{-3} the particle mass density, r the particle radius, and η = 1.5×10^{-5} kg m^{-1} the viscosity of CO_2 gas. The sedimentation velocity is w_{sed} ∼ − 10^{-4} m s^{-1} for r = 1 μm, w_{sed} ∼ − 10^{-3} m s^{-1} for r = 3 μm, and w_{sed} ∼ − 10^{-2} m s^{-1} for r = 10 μm. However, eq.(5.1.1) does not hold under Venus tenuous atmosphere. In Venus atmosphere, sedimentation velocity u will be calculated as

$$u = \left(1 + \frac{1.26\lambda_a}{r}\right) w_{sed} \qquad (5.1.2)$$

where w_{sed} is given by eq.(5.1.1). λ_a is the mean free path and r is the particle radius. The mean free path may be obtained from the expression as follows:

$$\lambda_a = \lambda_{a,0}\left(\frac{p_0}{p}\right)\left(\frac{T}{T_0}\right) \qquad (5.1.3)$$

where p means pressure [mb], T means temperature and λ_a is mean free path. At standard condition, p_0, T_0 and $\lambda_{a,0}$ indicates 1013.25 [mb], 293.15 [K] and 6.6×10^{-6}

[cm], respectively. The sedimentation velocity under Venus tenuous atmosphere is estimated when $p = 10^{-3}$ [mb] and $T = 200$ [K] at 110 km [Mahieux et al., 2012]. The velocity is $u \sim 2.5$ m s^{-1} for $r = 0.25$ μm, $u \sim 5.0$ m s^{-1} for $r = 0.5$ μm, and $u \sim 10.0$ m s^{-1} for $r = 1$ μm.

The upward transport velocity is needed to have more than the speed of gravitational sedimentation.

Some following upward transport processes were proposed previously. The 60 – 100 km region (the mesosphere) is a transition region between the 4 day retrograde superrotation at the cloud top and the solar – antisolar circulation in the thermosphere (above 100 km), which has upwelling over the subsolar point and transport to the nightside. The downward velocity at 100 km near the anti-solar point is estimated to be ~43 cm s^{-1} from the observed nighttime temperature profiles in Bertaux et al. (2007). Another derivation in Liang and Yung. (2009) obtained a different value of ~1 cm s^{-1} at 100 km, which should be corrected to ~10 cm s^{-1}. Piccialli et al. (2008) proposed that the presence of the mid-latitude jet with peak velocity of 80 – 90 m s^{-1} centered at 50° S at the cloud tops (~70 km). Piccialli et al. (2012) estimated that a mid-latitude jet with a maximum speed up to 140 ± 15 m s^{-1} extending between 20° S and 55° S latitude at 70 km altitude.

.

5.2 Haze increase process

The following process is proposed to explain the increasing of normalized extinction at high altitude.

(1) Sources of haze are transported to high altitude from main cloud height. Some transport processes are described in previous section.

(2) Transported sources will evaporate and SO・SO_2 will be produced at high altitude. Increasing SO and SO_2 mixing ratios at high altitude was observed in Belyaev et al. (2012) (Fig.1.9). In case that the sources of haze are H_2SO_4, SO_2 will be produced by the following reactions [Mills and Allen, 2007, Zhang et al., 2012].

$$H_2SO_4 \rightarrow SO_3 + H_2O \qquad \textbf{(5.2.1 a)}$$

$$SO_3 + CO \rightarrow SO_2 + CO_2 \qquad \textbf{(5.2.1 b)}$$

Also, in case that the sources of haze are S_x, SO and SO_2 will be produced by reactions as below [Mills and Allen, 2007, Zhang et al., 2012].

$$S + O + M \rightarrow SO + M \qquad \textbf{(5.2.2 a)}$$

$$S_x + O \rightarrow SO + S_{x-1} \qquad \textbf{(5.2.2 b)}$$

$$SO + OH \rightarrow SO_2 + H \qquad \textbf{(5.2.3 a)}$$

$$SO + NO_2 \rightarrow SO_2 + NO \qquad \textbf{(5.2.3 b)}$$

$$SO + ClSO_2 \rightarrow SO_2 + ClS \qquad \textbf{(5.2.3 c)}$$

$$SO + O_3 \rightarrow SO_2 + O_2 \qquad \textbf{(5.2.3 d)}$$

$$SO + O \rightarrow SO_2 + O \qquad \textbf{(5.2.3 e)}$$

(3) Haze will be produced by any chemical process at high altitude. If H_2SO_4 will be reproduced, the following reaction is considered.

$$SO_3 + H_2O \rightarrow H_2SO_4 \qquad (5.2.4)$$

If S_x will be reproduced, the following reactions are considered [Mills and Allen, 2007, Zhang et al., 2012].

$$SO + h\nu \rightarrow S + O \qquad (5.2.5\ a)$$

$$SO_2 + h\nu \rightarrow S + O_2 \qquad (5.2.5\ b)$$

$$2S + M \rightarrow S_2 + M \qquad (5.2.5\ c)$$

$$S + S_2 + M \rightarrow S_3 + M \qquad (5.2.5\ d)$$

$$2S_2 + M \rightarrow S_4 + M \qquad (5.2.5\ e)$$

$$S_2 + S_4 + M \rightarrow S_6 + M \qquad (5.2.5\ f)$$

$$2S_4 + M \rightarrow S_8 + M \qquad (5.2.5\ g)$$

where *M* is any molecule.

As shown in Fig.1.9, SO and SO_2 mixing ratios increase with altitude from 85 to 105 km. To increase SO and SO_2 mixing ratios at high altitude, aerosol reaction rates are calculated with two 1-dimensional photochemistry–diffusion models [Zhang et al., 2012]. There are two ways for increasing SO and SO_2: Model A with enhanced H_2SO_4 abundance above 90 km and Model B with enhanced S_8 abundance above 90 km. The rates of the production of H_2SO_4 and S_x through the reactions described above for Model A and B are shown in Fig. 5.1. The H_2SO_4 production rate in model A has a secondary peak at 96 km where the SO_3 peak is located. But the S_x aerosol production rate above 90 km is small because the nucleation process is really slow when there are few aerosol particles to serve as condensation nuclei.

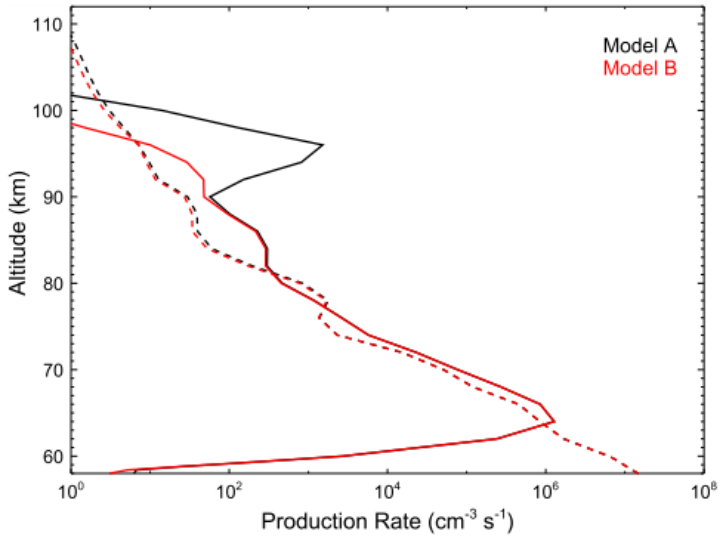

Fig.5.1 Production rate profiles of H_2SO_4 (solid) and S_x (dashed) for Model A (black) and B (red).

As shown in Fig.5.1, H_2SO_4 production rate at around 100 km is read 10^3 [cm^{-3} s^{-1}]. H_2SO_4 column production rate within a range of 5 km at around 100 km is obtained as follows:

$$10^3[cm^{-3}s^{-1}]\times 5\cdot 10^5[cm]=5\times 10^8[cm^{-2}s^{-1}] \qquad (5.2.6)$$

On the other hand, H_2SO_4 production rate at cloud altitude is estimated 10^{12} [cm^{-2} s^{-1}] in Imamura and Hashimoto. (2001). Assuming that 0.1 μm-size and 1.0 μm-size particles are produced in upper haze and cloud region, respectively, number density ratio is estimated as

$$\frac{n_{haze}}{n_{cloud}}=\frac{\dfrac{5\times 10^8}{(0.1)^3}}{\dfrac{10^{12}}{(1.0)^3}}=0.5 \qquad (5.2.7)$$

Assuming that scattering cross section is proportionate to geometric cross section, the ratios of scattering cross section is estimated as

$$\frac{\sigma_{haze}}{\sigma_{cloud}} = \frac{(0.1)^2}{(1.0)^2} = 0.01 \qquad (5.2.8)$$

The ratio of optical thickness is estimated as

$$\frac{\tau_{haze}}{\tau_{cloud}} \sim \frac{\sigma_{haze}}{\sigma_{cloud}} \times \frac{n_{haze}}{n_{cloud}} = 0.005 \qquad (5.2.9)$$

As shown in Fig.4.3, extinctions at 100 km are two or three orders magnitude smaller than those at 70 km. That is, the vertical distribution of extinction obtained in this study (Fig.4.3) is explainable in terms of H_2SO_4 production rate estimated in Zhang et al. (2012).

(4) The size of produced haze particles is considered to be smaller than that of transported sources for the following reason.

Extinction is obtained from the expression as follows:

$$k = \sigma \cdot N \qquad (5.2.10)$$

where σ is extinction cross section and N is number density of scattering material. Extinction cross section indicates a hypothetical are which describes the likelihood of light being absorbed and scattered by a particle. When haze particles become reduced in size without change in total amount of haze source material, cross section becomes smaller and number density becomes larger. For example, when particle becomes 0.5 times in size, extinction cross section becomes 1/4 times. On the other hand, number density becomes 8.0 times in volume. Under this circumstance, extinction will become larger than when the sources of haze are transported.

Normalized extinctions have possibility to increase at high altitude by above process. Given that normalized extinctions at low latitude are almost order of magnitude larger than those at high latitude, it would appear that haze are more produced at low latitude than at high latitude.

Given that the speculation noted above is correct, it is considered that transported relatively-large aerosols and reproduced small aerosols exist together at high altitude. This situation is similar to Fig.1.4 (taken from Wilquet et al. (2009)). Wilquet et al. (2009) demonstrated the existence of at least two types of particles at high altitude: mode 1 of mean radius $0.1 \leqq r \leqq 0.3$ μm and mode 2 of $0.4 \leqq r \leqq 1.0$ μm.

6. Conclusion

The properties of upper haze at altitude above 90 km were obtained for the first time in this study. The relationship between sulfuric compound and haze at high altitude was also discussed. These new knowledge concerning haze were cleared owing to analysis with wider altitude and latitude range in this study than previous study.

The upper haze properties were obtained at altitude above 90 km, especially extinction, optical thickness and normalized extinction.

(1) Upper haze exists at altitude above 90 km although it has been recognized that the top of upper haze is 90 km.

(2) Extinction profiles vary order of magnitude every occultations.

(3) Extinctions at low latitude are almost two times larger than those at high latitude. It would appear that aerosols are produced more at low latitude than at high latitude.

(4) Significant increases of normalized extinctions are observed at above 90 km at both high and low latitudes. From comparison with the vertical distributions of SO and SO_2 mixing ratios [Belyaev et al., 2012] (Fig.1.9), it would appear that haze is produced by any chemical reaction at high altitude after the sources of haze including sulfur are transported to altitude above 90 km. This is unexpected finding because it has not been recognized that haze exists at altitude above 90 km. This is cleared due to the first statistic analysis at altitude above 90 km with SOIR data in this study.

Haze transport and increase processes were discussed as below. For example, aerosols including sulfur will be transported upward at a velocity greater than sedimentation velocity. Transported aerosols will evaporate and SO・SO_2 will be produced at high altitude. In the next place, haze will be produced at high altitude by any chemical process. Since normalized extinctions increase with altitude at high altitude (Fig.4.18, 4.19 and 4.20), the size of produced haze particles is considered to be smaller than transported aerosols. Given that normalized extinctions at low latitude are almost order of magnitude larger than those at high latitude, it would appear that haze are more produced at low latitude than at high latitude.

CO_2 number densities vary almost two-digits at both high and low latitudes. It's not known exactly why CO_2 number densities vary enormously. CO_2 number densities obtained from this study are almost two orders magnitude smaller than those processed by the SOIR team. It would appear that this difference is caused by difference in absorption database and method to select data. However, we need to get into details about analysis algorithm of SOIR team to give a quantitative rating the difference. It is an issue in the future.

Acknowledgements

The author would like to thank Prof. N. Iwagami for his guidance during the doctoral course and stimulating discussions. The author wished to thank Dr. T. Imamura, Profs. M. Nakamura, T. Satoh, Y. Matsuda and Dr. I. Yoshikawa for providing important comments.

The author acknowledges generous support from SOIR team. The author thanks Dr. AnnCarine Vandaele for acceptance me into her laboratory and providing important comments. The author also thanks Drs. Arnaud Mahieux, Valerie Wilquet, Severine Robert and Rachel Drummond for stimulating discussions.

The author also wishes to thank members of space and planetary science at the University of Tokyo for support emotionally.

Appendix A.

The Venus Express payload

SPICAV/SOIR

It is made of three channels: SPICAV–IR, SPICAV–UV and SOIR. The two French channels, SPICAV-IR and SPICAV–UV are infrared and ultraviolet spectrometers [Bertaux et al., 2007]. SPICAV–UV is a highly sensitive instrument in the range of 110-310 nm with resolution of 1.5 nm based on an intensified CCD detector. SPICAV–IR covers the range from 0.7 to 1.7 μm with a resolving power of 1500. SPICAV operates both in nadir viewing and in stellar occultation modes. When working in stellar occultation mode, the UV channel sounds vertical distribution of sulfur-bearing gases (SO_2 and SO) above the clouds, and also CO_2, temperature and the aerosol content. SPICAV also operates in nadir mode. On the night side, these observations cover several spectral windows and allow the instrument to monitor the abundance of atmospheric water in the lower atmosphere, the total cloud opacity, and the surface temperature. The night-side NO 195 and O_2 airglow emissions are mapped by SPICAV to trace the thermospheric circulation [Bougher et al., 1997a]. On the day side, observations of the Lyman-alpha hydrogen and oxygen emissions allow studies of escape of these species.

VIRTIS

The VIRTIS instrument consists of two major parts: a mapping spectrometer (VIRTIS–M) that covers the range from 0.25 to 5 μm with moderate spectral resolution ($\lambda/\Delta\lambda \approx 200$), and a high spectral resolution spectrometer (VIRTIS–H) for the spectral

range from 2 to 5 μm ($\lambda/\Delta\lambda \approx 1200$) [Drossart et al., 2007]. VIRTIS monitors the abundance of trace gases (H_2O, CO, SO_2, COS) in the lower atmosphere, the total cloud opacity, and their variations. The variability of the lower atmosphere composition gives an indirect insight into the problems of deep atmospheric dynamics, surface-atmosphere interaction, and volcanic activity. On the day side, VIRTIS sounds gas and aerosol composition at the cloud tops. The second goal is the investigation of the atmospheric dynamics. VIRTIS measures the wind speeds by tracking cloud features in the UV and IR ranges that correspond to 70 and 50 km altitudes, respectively. They are complemented by observations of the O_2 airglow at 1.27 μm, which is considered a tracer of the lower thermosphere circulation (100 – 120 km) to yield a 3 – D time variable picture of Venus atmospheric dynamics. The third objective is to study the temperature and aerosol distribution in the mesosphere between 60 and 90 km by measuring thermal IR emission in the 4 – 5 μm range. The limb observations allows VIRTIS to investigate the vertical structure of haze layers above the cloud top with vertical resolution between few hundred meters and 2 km. In addition, VIRTIS maps the Venus surface in the 1 μm window on the night side. It is able to detect hot spots related to possible volcanic activity. Spatial resolution of these observations is limited by scattering in the clouds and is probably limited to about 50 km. Further night-side observations are used to search for lightning.

Appendix B.

Orders definition

This table summarizes all the diffractions order 101 to 190.

order	$\lambda_{min}(cm^{-1})$	$\lambda_{max}(cm^{-1})$	$\lambda_{mean}(cm^{-1})$	order	$\lambda_{min}(cm^{-1})$	$\lambda_{max}(cm^{-1})$	$\lambda_{mean}(cm^{-1})$
101	2257.16	2276.55	2266.86	**126**	2815.86	2840.05	2827.96
102	2279.51	2299.09	2289.30	**127**	2838.21	2862.59	2850.40
103	2301.86	2321.63	2311.75	**128**	2860.56	2885.13	2872.85
104	2324.21	2344.17	2334.19	**129**	2882.91	2907.67	2895.29
105	2346.55	2366.71	2356.63	**130**	2905.26	2930.21	2917.74
106	2368.90	2389.25	2379.08	**131**	2927.61	2952.75	2940.18
107	2391.25	2411.79	2401.52	**132**	2949.95	2975.29	2962.62
108	2413.60	2434.33	2423.97	**133**	2972.30	2997.83	2985.07
109	2435.95	2456.87	2446.41	**134**	2994.65	3020.37	3007.51
110	2458.29	2479.41	2468.85	**135**	3017.00	3042.91	3029.96
111	2480.64	2501.95	2491.30	**136**	3039.35	3065.45	3052.40
112	2502.99	2524.49	2513.74	**137**	3061.69	3087.99	3074.84
113	2525.34	2547.03	2536.19	**138**	3084.04	3110.54	3097.29
114	2547.69	2569.57	2558.63	**139**	3106.39	3133.08	3119.74
115	2570.04	2592.11	2581.08	**140**	3128.74	3155.62	3142.18
116	2592.38	2614.65	2603.52	**141**	3151.09	3178.16	3164.63
117	2614.73	2637.19	2625.96	**142**	3173.43	3200.70	3187.07
118	2637.08	2659.73	2648.41	**143**	3195.78	3223.24	3209.51
119	2659.43	2682.27	2670.85	**144**	3218.13	3245.78	3231.96
120	2681.78	2704.81	2693.30	**145**	3240.48	3268.32	3254.40
121	2704.12	2727.35	2715.74	**146**	3262.83	3290.86	3276.85
122	2726.47	2749.89	2738.18	**147**	3285.18	3313.40	3299.29
123	2748.82	2772.43	2760.63	**148**	3307.52	3335.94	3321.73
124	2771.17	2794.97	2783.07	**149**	3329.87	3358.48	3344.18
125	2793.52	2817.51	2805.52	**150**	3352.22	3381.02	3366.62

order	$\lambda_{min}(cm^{-1})$	$\lambda_{max}(cm^{-1})$	$\lambda_{mean}(cm^{-1})$	order	$\lambda_{min}(cm^{-1})$	$\lambda_{max}(cm^{-1})$	$\lambda_{mean}(cm^{-1})$
151	3374.57	3403.56	3389.07	**171**	3821.53	3854.36	3837.95
152	3396.92	3426.10	3411.51	**172**	3843.88	3876.90	3860.39
153	3419.26	3448.64	3433.95	**173**	3866.23	3899.44	3882.84
154	3441.61	3471.18	3456.40	**174**	3888.58	3921.98	3905.28
155	3463.96	3493.72	3478.84	**175**	3910.92	3944.52	3927.72
156	3486.31	3516.26	3501.29	**176**	3933.27	3967.06	3950.17
157	3508.66	3538.80	3523.73	**177**	3955.62	3989.60	3972.61
158	3531.00	3561.34	3546.17	**178**	3977.97	4012.14	3995.06
159	3553.35	3583.88	3568.62	**179**	4000.32	4034.68	4017.50
160	3575.70	3606.42	3591.06	**180**	4022.66	4057.22	4039.94
161	3598.05	3628.96	3613.51	**181**	4045.01	4079.76	4062.39
162	3620.40	3651.50	3635.95	**182**	4067.36	4102.30	4084.83
163	3642.75	3674.04	3658.40	**183**	4089.71	4124.84	4107.28
164	3665.09	3696.58	3680.84	**184**	4112.06	4147.38	4129.72
165	3687.44	3719.12	3703.28	**185**	4134.40	4169.92	4152.16
166	3709.79	3741.66	3725.73	**186**	4156.75	4192.46	4174.61
167	3732.14	3764.20	3748.17	**187**	4179.10	4215.00	4197.05
168	3754.49	3786.74	3770.62	**188**	4201.45	4237.54	4219.50
169	3776.83	3809.28	3793.06	**189**	4223.80	4260.08	4241.94
170	3799.18	3831.82	3815.50	**190**	4246.15	4282.62	4264.39

Appendix C.

Data set (morning)

The following table summarizes data used in this study.

Order	Orbit	Time	Lat.	Lon.	Order	Orbit	Time	Lat.	Lon.
122	133	1/9/2006	83	218	**149**	137	5/ 9/2006	79	237
122	145	13/9/2006	25	273	**149**	141	9/ 9/2006	-7	262
122	145.2	13/9/2006	59	270	**149**	247	24/12/2006	84	255
123	133	1/9/2006	83	218	**149**	356	12/ 4/2007	84	183
123	145	13/9/2006	25	273	**149**	357	13/ 4/2007	83	189
123	145.2	13/9/2006	59	270	**149**	358	14/ 4/2007	82	194
130	143	11/9/2006	68	262	**149**	359	15/ 4/2007	-45	216
130	242	19/12/2006	-71	207	**149**	361	17/ 4/2007	79	208
130	356	12/4/2007	84	183	**149**	362	18/ 4/2007	-29	224
130	357	13/4/2007	83	189	**149**	363	19/ 4/2007	76	216
130	693	14/3/2008	85	194	**149**	365	21/ 4/2007	-12	233
130	801	30/6/2008	87	86	**149**	366	22/ 4/2007	71	228
130	803	2/ 7/2008	86	108	**149**	462	27/ 7/2007	88	255
130	807	6/ 7/2008	84	135	**149**	465	30/ 7/2007	87	231
130	812	11/ 7/2008	79	158	**149**	467	1/ 8/2007	86	224
130	813	12/ 7/2008	-24	175	**149**	479	13/ 8/2007	77	235
130	815	14/ 7/2008	76	170	**149**	484	18/ 8/2007	70	246
145	467	1/ 8/2007	86	224	**149**	485	19/ 8/2007	68	249
146	137	5/ 9/2006	79	237	**149**	486	20/ 8/2007	65	251
146	141	9/ 9/2006	-7	262	**149**	487	21/ 8/2007	61	253
147	136	4/ 9/2006	80	233	**149**	487.2	21/ 8/2007	27	250
147	137	5/ 9/2006	79	237	**149**	583	25/11/2007	84	163
147	141	9/ 9/2006	-7	262	**149**	586	28/11/2007	82	177
147	361	17/4/2007	79	208	**149**	591	3/12/2007	-9	209
147	591	3/12/2007	-9	209	**149**	593	5/12/2007	3	215
147	593	5/12/2007	3	215	**149**	595	7/12/2007	17	220
148	137	5/ 9/2006	79	237	**149**	597.2	9/12/2007	59	223
148	255	1/ 1/2007	78	267	**149**	687	8/ 3/2008	88	223

Order	Orbit	Time	Lat.	Lon.	Order	Orbit	Time	Lat.	Lon.
149	688	9/3/2008	87	213	**149**	710.2	31/3/2008	21	217
149	689	10/3/2008	87	205	**149**	1139	3/ 6/2009	-75	91
149	690	11/3/2008	87	200	**149**	1141	5/ 6/2009	-67	100
149	691	12/3/2008	86	197	**149**	1154	18/6/2009	-7	144
149	693	14/3/2008	85	194	**149**	1252	24/9/2009	-73	95
149	695	16/3/2008	84	194	**149**	1254	26/9/2009	-65	98
149	697	18/3/2008	82	196	**149**	1256	28/9/2009	-57	103
149	699	20/3/2008	81	198	**149**	1381	31/1/2010	66	131
149	703	24/3/2008	77	206	**174**	467	1/ 8/2007	86	224
149	705	26/3/2008	74	210	**175**	689	10/3/2008	87	205
149	706	27/3/2008	73	212	**177**	812	11/7/2008	79	158
149	709	30/3/2008	67	219	**178**	699	20/3/2008	81	198
149	710.1	31/3/2008	63	221					

Data set (evening)

Order	Orbit	Time	Lat.	Lon.	Order	Orbit	Time	Lat.	Lon.
122	110	9/ 8/2006	-8	344	**149**	442	7/ 7/2007	78	285
122	111	10/ 8/2006	72	351	**149**	445	10/ 7/2007	81	292
122	217	24/11/2006	-13	317	**149**	458	11/ 7/2007	87	293
122	219	26/11/2006	79	317	**149**	667	15/ 7/2007	78	259
123	110	9/ 8/2006	-8	344	**149**	669	19/2/2008	79	263
123	111	10/ 8/2006	72	351	**149**	671	21/2/2008	81	268
123	217	24/11/2006	-13	317	**149**	674	24/2/2008	83	273
123	219	26/11/2006	79	317	**149**	675	25/2/2008	83	275
130	124	23/ 8/2006	88	88	**149**	677	27/2/2008	84	277
130	211	18/11/2006	70	296	**149**	679	29/2/2008	85	277
130	341	28/ 3/2007	82	348	**149**	681	2/ 3/2008	86	274
130	433	28/ 6/2007	66	262	**149**	684	5/ 3/2008	88	257
130	445	10/ 7/2007	81	292	**149**	685	6/ 3/2008	88	247
147	335	22/ 3/2007	-16	319	**149**	686	7/ 3/2008	88	235
149	332	19/ 3/2007	4	310	**149**	711.1	1/ 4/2008	58	223
149	334	21/ 3/2007	-10	316	**149**	1124	19/5/2009	-44	234
149	335	22/ 3/2007	-16	319	**149**	1126	21/5/2009	-52	240
149	341	28/ 3/2007	82	348	**149**	1128	23/5/2009	-60	247
149	345	1/ 4/2007	86	13	**149**	1130	25/5/2009	-69	255
149	347	3/ 4/2007	87	36	**149**	1132	27/5/2009	-77	264
149	349	5/ 4/2007	88	80	**149**	1465	25/4/2010	-60	200
149	436.1	1/ 7/2007	72	270	**149**	1467	27/4/2010	87	242
149	436.2	1/ 7/2007	17	272	**149**	1567	5/ 8/2010	-10	159
149	438	3/ 7/2007	75	275					

Reference

Belyaev, D., O. Korablev, A. Frdorova, J. –L. Bertaux, A. –C. Vandaele, F. Montmessin, A. Mahieux, V. Wilquet and R. Drummond, 2008: First observations of SO_2 above Venus' clouds by means of Solar Occultation in the InfraRed. *J. Geophys. Res* 113.

Belyaev, D., F. Montmessin, J. –L. Bertaux, A. Mahieux, A. Frdorova, O. Korablev, E. Marcq, Y. Yung, Z. Zhang, 2012: Vertical profiling of SO_2 and SO above Venus' clouds by SPICAV/SOIR solar occultations, *Icarus* 217, 740-751.

Bertaux, J. –L., D. Fonteyn, O. Korablev, E. Chassefière, E. Dimarellis, J.P. Dubois, A. Hauchecorne, M. Cabane, P. Rannou[a], A.C. Levasseur-Regourd, G. Cernogora, E. Quemerais, C. Hermans, G. Kockarts, C. Lippens, M.De Maziere, D. Moreau, C. Muller, B. Neefs, P.C. Simon, F. Forget, F. Hourdin, O. Talagrand,V.I. Moroz, A. Rodin, B. Sandel, A. Stern, 2000: The study of the Martian atmosphere from top to bottom with SPICAM Light on Mars Express, *Planet. Space Sci.*, 48, 1303– 1320.

Bertaux, J. –L., O. Korablev, S. Perrier, E. Quemerais, F. Montmessin, F. Leblanc, S. Lebonnois, P. Rannou, F. Lefevre, F. Forget, A. Fedorova, E. Dimarellis, A. Reberac, D. Fonteyn, J. Y. Chaufray and S. Guibert, 2006: SPICAM on Mars Express: Observing modes and overview of UV spectrometer data and scientific results. *J. Geophys. Res.* 111.

Bertaux, J. –L., A. –C. Vandaele, O. Korablev, E. Villard, A. Fedorova, D. Fussen, E. Quemerais, D. Belyaev, A. Mahieux, F. Montmessin, C. Muller, E. Neefs, D. Nevejans, V. Wilquet, J. P. Dubois, A. Hauchecorne, A. Stepanov, I. Vinogradov, A. Rodin and SPICAV/SOIR team, 2007: A warm layer in Venus' cryosphere and high-altitude measurements of HF, HCl, H_2O and HDO. *Nature* 450, 646-649.

Bougher, S. W., Alexander, M.J and Mayr, H.G., 1997a: Upper atmosphere dynamics: Global circulation and gravity waves. Vol. 1. Tucson: The University of Arizona Press. 259–291.

Braak, C. J., J. F. Haan and J. W. Hovenier, 2002: Spatial and temporal variations of Venus haze properties obtained from Pioneer Venus Orbiter polarimetry. *J. Geophys. Res* 107.

Clancy, R. T. and D. O. Muhleman, 1991: Long-term (1979 – 1990) changes in the thermal, dynamical and compositional structure of the Venus mesosphere as inferred from microwave spectral line observations of ^{12}CO, ^{13}CO, and $C^{18}O$. *Icarus* 89, 129 – 146.

de Kok, R., P. G. J. Irwin, C. C. C. Tsang, G. Piccioni and P. Drossart, 2011: Scattering particles in nightside limb observations of Venus' upper atmosphere by Venus Express VIRTIS. *Icarus* 211, 51-57.

Drossart, P., G. Piccioni, A. Adriani, F. Angrilli, G. Arnold, K.H. Baines, G. Bellucci, J. Benkhoff, B. B´ezard, J. –P. Bibring, A. Blanco, M.I. Blecka, and R.W. Carlson, 2007: Scientific goals for the observation of Venus by VIRTIS on ESA/Venus Express mission. *Planet. Space Sci.*, 55(12), 1653–1672.

Esposito, L. W., R. G. Knollenberg, M. Ya. Marov, O. B. Toon and R. P. Turco, 1983: The Clouds and hazes of Venus. *Venus*, 484-564. Univ. of Arizona Press.

Esposito, L. W., 1984: Sulfur Dioxide: Episodic Injection Shows Evidence for Active Venus Volcanism. *Science* 223, 1072-1074.

Esposito. L. W., M. Copley, R. Eckert, L. Gates, A. I. F. Stewart and H. Worden, 1988: Sulfur Dioxide at the Venus Cloud Tops, 1978-1986. *J. Geophys. Res* 93, 5267-7491.

Guzewich. S.D., Elsayed R. Talaat, Anthony D. Toigo, Darryn W. Waugh,and Timothy H. McConnochie, 2013: High-altitude dust layers on Mars: Observations with the Thermal Emission Spectrometer. *J. Geophys. Res.* 118, 1177 – 1194.

Hansen, J. E. and J. W. Hovenier, 1974: Interpretation of the Polarization of Venus. *J. Atmos. Sci.* 31, 1137-1160.

Hedin, A. E., H. B. Niemann and W. T. Kasprzak, 1983: Global empirical model of the Venus thermosphere. *J. Geophys. Res.* 88, 73 – 83.

Hestroffer, D. and C. Magnan, 1998: Wavelength dependency of the Solar limb darkening. *Astron. Astrophys.* 333, 338-342.

Imamura, T. and G.L. Hashimoto, 1998: Venus cloud formation in the meridional circulation. *J. Geophys. Res* 103, 31349-31366.

Imamura, T. and G.L. Hashimoto, 2001: Microphysics of Venusian Clouds in Rising Tropical Air. *J. Atmos. Sci.* 58, 3597-3612.

Kawabata, K., D. L. Coffeen, J. E. Hansen, W. A. Lane, M. Sato and L. D. Travis, 1980: Cloud and Haze Properties from Pioneer Venus Polarimetry. *J. Geophys. Res* 85, 8129-8140.

Keating, G. M., J. L. Bertaux, S. W. Bougher, T. E. Cravens, R. E. Dickinson, V. A. Krasnopolsky, A. F. Nagy, J. Y. Nicholson Ⅲ, L. J. Paxton and U von Zahn, 1985: Structure and composition, Venus International Reference Atmosphere Ⅳ. *Adv. Space. Res* 5, 117-172.

Knibbe, W. J. J., J. F. Haan and J. W. Hovenier, 1998: Analysis of temporal variations of the polarization of Venus observed by Pioneer Venus Orbiter. *J. Geophys. Res* 103, 8557-8574.

Krasnopolsky, V. A, 1986: *Photochemistry of the Atmosphere of Mars and Venus.* 147.

Krasnopolsky, V. A, and J.B. Pollack, 1994: H_2O-H_2SO_4 System in Venus' Clouds and OCS, CO, and H_2SO_4 Profiles in Venus' Troposphere. *Icarus* 109, 58-78.

Liang, M and Y. L. Yung, 2009: Modeling the distribution of H_2O and HDO in the upper atmosphere of Venus. *J. Geophys. Res* 114.

Mahieux, A., S. Berkenbosch, R. Clairquin, D. Fussen, N. Mateshvili, E. Neefs, D. Nevejans, B. Ristic, A.C. Vandaele, V. Wilquet, D. Belyaev, A. Fedorova, O. Korablev, E. Villard, F. Montmessin and J. –L. Bertaux, 2008: In-flight performance and calibration of SPICAV SOIR onboard Venus Express. *Applied Optics* 47, 2252-2265.

Mahieux, A., A.C. Vandaele, E. Neefs, S. Robert. V. Wilquet, R. Drummond, A. Fedorova and J. –L. Bertaux, 2010: Densities and temperatures in the Venus mesosphere and lower thermosphere retrieved from SOIR on board Venus Express: Retrieval technique. *J. Geophys. Res* 115.

Mahieux, A., A.C. Vandaele, S. Robert, V. Wilquet, R. Drummond, F. Montmessin and J. –L. Bertaux, 2012: Densities and temperatures in the Venus mesosphere and lower thermosphere retrieved from SOIR on board Venus Express: Carbon dioxide measurements at Venus terminator. *J. Geophys. Res* 117.

Mahieux, A, Inversion of the infrared spectra recorded by the SOIR instrument on board Venus Express. Doctoral Thesis.

Mills, F. P., and M. Allen, 2007: A review of selected issues concerning the chemistry in Venus' middle atmosphere. *Planet. Space Sci* 55, 1729-1740.

Na, C. Y., L. W. Esposito and T. E. Skinner, 1990: International Ultraviolet Explorer Observation of Venus SO_2 and SO. *J. Geophys. Res* 95, 7485-7491.

Nevejans, D., E. Neefs, E. V. Ransbeeck, S. Berkenbosch, R. Clairquin, L. D. Vos, W. Moelans, S. Glorieyx, A. Baeke, O. Korablev, I. Vinogradov, Y. Kalinnikov, B. Bach, J. P. Dubois and E. Villard, 2006: Compact high-resolution spaceborne echelle grating spectrometer with acousto-optical tunable filter based order sorting for the infrared domain from 2.2 to 4.3 μm. *Applied Optics* 45, 5191-5206.

Piccialli, A., D. V. Titov, D. Grassi, I. Khatuntsev, P. Drossart, G. Piccioni and A. Migliorini, 2008: Cyclostrophic wings from the Visible and Infrared Thermal Imaging Spectrometer temperature sounding: A preliminary analysis. *J. Geophys. Res* 113.

Piccialli, A., S. Tellmann, D. V. Titov, S. S. Limaya, I.V. Khatuntsev, M. Patzold and B. Hausler , 2012: Dynamical properties of the Venus mesosphere from the radio-occultation experiment VeRa onboard Venus Express. *Icarus* 217, 669-681.

Prinn, R.G., 1975: Venus: Chemical and Dynamical Processes in the Stratosphere and Mesosphere. *J. Atmos. Sci.* 32, 1237-1247.

Sandor, B. J., R. T. Clancy and G. M. Schieven, 2012: Upper limits for H_2SO_4 in the mesosphere of Venus. *Icarus* 217, 839-844.

Sato, M., L. D. Travis and K. Kawabata, 1996: Photopolarimetry Analysis of the Venus Atmosphere in Polar Regions. *Icarus* 124, 569-585.

Soret, L., J. –C. Gerard, F. Montmessin, G. Piccioni, P. Drossart, J –L. Bertaux, 2012: Atomic oxygen on the Venus nightside: Global distribution deduced from airglow mapping. *Icarus* 217, 849-855.

Stiepen, A., L. Soret, J. –C. Gerard, C. Cox and J. –L. Bertaux, 2012: The vertical distribution of the NO nightglow: Limb profiles inversion and one-dimensional modeling. *Icarus* 220, 981-989.

Svedhem, H., D. V. Titov, D. McCoy, J. –P. Lebreton, S. Barabash, J. –L. Bertaux, P. Drossart, V. Formisano, B. Hausler, O. Korablev, W. J. Markiewicz, D. Nevejans, M. Patzold, G. Piccioni, T. L. Zhang, F. W. Taylor, E. Lellouch, D. Koschny, O. Witasse, H. Eggel, M. Warhaut, A. Accomazzo, J. Rodriguez-Canabal, J. Fabrega, T. Schirmann, A. Clochet and M. Coradini, 2007: Venus Express- The first European mission to Venus. *Planet. Space Sci* 55, 1636-1652.

Takagi, S. and N. Iwagami, 2011: Contrast sources for the infrared images taken by the Venus mission AKATSUKI. *Earth. Planet. Space* 63, 435-442.

Titov, D.V., H. Svedhem, D. Koschny, R. Hoofs, S. Barabash, J. –L. Bertaux, P. Drossart, V. Formisano, B. Hausler, O. Korablev, W. J. Markiewicz, D. Nevejans, M. Patzold, G. Piccioni, T.L. Zhang, D. Merritt, O. Witasse, J. Zender, A. Acco,azzo, M. Sweeney, D. Trillard, M. Janvier and A. Clochet, 2006: Venus Express science planning. *Planet. Space Sci* 54, 1279-1297.

Yung, Y., M.C. Liang, X. Jiand. R.L. Shia, C. Lee, B. Bezard and E. Marcq, 2009: Evidence for carbonyl sulfide (OCS) conversion to CO in the lower atmosphere of Venus. *J. Geophys. Res* 114.

Vandaele, A.C., M. De Maziere, R. Drummond, A. Mahieux, E. Neefs, V. Wilquet, O. Korablev, A. Fedorova, D. Belyaev, F. Montmessin and J. –L. Bertaux, 2008: Comparison of the Venus mesosphere measured by Solar Occultation at Infrared on board Venus Express. *J. Geophys. Res* 113.

Wilquet. V., A. Fedorova, F. Montmessin, R. Drummond, A. Mahieux, A.C. Vandaele, E. Villard, O. Korablev and J. –L. Bertaux, 2009: Preliminary characterization of the upper haze by SPICAV/SOIR solar occultation in UV to mid-IR onboard Venus Express. *J. Geophys. Res* 114.

Wilquet. V., R. Drummond, A. Mahieux, S. Robert, A.C. Vandaele and J. –L. Bertaux, 2012: Optical extinction due to aerosols in the upper haze of Venus: Four years of SOIR/VEX observations from 2006 to 2010. *Icarus* 217, 875-881.

Zahn, U., D. Krasnopolsky, K. Mauersberger, A. O. Nier and D. M. Hunten, 1979: Venus Thermosphere: In situ Composition Measurements, the Temperature Profiles, and the Homopause Altitude. *Science* 203, 768-770.

Zasova, L. V., V. I. Moroz, V. M. Linkin, I. A. Khatountsev and B. S. Maiorov, 2006: Structure of the Venusian atmosphere from surface up to 100 km. *Cosmic Res. Engl. Transl.* 44, 364-383.

Zasova, L. V., N. Ignatiev, I. Khatuntsev and V. Linkin, 2007: Structure of the Venus atmosphere, *Planet. Space Sci.* 55, 1712-1728.

Zhang, Xi., M. Liang, F. Mills, D. Belyaev and Y. Yung, 2012: Sulfur chemistry in the middle atmosphere of Venus. *Icarus*. 217, 714-739.